Bioengineering Materials for Environment Protection in a Changing Climate

Lead Guest Editor: Donatella Termini
Guest Editors: Hazi M. Azamathulla and Jose R. B. Cantalice
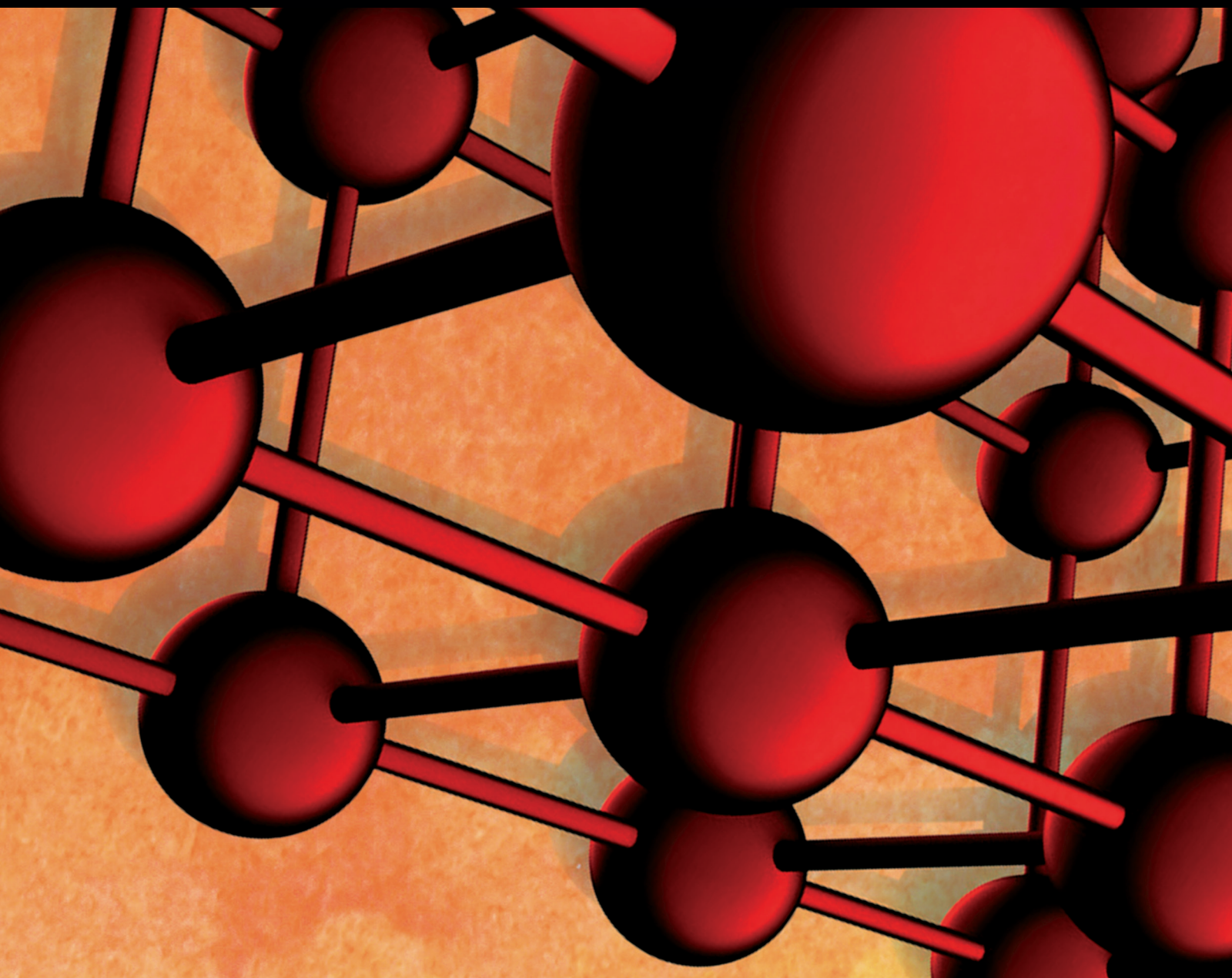
Bioengineering Materials for Environment Protection in a Changing Climate

Bioengineering Materials for Environment Protection in a Changing Climate

Lead Guest Editor: Donatella Termini
Guest Editors: Hazi M. Azamathulla and Jose R. B. Cantalice

Editorial Board

Contents

Editorial

Bioengineering Materials for Environment Protection in a Changing Climate

Donatella Termini [ID],[1] **Hazi M. Azamathulla,**[2] **and Jose R. B. Cantalice** [ID][3]

[1]*Department of Engineering, University of Palermo, Palermo, Italy*
[2]*Department of Civil and Environmental Engineering, University of the West Indies, West Indies, Mona, Jamaica*
[3]*Environmental Engineering Graduate Program, Rural Federal, University of Pernambuco, Recife, Brazil*

Correspondence should be addressed to Donatella Termini; donatella.termini@unipa.it

Climate change is one of the biggest problems of our times, and as time passes, climate extremes tend to increase both in magnitude and in frequency. Because the severity of the extreme climate events has increased, the interaction of these events with vulnerable human and natural systems has more frequently lead to disasters. Recent climate models' projections have also shown a further substantial warming in temperature extremes by the end of the 21st century. The prevision models' results also indicate that the global warming and the increase in frequency of temperature extremes could be strictly related to the anthropogenic forcing.

One of the environmental problems determined by warmer temperatures is the altering of the hydrological regime which determines changes in precipitation levels and patterns. The severity of disasters of hydrogeological origin produces serious damages to physical elements, buildings, and infrastructures located in vulnerable locations. Thus, climate-related disasters have both social and environmental dimensions.

The point is that although risks from climate extremes to industries, environment, and communities are increasing, still today they are not well quantified.

In this context, the knowledge of the potential environmental and socioeconomic impacts of climate change is fundamental to define procedures and technical solutions to protect the environment or to control the environmental hazards. In the ambit of the environmental engineering, which is the branch of engineering focusing on the aforementioned procedures and technical solutions, advanced bioengineering materials and combined techniques are needed to reduce the human impact on the environment. The present special issue collects contributions representing new ideas on innovative materials and advanced technologies in the area of environmental engineering.

A brief review of two techniques of controlling the human impact both in the extraurban and in urban areas, which adopt vegetation as living material, is reported in the paper by Termini. In particular, the first technique consists in using vegetation for soil erosion protection and rivers' bank stabilization in extraurban areas; the second technique consists in using vegetation for green roofs or walls added to buildings in urban areas. The discussion regarding the advantages and the disadvantages in adopting these two techniques concludes the review. The work demonstrates that the use of vegetation as biomaterial in environmental engineering could exert an important role in mitigating the worst effects due to anthropogenic actions. Furthermore, its use offers significant economic benefits, including a longer measure's life and an increasing biodiversity.

Another important issue for controlling soil degradation, deterioration, and improving the arid and semiarid soils is related to the use of polymers and biopolymers as soil-stabilizing additives. In the last two decades, the biodegradable polymers have been widely investigated to replace synthetic polymers. Dintcheva et al. analyze the effect of naturally occurring compounds, such as quercetin (Q) and sodium montmorillonite (NaMMt) at different weight ratios, in biopolyesters, such as polylactic acid, as suitable candidates for soil stabilization in the agricultural sector. The study is conducted through experimental and theoretical analyses by investigating the rheological behavior of these

materials and applying the fractional-order calculus to fit the experimental data. As a result, the authors conclude that the fractional model is able to predict the rheological behavior of the investigated complex biopolymer systems especially at long experimental time, thus confirming that it is possible to consider them as suitable materials for soil stabilization.

Oueslati and Meftah focus on the use of substances, like the montmorillonite, as a green solution in the context of geological barrier for industrial and/or radioactive hazardous waste confinement. In particular, the work of Oueslati and Meftah investigates the water-montmorillonite interaction under variable atmospheric conditions, in order to characterize the interlamellar space configuration for its possible use. Atmospheric stress and hydrological disturbance are obtained at the laboratory scale. The study also indicates the limits observed during sorption/desorption processes in the case of the stressed sample.

Another problem related to the environment responses due to climate and anthropogenic impacts is related to the absorption properties of inorganic or organic suspended particulate materials in a water body. In fact, a variability in absorption coefficients has been documented in oceanic waters where phytoplankton and their derivative products (such as organic detritus, natural decay of the algal cells) are optically dominant. Wang et al. explore the spectral variation of suspended particulate material absorption and its changing mechanism during flood periods of Poyang Lake and the relative influence in the remote sensing monitoring. The authors separate absorption coefficients of suspended particulate materials in Poyang Lake through controlled laboratory experiments during a flood period and analyze the changing mechanism for corresponding components of absorption in order to facilitate improvements in the parameterization of remote sensing algorithms for the interpretation of remote sensing information. Results show that the nonlinear dependency of specific phytoplankton particulate absorption on pigment concentration for various trophic statuses in different periods could bring uncertainties to the application of remote sensing algorithms.

In industrialized countries, one of the main environmental problems is due to the soil contamination by heavy metals. In fact, heavy metals are nonbiodegradable and strongly toxic affecting the ecosystem and the proprieties of soil. In the paper by Tang et al., the authors propose a method reinforcing the contaminated soils with fiber and cement, and through laboratory tests, they evaluate the strength of heavy metal contaminated reinforced soil. The test results show that the mechanical properties of reinforced soil change with increasing the fiber content until an optimum content at which the maximum reinforced soil corresponds. Thus, the authors verify that the addition of fibers can effectively prevent the damage caused by freeze-thaw cycles to the soils.

Conflicts of Interest

The guest editors declare that there are no conflicts of interest regarding the publication of this special issue.

Acknowledgments

Review Article

Use of Vegetation as Biomaterial for Controlling Measures of Human Impact on the Environment

Donatella Termini (iD)

Dipartimento di Ingegneria, University of Palermo, Palermo, Italy

Correspondence should be addressed to Donatella Termini; donatella.termini@unipa.it

Academic Editor: Lingxue Kong

In a context of a climate change, bioengineering techniques and biomaterials are needed to reduce the human impact on the environment. Thus, in recent years, living materials have been used in environmental engineering applications. In the present paper, attention is restricted to the vegetation, and a brief review on its use as biomaterial in engineering control techniques is presented. The core of this review is a comprehensive overview of two important techniques using vegetation as living material for measures limiting the human impact both in extra-urban and in urban sites. In particular, the use of vegetation both as living material for soil erosion protection and river's bank stabilization in extra-urban areas and as a part of green roofs or walls added to buildings in urban areas is presented. Considerations about the advantages and disadvantages of these techniques conclude this review.

1. Introduction

Environmental engineering is the branch of engineering identifying technical solutions to protect the environment and/or to control environmental hazards.

It is generally accepted that climate change is one of the biggest problems of our times. Climate change determines warmer temperatures altering the hydrologic cycle and changing the amount, timing, and intensity of precipitations [1]. This leads to a more frequent high-intensity rainfall events and consequent inundation phenomena both in urban and extra-urban areas. Recent literature (see as an example [2, 3]) exalts the role of the anthropogenic actions, such as the gases emissions, the fossil fuel use, and the fertilization, in the global mean temperature changes.

The use of biomaterials in bioengineering techniques, also in combination with traditional hydraulic or geo-technical engineering practices, would allow us to have an "environmentally friendly" measure to control the risks related to the extreme events and to mitigate considerably their effects. Furthermore, the application of such a kind of measure would allow us to reduce the worst effects of the anthropogenic actions with low overall costs.

In recent years, much more attention has been devoted to vegetation as living material in the ambit of bio-engineering measures. Such "environmentally friendly" material was used especially in the United States since the first decades of the 20th century; recently, and the interest on its use in environmental engineering has strongly increased also in Europe [4].

As literature (see as an example [5]) shows, climate is one of the controlling factors of the evolution and distribution of the vegetation species. Thus, a limitation in the use of vegetation is related to the fact that its characteristics are closely correlated to the climate so that rapid climate changes could lead to remarkable changes in the vegetation behavior, contributing to modify its protecting function.

In the present work, measures in environmental engineering using vegetation as living material are considered, and the emphasis is on two techniques adopted for limiting the human impact in extra-urban and in urban sites. Considerations about the advantages and disadvantages of these techniques conclude this review.

2. Vegetation as Biomaterial in Environmental Engineering

2.1. Vegetation and Measures for Protection and Erosion Control. In extra-urban areas, vegetation is generally used as living material for protection and stabilization actions in bioengineering techniques. In particular, vegetation and derived materials are used in controlling measures of soil erosion and of river's bank stability [6]. Soil erosion processes can severely damage the infrastructures and the environment. In fact, heavy rainfall can determine strong soil erosion either producing hyperconcentrated flows or determining localized erosion around structures or producing river's bank failure and inundation phenomena.

Thus, especially in recent years, researchers have devoted much attention to the identification of mutual interactions between riparian vegetation and rivers' morphodynamics (among others [7–12]). Riparian zones are transitional areas between water and land, and the vegetation in riparian zones (see Figure 1) is a key element exerting both an active role and a passive role on channel's morphodynamics.

In fact, on one hand, vegetation traps, reinforces, and aggrades landforms and the exposure of the trees to the hydrological processes; on the other hand, vegetation provides additional stability of deposited sediments due to the root systems [11]. According to Güneralp and Rhoads [8], as Figure 1 shows, different types of plants, which range from macrophytes to riparian trees, could control river morphology and the interaction between vegetation and fluvial morphology.

From a hydraulic point of view, vegetation is a source of flow resistance because it increases the bed roughness, decreasing bed shear stress and reducing the flow conveyance capacity [13–16]. As consequence, vegetation protects the bank and the bed creating feedbacks to sediment deposition [17] and reducing the soil erosion due to the reduction of the bed shear stress [18]. It should be noted that the quantification of the dissipative effects due to the presence of the vegetated elements depends on plants' shape, size, arrangement, and concentration [16].

On the construction point of view, the protective techniques in riparian zones could consist either of distributed single roots of plants (which are called as point-by-point systems) or of rows of roots of plants (which are called as linear systems) or of covering-mattress of plants (which are called as covering systems). Covering-mattresses of plants are also realized as measures against soil erosion processes. These measures consist either of flexible mattress or of wool geotextiles [19] with inseminated vegetation [20]. The plants grown on the wool geotextiles (Figure 2(a)) determine a mattress covered with the mixture of grasses and various herbaceous plants. Recently, simple mattress of inseminated herbaceous plants with deep roots has been realized [21].

To protect the vegetated river's bank, the so-called "crib walls" (see Figure 2(b)) are often used. They are realized with reticular systems of compartments realized either of wood or of prefabricated concrete and filled with vegetation (Figure 2(b)). In this case, vegetation especially allows
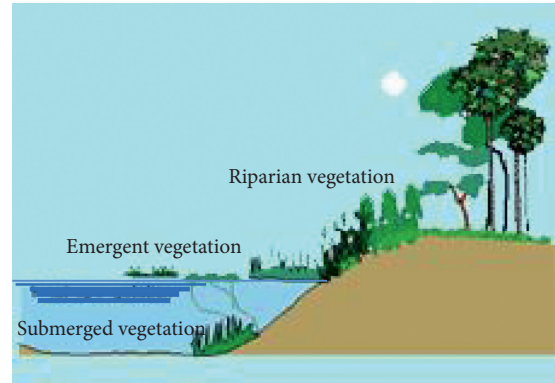
FIGURE 1: Example of riparian zone and vegetation.

reinforcing of the bank through its root system. In order to guarantee the good performance of such a measure, an efficient and periodical maintenance has to be performed because of the potential transport of sediment by the flow which could determine the emptying of the compartments especially before that the vegetation is fully developed.

It should be noted that the vegetation patterns are strongly controlled by flood disturbance which determines either its mechanical damage or the transport of seeds or the deposition of sediments. Thus, flood disturbance strongly influences the type of vegetation that establishes (among others [12, 22]). As consequence, vegetation composition and growth can vary greatly depending on the tolerances of the vegetation species. Furthermore, the vegetation distribution could also change in time and in space depending on the combination of factors affecting the settling and growth of the vegetated elements.

2.1.1. Functions and Advantages. In the aforementioned techniques, vegetation exerts a fundamental role performing both a hydrological-hydraulic function and an environmental function and a mechanical function, as schematized in Table 1. From Table 1, it can be summarized that on a hydrological-hydraulic point of view, vegetation allows to intercept raindrops, thus protecting the soil from erosion caused by rain splash. Furthermore, the roots of vegetation absorb the water surface limiting the soil saturation and the slope failure and reducing the flow velocity by increasing surface roughness; on an environmental point of view, vegetation allows the absorption of CO_2 depending on the soil characteristics and the temperature; on the mechanical point of view, the vegetation and its roots improve the stabilization of the bed material, thus increasing the soil strength and protecting the surface from water infiltration.

2.2. Vegetation and Measures to Limit the Worst Human-Induced Effects. Adding a green roof or a green wall (see Figure 3) to a building represents, especially in recent years, an "environmentally friendly" measure to limit the anthropogenic actions in urban areas. The green wall can be defined as a technological system used as a solution, even

(a)   (b)
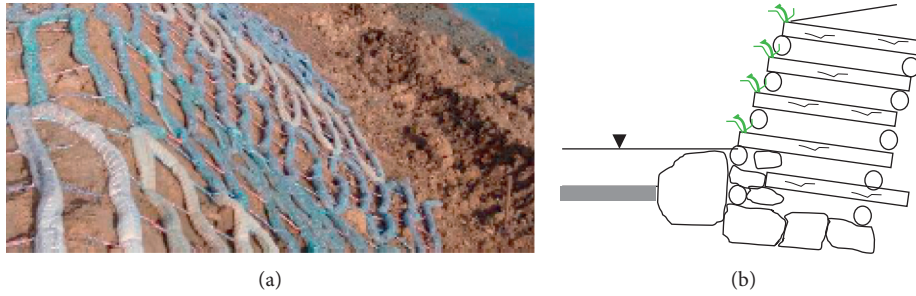
FIGURE 2: (a) Example of wool geotextiles. (b) Example of woods crib walls.

TABLE 1: Functions of vegetation in environmental engineering measures.

Function	Typology	Description
Hydrological-hydraulic	Interception	The vegetation intercepts raindrops and reduces their size and strength, thus protecting the soil from erosion caused by rain splash
	Restraint	The dense network of roots restrains bed material
	Absorption	Roots absorb water surface and underground water, thus reducing the saturation level of soil and the risk of slope failure
	Infiltration	Plants help to maintain soil porosity and permeability, increasing retention and delaying the runoff
	Evapotranspiration	Vegetation transpires water absorbed through the roots and allows it to evaporate into the air
	Surface runoff reduction	Stems and roots can reduce the velocity of surface runoff by increasing surface roughness
	Reducing flowing by stems	A portion of rainwater is intercepted by vegetation so that rainwater is stored in the stems
Environmental	Absorption	It allows the absorption of CO_2 depending on the soil fertility, type of soil, exposure, temperature trend, and the plant species
Mechanical	Catching	The loose soil materials, which roll down a slope because of gravity and erosion, are caught by planting the stems and roots
	Armouring	Vegetation can trap high-size sediments
	Reinforcing	The shear strength of the soil can be increased by planting vegetation depending on the nature of its roots
	Supporting and anchoring	Large and mature plants can stabilize layers with a tendency to slip over each other
	Draining	Surface water drains away more easily in areas with dense rooted vegetation

FIGURE 3: Example of green walls.

partial, of a generic building construction with the aim of guaranteeing several benefits for life [23].

In Europe, the use of green technology began since the 1960s. Promoters of this system were the countries of central and northern Europe: Switzerland, Austria, Finland, Norway, and Germany.

According to Abram [24], the "green roof" can be defined as a technological system realized on top of a building. Such a technological system consists of different stratifications attached to the thermal insulation element (if existing) and forming a unique system. In particular, as Figure 4 shows, this system consists of four types of layers: the vegetation layer, the protection (filtering and draining)
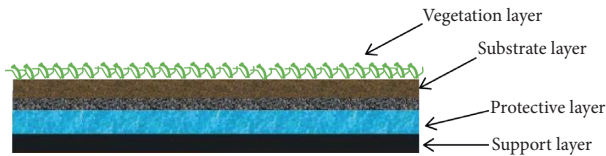
Figure 4: Scheme of the green roof system.

layers, and the supporting layer. The vegetation layer is the most essential part of the green roof. Generally, herbaceous vegetation, more precisely grass that it is very variable in quantity and grows over time, is used. The nutrition of vegetation is from the so-called growth substrate layer which could be mixed with compost and plays an important role in managing water. The protection layer could be composed of two plastic materials [25]: the first one prevents roots penetration into the support and could be made of high-density polyethylene; the second one is a layer of drainage and filtration consisting generally of polystyrene. The support layer supports all the above mentioned different layers of the green roof and could be made of wood.

Although each installation presents similar constructive characteristics, its performance could vary by region, climate, building, design, and green wall type [26]. In particular, some main elements should be considered in order to guarantee the good performance of the green roofs: (a) the roots system must not compromise the integrity and functionality of the underlying layers and in particular of the thermal insulation element; (b) it is necessary to protect the underlying waterproofing of the roof from damage and mechanical stresses caused by the weight of the overlying layers; and (c) it is necessary to guarantee the drainage and the presence of air.

Like green roofs, the "green walls" also consist of a sequence of layers organized with a precise order in the space [27, 28]. In general, passing from the outside to the building's surface, the sequence includes four layers: the vegetated layer, the substrate layer, the technological layer, and the closure layer. The vegetated layer is composed by the plants which could be of different species although always-green species are preferably used. The substrate layer represents the layer from which the plants take nutrition. The technological layer is the layer necessary for the implementation of the green package and its functionality. Finally, the closure layer is the physical element of delimitation between the sequence and the building's surface.

It should be noted that according to the used executive procedure and the plants peculiarities, three different typologies of the green wall can be distinguished: the "green facade", the "living wall", and the "garden wall". The "green facade" represents a vegetal coating of the building's surface [29]. This typology includes a simple technological layer so that either the plants are clinging directly to the building's surface (such a practice was widely used in the past) or there are specific support elements, as the wire meshes, on which the plants cling (see Figure 5(a)). Thus, the climbing plant species are generally used for this typology. Unlike the "green facade", the "living wall" is characterized by a marked integration between the building's surface and the plants (see

Figure 5(b)). In this typology, the plants are arranged directly on the closure layer [30] so that a uniform vegetal layer covering the entire building surface forms; the vegetation becomes an integrating part of the building surface itself. The "garden wall" can be considered as a subtype of the living wall [31]. The main differences with respect to the living wall are due both to the arrangements of the plant apparatus and for the material with which the substrate is made (see Figure 5(c)). In fact in the garden wall, synthetic elements are generally used for the substrate.

2.2.1. Functions and Advantages. Green roofs and walls provide many functions and offer several benefits (among others [32–35]), as schematized in Table 2. From Table 2, it can be summarized that on the aesthetic point of view, this system allows aesthetic stimulation allowing to create privacy and limiting the negative psychological effects associated with property demarcation; on the protective point of view, this system provides an additional layer of exterior insulation also limiting the thermal fluctuations; on the environmental point of view, this system allows to reduce noise, to mitigate air pollution levels by lowering extreme summer temperatures through photosynthesis. Furthermore, green walls allow both to treat water by filtering it through specific marine plants [37] and to reduce the temperature fluctuations at a wall's surface, limiting the movement of heat between building walls [38]. A recent field green wall experiment [39] has indicated a good efficiency of COD and BOD5 removal from greywater produced by an office building so that greywater reached an appropriate quality to accumulate it for its reuse for irrigation purposes [40]. This confirms that use of the green wall for greywater treatment and reuse could be a very promising additional service provided by it.

3. Discussion and Concluding Remarks

From the presented brief review of the measures for limiting the human impact in the environment, it can be concluded that in comparison with traditional engineering techniques, the use of vegetation as biomaterial presents many benefits.

In particular, from the aforementioned considerations, three general groups of benefits can be outlined: (1) technical advantages which include the protection against surface erosion, the improving of bank's stability by root reinforcement and draining of the soil, and the protection against wind; (2) environmental advantages which include the regulation of temperature and humidity close to the surface, the improving of water interception, evapotranspiration and storage, and the improving of habitat and biodiversity; and (3) aesthetic advantages which include the use of technological systems improving the aesthetic buildings' characteristics and a more appealing landscape.

An adding benefit is that related to the economic advantages. In fact, the use of vegetation in controlling measures against erosion in extra-urban sites allows the reduction of the construction and the structural maintenance costs with respect to the corresponding costs
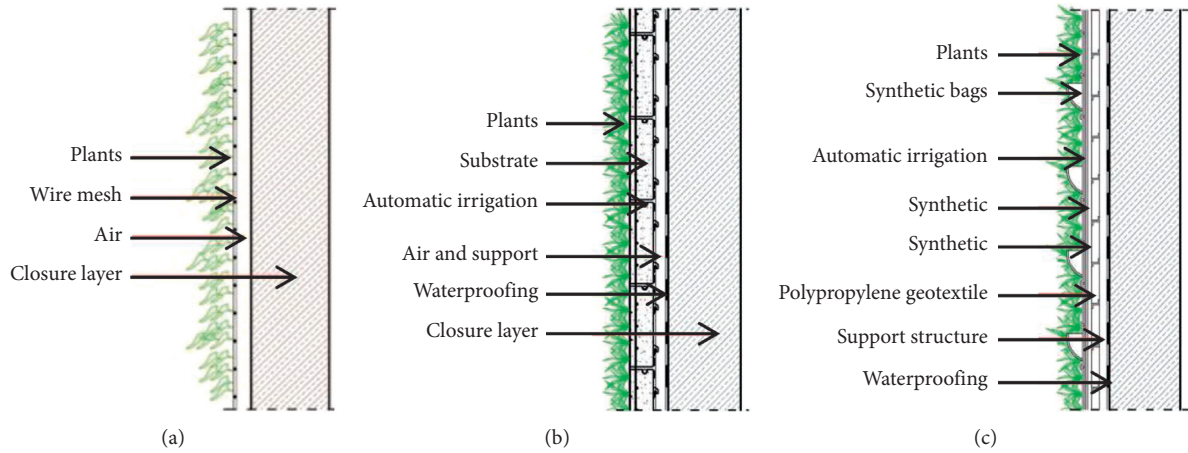
FIGURE 5: (a) Example scheme of the "green façade." (b) Example scheme of the "living wall." (c) Example scheme of the "garden wall."

TABLE 2: Functions of vegetation in green walls.

Function	Typology	Description
Aesthetic and protective function	Aesthetic improvements	Especially, green walls provide aesthetic stimulation where it would not otherwise be found. They can also serve to create privacy limiting the negative psychological effects associated with property demarcation.
	Building structure protection	Temperature fluctuations over a building's lifetime can determine damages in building facades. Green walls provide an additional layer of exterior insulation limiting thermal fluctuations. Furthermore, green walls protect exterior finishes from UV radiation and rain and decrease the effect of wind pressure [36].
Environmental	Noise reduction	The vegetated surface provided by green walls and roofs will block high-frequency sounds, and when constructed with a substrate or growing medium support, it can also block low-frequency noises.
	Increased biodiversity	Green walls can help mitigate the loss of biodiversity due to the effects of urbanization, help sustain a variety of plants, pollinators, and invertebrates, and provide habitat and nesting places for various bird species.
	On-site wastewater treatment	Several water-recycling systems can be applied to green walls. As an example, systems pump greywater through a green wall, which then passes through filters, gravel, and marine plants and treat water which is then sent to a greywater holding tank for household or irrigation use or released into the public water treatment system [37].
	Improved energy efficiency	Green walls can reduce the temperature fluctuations at a wall's surface from a range of $10–60°C$ to one of $5–30°C$, limiting the movement of heat between building walls [38].
	Reduction of the urban heat island effect	The reintroduction of vegetation into urban environments promotes the occurrence of natural cooling processes, such as photosynthesis and evapotranspiration.
	Improved exterior air quality	Green walls mitigate air pollution levels by lowering extreme summer temperatures through photosynthesis, trapping particulate matter, and capturing gases.

necessary for a classical structural measure [40]. Furthermore, the vegetation installation contributes to create areas for agricultural and recreational use. The economic advantages in the use of green walls in urban areas are especially related to the multiple benefits which they produce [41]. A green wall can act like a cooler due to plant evapotranspiration and can reduce impact of the wind by 75% and heating demand by 25% [36].

On the other side, it should be considered that in order to guarantee the efficiency of the aforementioned measures, some important elements have to be taken into account. First of all, it is really important to select local species already adapted to the growing conditions which can resist to high frequency of occurrence of high-magnitude events. Furthermore, it should be important to select species that can be used for other purposes, for example, providing fruit or leaves that can be used for other purposes. This suggests that to analyze the effective protective action of vegetation, it is important to evaluate the durability and different aspects related to the maintenance of the planted species.

In conclusion, vegetation as biomaterial in environmental engineering could exert an important role to mitigate worst effects due to anthropogenic actions. Its use offers significant economic benefits, including a longer measure's life and an increasing biodiversity; if well designed, it can offer people also the psychological benefits of nature.

Conflicts of Interest

The author declares that they have no conflicts of interest.

References

[1] V. Rahimpour, Y. Zeng, C. M. Mannaerts, and Z. Su, "Attributing seasonal variation of daily extreme precipitation events across The Netherlands," *Weather and Climate Extremes*, vol. 14, pp. 56–66, 2016.

[2] N. Christidis and P. A. Stott, "Attribution analyses of temperature extremes using a set of 16 indices," *Weather and Climate Extremes*, vol. 14, pp. 24–35, 2016.

[3] P. Kokic, S. Crimp, and M. Howden, "A probabilistic analysis of human influence on recent record global mean temperature changes," *Climate Risk Management*, vol. 3, pp. 1–12, 2014.

[4] A. T. Leiser, "Bio-technology for slope protection and erosion control," in *Proceedings of the Conference on Watershed Stewardship*, Rapid City, SD, USA, September 1998.

[5] F. I. Woodward and I. F. McKee, "Vegetation and climate," *Environment International*, vol. 17, no. 6, pp. 535–546, 1991.

[6] N. J. Georgi and J. E. Stathakopoulos, "Bioengineering techniques for soil erosion protection and slope stabilization," in *Proceedings of the 46th Congress of the European Regional Science Association, University of Thessaly*, Volos, Greece, August 2006.

[7] J. Bendix and C. R. Hupp, "Hydrological and geomorphological impacts on riparian plant communities," *Hydrological Processes*, vol. 14, no. 16-17, pp. 2977–2990, 2000.

[8] İn. Güneralp and B. L. Rhoads, "Influence of floodplain erosional heterogeneity on planform complexity of meandering rivers," *Geophysical Research Letters*, vol. 38, no. 14, 2011.

[9] C. L. Jang and Y. Shimizu, "Vegetation effects on the morphological behavior of alluvial channels," *Journal of Hydraulic Research*, vol. 45, no. 6, pp. 763–772, 2005.

[10] J. McKean, D. Nagel, D. Tonina et al., "Remote sensing of channels and riparian zones with a narrow-beam aquatic-terrestrial LIDAR," *Remote Sensing*, vol. 1, no. 4, pp. 1065–1096, 2009.

[11] E. Perucca, C. Camporeale, and L. Ridolfi, "Influence of river meandering dynamics on the riparian vegetation pattern formation," *Journal of Geophysical Research*, vol. 111, article G01001, 2006.

[12] E. Perucca, C. Camporeale, and L. Ridolfi, "Significance of the riparian vegetation dynamics in meandering river morphodynamics," *Water Resources Research*, vol. 43, no. 3, article W03430, 2007.

[13] C. Camporeale, P. Perona, A. Porporato, and L. Ridolfi, "On the long-term behavior of meandering rivers," *Water Resources Research*, vol. 41, no. 12, 2005.

[14] A. Gurnell, "Plants as river system engineers," *Earth Surface Processes and Landforms*, vol. 39, no. 1, pp. 4–25, 2014.

[15] H. M. Nepf, "Hydrodynamics of vegetated channels," *Journal of Hydraulic Research*, vol. 50, no. 3, pp. 262–279, 2012.

[16] D. Termini, "Flexible vegetation behaviour and effects on flow conveyance: experimental observations," *International Journal of River Basin Management*, vol. 13, no. 4, pp. 401–411, 2015.

[17] C. Liu and H. Nepf, "Sediment deposition within and around a finite patch of model vegetation over a range of channel velocity," *Water Resources Research*, vol. 52, no. 1, pp. 600–612, 2016.

[18] A. Crosato, F. B. Desta, J. Cornelisse, F. Schuurman, and W. S. J. Uijttewaal, "Experimental and numerical findings on the long-term evolution of migrating alternate bars in alluvial channels," *Water Resources Research*, vol. 48, no. 6, article w06524, 2012.

[19] O. Ogbobe, K. S. Essien, and A. Adebayo, "A study of biodegradable geotextiles used for erosion control," *Geosynthetics International*, vol. 5, no. 5, pp. 545–553.

[20] J. AdebayoEssien, J. Grzybowska-Pietras, A. Gawłowski, M. Rom, S. Przybylo, and R. Laszczak, "Application of wool geotextiles for the protection of steep slopes," *Procedia Engineering*, vol. 200, pp. 112–119, 2017.

[21] C. Zarotti and M. Zarotti, "L'interazione pendio atmosfera: piante erbacee perenni e autoctone a radicazione profonda e resistente per la realizzazione e protezione delle opere di captazione e regimentazione delle acque meteoriche e suprficiali," in *Proceedings of the XXXVI Convegno Nazionale di Idraulica e Costruzioni Idrauliche*, Ancona, Italy, September 2018, in Italian.

[22] L. Bertoldi, M. Massironi, D. Visonà et al., "Mapping the Buraburi granite in the Himalaya of Western Nepal: remote sensing analysis in a collisional belt with vegetation cover and extreme variation of topography," *Remote Sensing of Environment*, vol. 115, no. 5, pp. 1129–1144, 2011.

[23] L. G. Lanza, "Coperture a verde e ambiente urbano sostenibile," in *IA Ingegneria Ambientale*, ANNO XXXVIII N.3, 2009, in Italian.

[24] P. Abram, *Giardini Pensili-Coperture a Verde e Gestione Delle Acque Meteoriche, Sistemi Editoriali Professionisti, Tecnici e Imprese, AS11*, Gruppo Editoriale Esselibri-Simone, Napoli, Italy, 2004, in Italian.

[25] D. Morau, T. Rabarison, and H. Rakotondramiarana, "Life cycle analysis of green roof implemented in a global south low-income country," *British Journal of Environment and Climate Change*, vol. 7, no. 1, pp. 43–55, 2017.

[26] K. Liu and B. Bass, "Performance of green roof systems," in *Proceedings of the Cool Roofing Symposium*, pp. 1–18, Atlanta, GA, USA, May 2005.

[27] Ö. T. Burhan and E. Karaca, *Vertical Gardens Advances in Landscape Architecture*, Intech Open Science, London, UK, 2013.

[28] R. Jain and T. Janakiram, *Vertical Gardening: A New Concept of Modern Era Commercial Horticulture*, N. L. Patel, S. L. Chawla, and T. R. Ahlawat, Eds., New India Publishing Agency, New Delhi, India, 2016.

[29] M. Köhler, "Green facades—a view back and some visions," *Urban Ecosystems*, vol. 11, no. 4, pp. 423–436, 2008.

[30] S. Loh, "Living walls: a way to green the built environment," *BEDP Environment Design Guide Technology*, vol. 1, no. 26, pp. 1–7, 2008.

[31] J. Binabid, *Vertical Garden: The Study of Vertical Gardens and Their Benefits for Low-Rise Buildings in Moderate and Hot Climates*, University of Southern California, ProQuest LLC, Los Angeles, CA, USA, 2010.

[32] E. P. D. Barrio, "Analysis of the green roofs cooling potential in buildings," *Energy and Buildings*, vol. 27, no. 2, pp. 179–193, 1998.

[33] N. Dunnett, A. Nagase, R. Booth, and P. Grime, "Influence of vegetation composition on runoff in two simulated green roof experiments," *Urban Ecosystems*, vol. 11, no. 4, pp. 385–398, 2004.

[34] E. Eumorfopoulou and D. Aravantinos, "The contribution of a planted roof to the thermal protection of buildings in Greece," *Energy and Buildings*, vol. 27, no. 1, pp. 29–36, 1998.

[35] M. Gernot, *Dämpfung von Hochfrequenter Strahlung durch Lehmbaustaffe und Gründecher*, University of Kassel, Kassel, Germany, 2006.

[36] S. W. Peck, C. Callaghan, M. E. Kuhn, and B. Bass, *Benefits, Barriers and Opportunities for Green Roof and Vertical Garden Technology Diffusion*, Canada Mortgage and Housing Corporation, Ottawa, ON, Canada, 1999.

[37] C. Shirley-Smith, "The sustainability value of the green roof water recycling system in urban communities," WATERSAVENetworkEvent, October 2008, http://www.watersave.uk.net/Presentations/Chris_ShirleySmith.pdf.

[38] G. Minke and G. Witter, *Haeuser mit Gruenem Pelz, Ein Handbuch zur Hausbegruenung*, Verlag Dieter Fricke GmbH, Frankfurt, Germany, 1982.

[39] F. Masi, R. Bresciani, A. Rizzo et al., "Green walls for greywater treatment and recycling in dense urban areas: a case-study in Pune," *Journal of Water, Sanitation and Hygiene for Development*, vol. 6, no. 2, pp. 342–347, 2016.

[40] G. Başdoğan and A. Çiğ, "Ecological-social-economical impacts of vertical gardens in the sustainable city model," *Yuzuncu Yıl University Journal of Agricultural Sciences (YYU J AGR SCI)*, vol. 26, no. 3, pp. 430–438, 2016.

[41] L. Curtis and M. Stuart, *Enhancing CHBE Indoor Air Quality: Biowall Technology, UBC Social Ecological Economic Development Studies (SEEDS) Student Report*, University of British Columbia, Vancouver, BC, Canada, 2010.

Research Article

Strength and Deformation Properties of Fiber and Cement Reinforced Heavy Metal-Contaminated Synthetic Soils

Qiang Tang [ID],[1,2] **Peixin Shi** [ID],[1] **Yu Zhang,**[1] **Wei Liu,**[1] **and Lei Chen**[1]

[1]*School of Rail Transportation, Soochow University, Suzhou, China*
[2]*National Engineering Laboratory of Highway Maintenance Technology, Changsha University of Science & Technology, Changsha, China*

Correspondence should be addressed to Peixin Shi; pxshi@suda.edu.cn

Heavy metals are not only hazardous to environment and public health, but they degrade the physicochemical and biological properties of soils increasing difficulty to the redevelopment of contaminated sites. This study proposes a method for reinforcing contaminated soils with fiber and cement. The feasibility of using wheat straw as fiber reinforcement is discussed. The strength of heavy metal-contaminated soil reinforced with wheat straw and cement is investigated through laboratory testing. Twelve groups of soil samples were prepared at three fiber contents (i.e., 0.1%, 0.2%, and 0.3% by weight), three water contents (i.e., 9%, 12%, and 15%), and three cement contents (i.e., 5%, 7.5%, and 10% by weight). Unconfined compression strength (UCS) was tested after 28 days of curing period and various freeze-thaw cycles. The testing results show that the increase in the number of freeze-thaw cycles results in the decrease of UCS. The inclusion of fiber reinforcement within cemented soil causes an increase in the UCS and changes the brittle behavior of cemented soil to a more ductile one. The UCS of the fiber-reinforced soils first increases, then decreases with the increase of water content, and reaches the maximum value at the optimum moisture content.

1. Introduction

With rapid industrialization, soil contamination by heavy metals has become one of the main global environmental problems [1–5]. Heavy metals in soil are highly toxic, persistent, and nonbiodegradable, which will impair the natural ecosystem services and eventually damage human health via the food chain [6–10]. Furthermore, heavy metals have adverse effects on the mechanical properties of soils, which results in unfavorable conditions for the redevelopment of contaminated sites [11]. Solidification/stabilization (S/S) is an effective and economical method to heavy metal-contaminated soil treatment and has attracted increasing attention in the past decades [12, 13]. S/S technology according to different disposal locations can be divided into in situ and ex situ. Ordinary Portland cement, as a common binder utilized in S/S remediation, encapsulates heavy metal ions in a monolithic solid of high structural integrity to reduce further mobility of heavy metal ions

[11, 12]. Du et al. evaluated the environmental characteristics of cement-solidified heavy metal-contaminated soil by using the finite element model. The results found that heavy metals leaching concentration is less than the maximum allowable value after the cement-solidified soil as foundation material served 50 years [14]. More importantly, cement-solidified soils have a certain strength and can be used as the bearing material for shallow foundations and base for roadway or railway embankments [11].

Previous studies show that the presence of heavy metals in soils creates a retardant effect on the hydration reaction of cement-based binders [15]. Because the quantity of hydration products (e.g., calcium-silicate-hydrate (C-S-H) gels) in cement-solidified soils is positively correlated with the strength, the retarded formation of hydration products caused by heavy metals leads to a lower strength and modulus [16]. Buj et al. found that the presence of high concentrations of heavy metals noticeably impacted the strength of cemented soil matrix by creating defects at

crystalline matrices [17]. Based on the measured unconfined compressive strength (UCS) of soil samples at different heavy metal concentrations, Du et al. found that the UCS of stabilized Zn-contaminated soils decreased slightly as Zn concentration increased [18]. When exposed to certain long-term external conditions such as freeze-thaw cycling, cracks occur easily in the cement-solidified mixture and the UCS decreases with alternative cycles [19]. Previous studies showed that the initial cracking and subsequent frost lens formation increased the potential to damage of the soil-cement materials [20]. Lake et al. showed that the specimens exposed to freeze-and-thaw conditions were more prone to cracking because the freezing generates excess pressure exceeding the tensile strength of the material [21].

Fiber reinforcement increases the modulus and inhibits cracking of soils. It serves as an effective method to treat cement-solidified heavy metal-contaminated soils. Wheat straw, the residue after wheat harvest, is produced in large quantities worldwide [22]. As a large agricultural country, the annual output of straw in China is about 7 million tons, accounting for about 20~30% of the total amount in the world [23]. Currently, the direct open burning is a major way to destroy the straw in China. The particulate matter and gaseous pollutants released during straw burning create a serious negative effect on the atmospheric environment, climate change, and ecological system [24, 25]. In China, straw open burning may lead to closing of highways and flight delay [26]. The application of agricultural crop residues may open new markets for wheat straw and improve the rural agricultural economy [27]. In this paper, wheat straw and cement were chosen as reinforcing element and solidified material, respectively. Cement seals wheat fibers in a dense matrix to increase strength and durability, and wheat fibers change the brittleness of the cemented soil to a more ductile one. The influence of cement content, water content, quantity of fibers, and alternative cycles of freeze-thaw is evaluated in terms of the compressive strength and failure strain.

2. Materials and Methods

2.1. Materials. To avoid the adverse effects of material in homogeneity on the strength and deformation properties of natural soils, laboratory-made sand-clay mixtures were used for testing. The synthetic soil consisted of 70% sand and 30% kaolin and can be classified as sandy loam texture according to the *Classification and Codes for Chinese Soil* (GB/T 17296-2000). A maximum dry density of 1.88 g/cm^3 and a optimum water content of 12% were determined by the compaction tests based on *Standard for Soil Test Method* (GB/T 50123-1999). Clay is commercial kaolin which was sampled from Suzhou Kaolin Co. Ltd., China. Commercial sand with a mean diameter of approximately 1.0 mm was collected from Shengfa Building Materials Co. Ltd., China. As a solidified material, the commercially available Portland cement (i.e., PG325) was purchased from the cement plant in Anhui, China. The cement mainly consists of 6 ~ 15% active additive and 85~94% cement. The physical properties and chemical composition of the soil and cement are summarized in

Table 1. Prior to use, the soil and cement were dried in an oven at a temperature of 105°C for at least 24 hours (101-A, Leao, China) and sieved (1 mm for soils; 0.3 mm for cement) to remove impurities. The chemical, lead nitrate, $Pb(NO_3)_2$ (analytical reagent), was obtained from Suzhou Experiment Instrument Co. Ltd., China. The water used was deionized water (DIW), prepared from tap water via distillation (RFD240NA, Advantec, Japan).

Local wheat straw fibers were used as the reinforcement material. Agroresidues were obtained from local farms and homogenized carefully. The wheat straw is composed (on a mass basis) of $57 \pm 10\%$ internodes, $18 \pm 3\%$ leaves, $10 \pm 2\%$ nodes, $9 \pm 4\%$ chaff, and $6 \pm 2\%$ rachis [28]. The stem of wheat straw was selected, cleaned, and grouped for pretreatment. The pretreatment process of wheat straw is shown in Figure 1. The wheat straw fibers were dried at the temperature of 65°C [29]. After drying, they were cleaned and the leaves, spikes, sheaths, and fragments were removed. The samples were then collected for microstructure observations using a scanning electron microscope (SEM) (S-4700, Hitachi, Japan). A homogenous group of wheat fibers with approximately equal diameter was selected and chopped into the required length using a grain straw shredder (YB-1000A, Sufeng Industrial, China), operating at 25,000 rpm and equipped with a 200 mm replaceable blade. The wheat straw fibers were kept in sealing bags for storage at room temperature. The straw fibers after milling were about 10~20 mm in length and 2~3 mm in diameter. The fiber compositions of the wheat straw fibers are celluloses, lignin, and hemicelluloses, and the total inorganic content is about 15% [29].

2.2. Experimental Program. As Pb was commonly encountered in contaminated sites worldwide, especially in China, it was selected as the target heavy metal in this work [30]. To reach the target concentration of Pb(II) (1 mg/g and 10 mg/g), a certain dose of $Pb(NO_3)_2$ was dissolved in a small amount of DIW and was then poured into the dry synthetic soil. Unreinforced samples and wheat straw fiber-reinforced samples were homogenized with the cement at three different cement/soil ratios (5%, 7.5%, and 10%) after blending for 2~3 min in a blender. Simultaneously, the exact amount of DIW was weighted and slowly poured into the mixture to prevent fiber segregation during sample formation. The water content of the three specimens was 9%, 12%, and 15%, respectively. Wheat straw fibers were applied as a reinforcement material at the percentage of 0.1, 0.2, and 0.3 by weight of soil. The mixing process for the soil, water, cement, and fibers was stopped when the fibers were evenly distributed and randomly oriented throughout the soil. After mixing, the mixture was shaped in a mold with a length of 100 mm and an inner diameter of 50 mm with full compaction. To ensure uniformity, the samples were compacted in five layers. The height of each layer was approximately 1/5 of the specimen height. A rammer was dropped 12 times from a height of 200 mm on each layer of the specimen. After that, the mixtures were demolded and cured (90 ± 2% humidity; 20 ± 2°C) for 28 days in a curing box (HBY-15B,

TABLE 1: Properties of soils and cement.

Property	Standard	Unit	Kaolin	Sand	Cement
Moisture	JIS A 1203	%	2.90	0.39	0.5
pH	JGS 0211		4.70	7.50	10
EC	JGS 0212	mS/cm	0.42	0.06	
Grain size distribution	GB/T 50123-1999				
Clay fraction ($\leq$0.005 mm)		%	56.40	0.10	2.3
Silt fraction (0.075–0.005 mm)		%	18.80	2.98	97.7
Sand fraction (2-0.075 mm)		%	24.80	96.92	0
N_2-BET					
Correlation coefficient (R^2)			0.99	0.99	0.99
Specific surface area		m^2/g	29.41	0.014	0.35
Diameter		nm	29.97		
Pore volume		cm^3/g	0.22		
Chemical composition					
SiO_2		%	45.32	93.57	1.94
Fe_2O_3		%	0.14	0.74	0.23
CaO		%	0.02	1.87	31.31
Al_2O_3		%	51.13	2.12	0.9
MgO		%	0.28	0.28	0.29
SO_3		%	0.09		43.49
TiO_2		%	0.68	0.027	
Na_2O		%	0.56	0.48	
K_2O		%	1.54	0.59	
Cl^-		%	0.01		

FIGURE 1: Pretreatment process of wheat straw. (a) Local wheat straw fibers. (b) Cleaned and dried fibers. (c) Milled fibers. (d) Fibers kept in a sealing bag.

Donghua, China). Table 2 provides the details of the different water, cement, and fiber content of the mixtures. Three replicates were analyzed for each set of testing.

During freezing and thawing, the specimens were placed into a refrigerator at $-10°C$ for 6 hrs and then at $+10°C$ for thawing phase for 6 hrs as suggested by Qi et al. [31]. Observation during testing shows that, after the six-hour freezing or thawing, the specimen height keep virtually remains constant. The unreinforced samples were subjected to 0, 3, 6, and 9 freeze-thaw cycles, and the wheat straw fiber-reinforced samples were subjected to 9 freeze-thaw cycles. The UCS of the unreinforced and wheat straw fiber-reinforced soil samples was tested as per ASTM D 2166-91 using a microcomputer-controlled electronic testing machine (LDS-50, Chenda, China) with a strain rate of 1 mm/min. The testing machine (MTS 10/GL) has a loading capacity of 50 kN, as referenced to the study of Koohestani et al. [32]. The loads were recorded at the point of sample fracturing, and the UCS

was determined using the formula $P = F/A$, where P is the compressive strength (MPa), F is the load (N) at fracture, and A is the area of loading cross section (mm^2). All the tests were replicated, and the average values were reported.

3. Results and Discussion

3.1. Results. It is well documented that the USC and failure strain of cement-based samples can reflect directly the degree of deterioration caused by freeze-thaw attacks. Figure 2 shows the variation of the UCS of the cement-based solidification samples under different freeze-thaw cycles. Figure 3 shows the variation of the failure strain of the samples subjected to different freeze-thaw cycles. As seen in Figure 2, the maximum UCS is achieved with the specimens free from freeze-thaw cycles. The UCS decreased with alternative cycles. Figure 2(a) shows that the largest strength reduction was about 56.1% that occurred after the 9th cycle.

Table 2: Composition and properties of the soil mixtures.

Cycles	Pb concentration (%)	Water content (%)	Cement content (%)	Fiber content (%)
Unreinforced				
		9	7.5	0
	0.1	12	7.5	0
0		15	7.5	0
		12	5	0
	1	12	7.5	0
		12	10	0
		9	7.5	0
	0.1	12	7.5	0
3		15	7.5	0
		12	5	0
	1	12	7.5	0
		12	10	0
		9	7.5	0
	0.1	12	7.5	0
6		15	7.5	0
		12	5	0
	1	12	7.5	0
		12	10	0
		9	7.5	0
	0.1	12	7.5	0
9		15	7.5	0
		12	5	0
	1	12	7.5	0
		12	10	0
Reinforced				
		9	7.5	0.1
		9	7.5	0.2
		9	7.5	0.3
		12	7.5	0.1
	0.1	12	7.5	0.2
		12	7.5	0.3
		15	7.5	0.1
		15	7.5	0.2
9		15	7.5	0.3
		12	5	0.1
		12	5	0.2
		12	5	0.3
		12	7.5	0.1
	1	12	7.5	0.2
		12	7.5	0.3
		12	10	0.1
		12	10	0.2
		12	10	0.3

According to Mehta and Monteiro, the pores in hardened cement paste can be divided into three main groups according to their form and size: capillary, gel, and air pores [33]. During the freezing and thawing processes, water firstly enters the biggest pores of hardened cement paste and subsequently reaches the smaller pores. According to Everett, ice crystals in the pores tend to grow continuously and penetrate deeper into smaller pores of the hardened cement paste and thus fill capillary pores with water or freezing solution [34]. When water or freezing solution freezes, the volume of water stored in micropores increases by 9%, the hardened cement paste generates internal stresses, and finally crumbles [35, 36].

Cement treatment strengthens the fabric of clays at the intercluster spacing and forms strong bonds with the fabric. According to Kalliopi, the destructive effect during freezing depends on the content of water in hardened cement paste [37]. Figure 2(a) shows that the UCS of the samples increased when the water content increased from 9% to 12% but decreased when the water content increased from 12% to 15%, indicating that there is a threshold value of water content beyond which the UCS decreases with increasing water content. This is because that, with high water content, the cohesive force of the soil subject to freeze-thaw cycles is lower than that before freeze-thaw cycles. The growth of ice crystals destroys the connection between soil particles and the structure of products of hydration.

The effects of freeze-thaw cycles on the UCS varied depending on the cement percentage added to the specimens. Figure 2(b) shows that the UCS increased with the increase of cement content after 9 freeze-thaw cycles. The UCS of the unreinforced samples with 5%, 7.5%, and 10% cement were 0.06, 0.26 and 0.44 MPa, respectively. The increase in strength reflected the ongoing hydration reaction during which the strong adhesive products (e.g., C-H-S gels) were generated to provide high bearing capacity against loading [38]. Figure 3(b) shows the ductility of the samples decreased with the increase of cement content. After 9 freeze-thaw cycles, the failure strain of the mixtures with 5%, 7.5%, and 10% cement was 0.7%, 0.63%, and 0.57%, respectively.

Figure 2 further shows that the concentration of heavy metal had a significant impact on the strength of cement stabilized soil. For the 12% water + 7.5% cement samples, the increase of the Pb(II) concentration from 1 mg/g (0.1%, Figure 2(a)) to 10 mg/g (1%, Figure 2(b)) resulted in a decrease of the UCS by 71.9%, 83.3%, 87.4%, and 86.2%, respectively, after subjecting to 0, 3, 6, and 9 freeze-thaw cycles, respectively. This is because the presence of Pb(II) has a negative effect on the hydration reaction of cement and hinders the hydration reaction of cement.

Figures 4 and 5 plot the UCS and the failure strain of wheat straw-reinforced samples with various fiber percentages subjecting to 9 freeze-thaw cycles, respectively. These figures show that the addition of wheat straw increased the UCS of soil and restrained the deformation of the samples. As shown in Figure 4(b), the maximum values of UCS observed in 0.1% fiber with 5%, 7.5%, and 10% cement content were 1.47, 1.59, and 2.9 MPa, respectively, which were 24.5, 6.1, and 6.6 times higher than that of unreinforced samples.

Figure 4(a) shows that, with the increase of the fiber content, the UCS increased first, reached the maximum value when the fiber content was 0.1%, and then reduced. Figure 4(a) also shows that, with the increase of the water content, the UCS increased when the water content was relatively low (e.g., 9% and 12%). When the water content was relatively high (e.g., 15%), the UCS kept virtually constant or decreased, depending on the fiber content. Taking 0.2% fiber as an example, the UCS of the reinforced soil with 9, 12, and 15% water content was 3.25, 5.18, and 3.45 MPa, respectively.

The failure strains obtained from the unconfined compression tests are given in Figure 5. The comparison with the
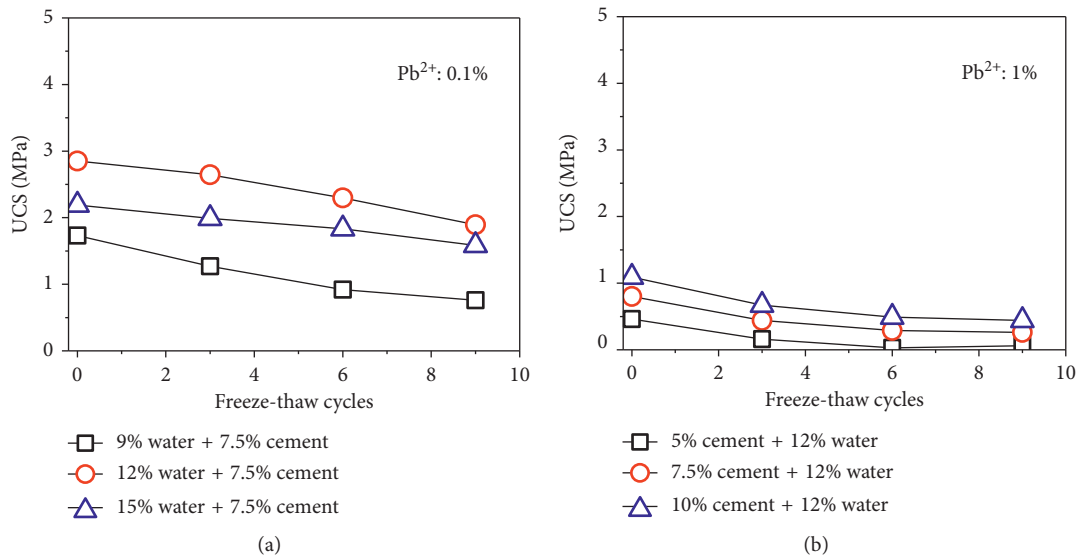
FIGURE 2: UCS of unreinforced samples during freeze-thaw cycles. (a) Various percentages of water content based on 7.5% cement + 0.1% Pb(II). (b) Various percentages of cement content based on 12% water + 1% Pb(II).
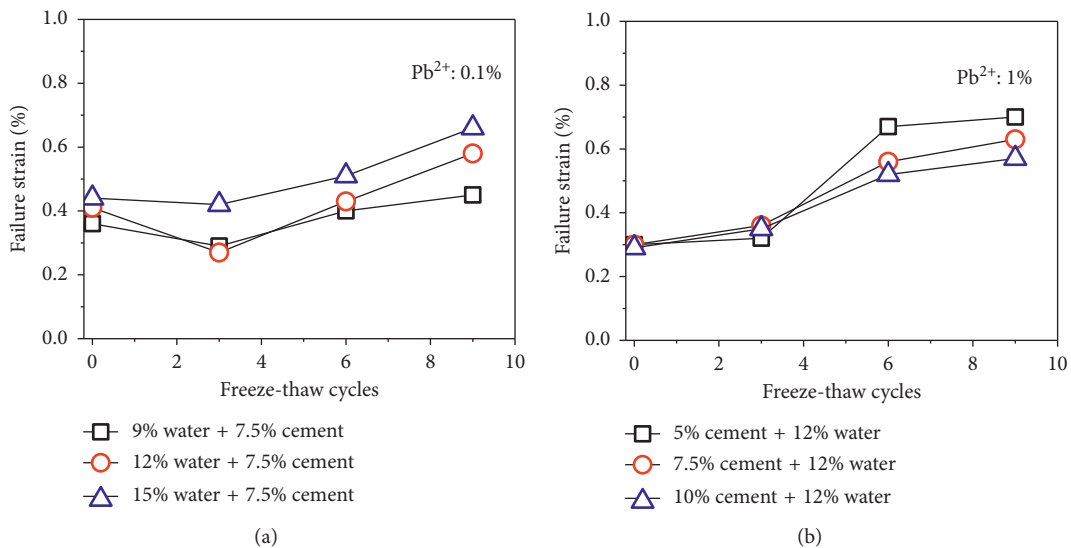
FIGURE 3: Failure strain of unreinforced soil samples during freeze-thaw cycles. (a) Various percentages of water content based on 7.5% cement + 0.1% Pb(II). (b) Various percentages of cement content based on 12% water + 1% Pb(II).

unreinforced samples shows that the inclusion of fibers within the cemented soil reduced the failure strain. As shown in Figure 5(a), the failure strain of three different cement content samples with 0.1% fiber is 0.33 (5% cement), 0.31 (7.5% cement), and 0.43% (10% cement), respectively. Compared with unreinforced samples, the failure strains of cement-fiber samples reduce by 52.9%, 50.8%, and 24.6%. As such, the fibers incorporated into cement-based material increase the deformation resistance of the samples by inhibiting the crack generation with the samples.

3.2. Mechanism. The test results in this study suggest that the strength and deformation behaviors of cemented soil reinforced by wheat straw were considerably affected by fiber content, cement content, and water content. The integrality and strength of reinforced soil can be enhanced by inclusion of randomly distributed wheat straw, and the deformation can be restrained. It is generally agreed that reinforcement plays an important role in the development of UCS. The distributed discrete fibers act as a spatial three-dimensional network to interlock soil grains, help grains to form a unitary coherent matrix, and restrict the displacement. Consequently, the stretching resistance between clay particles and strength was improved. As a natural fiber material, wheat straw has tensile strength which makes it suitable for soil reinforcement [39]. Because of the interfacial force, the fibers in the matrix are difficult to slide and can acquire tensile stress, as the schematic diagram shown in Figure 6. When the specimens are under tension, the "bridge" effect of the

(a)

(b)
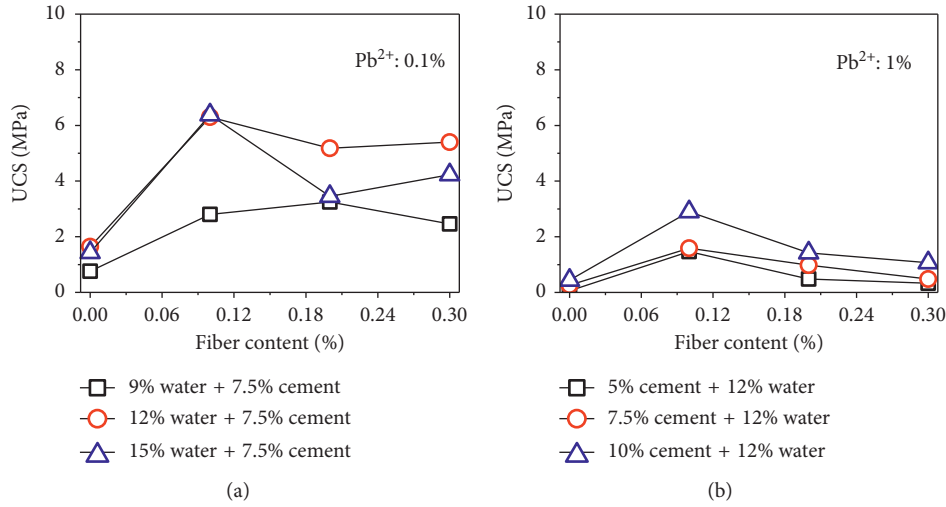
FIGURE 4: UCS of fiber-reinforced samples under 9 cycles. (a) Various percentages of water content based on 7.5% cement + 0.1% Pb(II). (b) Various percentages of cement content based on 12% water + 1% Pb(II).

(a)

(b)
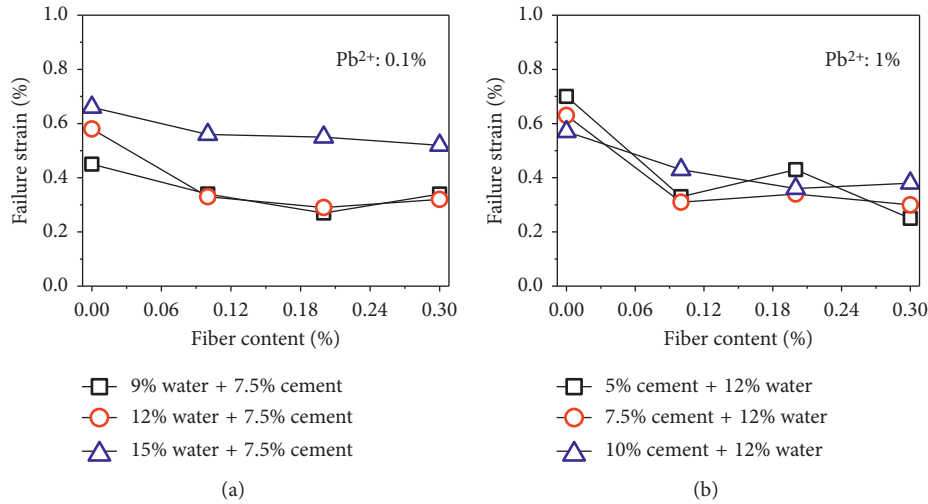
FIGURE 5: Failure strain of fiber-reinforced soil samples under 9 cycles. (a) Various percentages of water content based on 7.5% cement + 0.1% Pb(II). (b) Various percentages of cement content based on 12% water + 1% Pb(II).
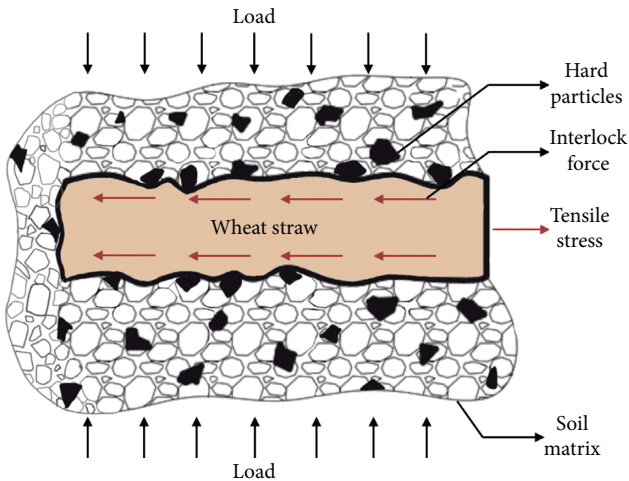
FIGURE 6: Schematic diagram of interfacial interaction between wheat straw and soil.

fibers, as shown in Figure 7, can efficiently impede further development of tensile cracks and deformation of the soil. As a result, the fiber-reinforced soil demonstrated a more ductile behavior.

Several studies indicated that the fiber sliding resistance was strongly dependent on the fiber surface roughness [40–42]. As the fibers were mixed and the samples were compacted, the hard particles (such as sands) of mixtures impacted and abraded the fiber surface, causing plastic deformation and even removal of part of the surface layer. The pits and grooves formed on the fiber surface constituted an interlock and improved the interactions between fiber surface and soil matrix. The SEM observations on the surface of wheat straw, as presented in Figure 8, show that the wheat straw surface was covered by pits and grooves. The addition of wheat straw fiber leads to a significant increase in UCS of the soil samples, and there is an optimum wheat fiber content at which the UCS reaches maximum according to
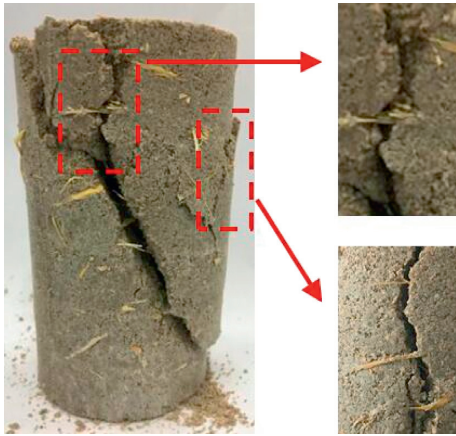
FIGURE 7: "Bridge" effect of wheat straw in cemented soil.
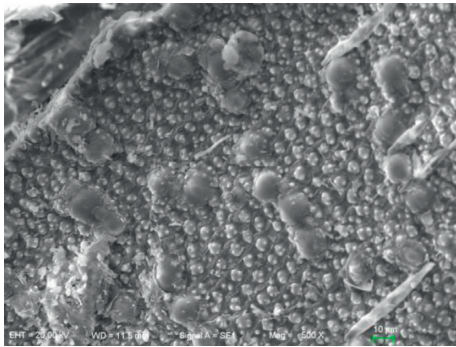
FIGURE 8: SEM images of wheat straw.

the study Qu and Sun; if the fiber content exceeds the optimum content, fiber overlapping may occur [43]. The frictional resistance between fibers is smaller than that between soil particle and fiber. In this case, increasing fiber content will lower the strength of reinforced soil. Prabhakara and Sridhar also come to the similar conclusion. This is the reason for the reduction of UCS after 0.1% fiber content [44].

It should be noted that wheat straw fibers are very easily affected by the presence of salts in soils, biological degradation, and ultraviolet degradation. Only when the wheat straw fibers are wrapped up to block its direct contact with water and air, they may be spared from the environmental degradation [45]. According to Tang et al., the fiber surface is attached by hydrated products of the cement [46]. It is known that the by-products of the cement possess higher strength and cementation than that of the clay grains. Therefore, the strength of fiber-reinforced cemented soil increases with increasing cement content. Network-like hydration crystals were wrapped around the fiber tightly that effectively restricted the fiber's relative movement and increased the reinforcement benefit significantly. The high degree of stiffness of the attached hydration crystals also toughened the distributed fibers, which act similarly to plant roots in distributing the stresses in a broader area and inhibiting fissure propagation. Therefore, the combined fiber and cement inclusions increase the efficiency of transfer of the load from matrix to fibers. Furthermore, the hydration of

the cement binds soil particles together and makes the matrix more compacted, causing an increase in normal stress around the fiber body and the effective contact area. Tagnit-Hamou et al. considered that, during cement hydration, the exothermic effect causes localized damage to the surface of the fibers [41]. The hardness of the superficial layer decreases and allows the insertion of crystals. Meanwhile, during mixing, filler grains cause grooves and stripping. Fiber roughness increases and allows a better adherence to the paste which results in the static friction coefficient between fiber and composite matrix increased [41, 46].

With the increase of water content, the UCS of fiber-reinforced samples first increases and then decreases. This phenomenon indicates that the moisture content has a significant impact on the UCS of wheat straw-reinforced soil. Only when the water content of reinforced soil reaches a certain value can wheat straw produce the best result. The low water content will lead to the drying of the soil, and the deformation of the reinforcement and the soil cannot be coordinated. According to Huang et al., the cohesive function between hydrated film and soil particles will gradually increase with the increase of water content when the water content is less than the optimum moisture content [47, 48]. The increase of cohesive force improves the friction between wheat straw and soil so that the tensile properties of straw are fully reflected, resulting in an increase of the UCS. However, with the increase of water content, the hydrated film around soil grains thickens, improving the lubrication between the reinforcement and soil grains. Furthermore, when the hydrated film in the contact of soil particles is squeezed, the bounded water becomes free water and reduces the cohesive force of soil.

4. Conclusions

In this paper, a series of experiments were conducted to evaluate the effects of randomly distributed short wheat straw fiber reinforcement on the strength behavior of cemented soils. The effect of wheat straw fiber and cement inclusions on UCS, failure strain, and elastic modulus of heavy metal-contaminated soil specimens was determined. According to the testing results, the mechanical properties of reinforced soil change with increasing the fiber content until an optimum content at which the UCS of the reinforced soil reaches maximum. The optimum fiber content is found to be 0.1% in the current tests.

The addition of fibers can effectively prevent the damage caused by freeze-thaw cycles to the soils. The "bridge" effect of wheat straw can efficiently impede the further development of tensile cracks and deformation of the soil. Increasing cement content could increase the UCS and decrease the failure strains of fiber-reinforced cemented soil. The by-products of the cement possess higher strength and cementation than those of the clay grains. In fiber-reinforced cemented soil, the interactions between the fiber surface and the hydrated products play a major role on the strength characteristic. On account of above findings, it is recommended that, in cold climates, where soil is affected by freeze-thaw cycles, wheat fibers can be applied in the field of geotechnical engineering from an environmental point of view.

Data Availability

All the data presented in the manuscript were obtained from laboratory tests at Soochow University in Suzhou, China. All the laboratory testing data were presented in the figures and tables in the manuscript. We will be very pleased to share our all the raw data. If needed, please contact the corresponding author.

Conflicts of Interest

The authors declare that they have no conflicts of interest.

Acknowledgments

References

[1] Q. Tang, F. Gu, Y. F. Gao, T. Inui, and T. Katsumi, "Desorption characteristics of Cr(III), Mn(II) and Ni(II) in contaminated soil using citric acid and citric acid containing wastewater," *Soils and Foundations*, vol. 58, no. 1, pp. 50–64, 2018.

[2] Q. Tang, H. J. Kim, K. Endo, T. Katsumi, and T. Inui, "Size effect on lysimeter test evaluating the properties of construction and demolition waste leachate," *Soils and Foundations*, vol. 55, no. 4, pp. 720–736, 2015.

[3] Y. Zhang, Q. Tang, S. Chen, F. Gu, and Z. Z. Li, "Heavy metal adsorption of a novel membrane material derived from senescent leaves: kinetics, equilibrium and thermodynamic studies," *Membrane Water Treat*, vol. 9, no. 2, pp. 95–104, 2018.

[4] Q. Tang, F. Gu, Y. Zhang, Y. Zhang, and J. Mo, "Impact of biological clogging on the barrier performance of landfill liners," *Journal of Environmental Management*, vol. 222, pp. 44–53, 2018.

[5] Q. Tang, T. Katsumi, T. Inui, and Z. Li, "Influence of pH on the membrane behavior of bentonite amended Fukakusa clay," *Separation and Purification Technology*, vol. 141, pp. 132–142, 2015.

[6] Q. Tang, T. Katsumi, T. Inui, and Z. Li, "Membrane behavior of bentonite-amended compacted clay," *Soils and Foundations*, vol. 54, no. 3, pp. 329–344, 2014.

[7] Q. Tang, X. Tang, Z. Li et al., "Zn(II) removal with activated firmiana simplex leaf: kinetics and equilibrium studies," *Journal of Environmental Engineering*, vol. 138, no. 2, pp. 190–199, 2012.

[8] Q. Tang, X. Tang, M. Hu, Z. Li, Y. Chen, and P. Lou, "Removal of Cd(II) from aqueous solution with activated Firmiana Simplex Leaf: behaviors and affecting factors," *Journal of Hazardous Materials*, vol. 179, no. 1–3, pp. 95–103, 2010.

[9] Q. Tang, T. Zhou, F. Gu, Y. Wang, and J.-m. Chu, "Removal of Cd(II) and Pb(II) from soil through desorption using citric acid: kinetic and equilibrium studies," *Journal of Central South University*, vol. 24, no. 9, pp. 1941–1952, 2017.

[10] Q. Tang, W. Liu, Z. Li, Y. Wang, and X. Tang, "Removal of aqueous Cu(II) with natural kaolin: kinetics and equilibrium studies," *Environmental Engineering and Management Journal*, vol. 17, no. 2, pp. 467–476, 2018.

[11] Q. Tang, Y. Zhang, Y. Gao, and F. Gu, "Use of cement-chelated, solidified, municipal solid waste incinerator (MSWI) fly ash for pavement material: mechanical and environmental evaluations," *Canadian Geotechnical Journal*, vol. 54, no. 11, pp. 1553–1566, 2017.

[12] Q. Tang, Y. Liu, F. Gu, and T. Zhou, "Solidification/stabilization of fly ash from a municipal solid waste incineration facility using Portland cement," *Advances in Materials Science and Engineering*, vol. 2016, Article ID 7101243, 10 pages, 2016, in press.

[13] J. H. Zhang, J. H. Peng, J. L. Zheng, L. J. Dai, and Y. S. Yao, "Prediction of resilient modulus of compacted cohesive soil in south China," *International Journal of Geomechanics*, vol. 10, no. 6, pp. 248-249, 2019.

[14] P. X. Du, Y. Zhang, W. Y. Wei, and Q. Tang, "Strength and environmental characteristics of cement solidified heavy metal contaminated soil: experiment and numerical simulation," *Science, Engineering, and Technology*, vol. 18, no. 21, pp. 146–154, 2018.

[15] X. Li, C. S. Poon, and H. Sun, "Heavy metal speciation and leaching behaviors in cement based solidified/stabilized waste materials," *Journal of Hazardous Materials*, vol. 82, no. 3, pp. 215–230, 2001.

[16] S. H. Chew, A. H. M. Kamruzzaman, and F. H. Lee, "Physicochemical and engineering behavior of cement treated clays," *Journal of Geotechnical and Geoenvironmental Engineering*, vol. 130, no. 7, pp. 696–706, 2004.

[17] I. Buj, J. Torras, D. Casellas, M. Rovira, and J. de Pablo, "Effect of heavy metals and water content on the strength of magnesium phosphate cements," *Journal of Hazardous Materials*, vol. 170, no. 1, pp. 345–350, 2009.

[18] Y.-J. Du, M.-L. Wei, K. R. Reddy, F. Jin, H.-L. Wu, and Z.-B. Liu, "New phosphate-based binder for stabilization of soils contaminated with heavy metals: leaching, strength and microstructure characterization," *Journal of Environmental Management*, vol. 146, pp. 179–188, 2014.

[19] Z. He, S. W. Tang, G. S. Zhao, and E. Chen, "Comparison of three and one dimensional attacks of freeze-thaw and carbonation for concrete samples," *Construction and Building Materials*, vol. 127, pp. 596–606, 2016.

[20] M. A. Othman and C. H. Benson, "Effect of freeze-thaw on the hydraulic conductivity and morphology of compacted clay," *Canadian Geotechnical Journal*, vol. 30, no. 2, pp. 236–246, 1993.

[21] C. B. Lake, A. M. Yousif, and R. J. Jamshidi, "Examining freeze/thaw effects on performance and morphology of a lightly cemented soil," *Cold Regions Science and Technology*, vol. 134, pp. 33–44, 2016.

[22] S. Panthapulakkal and M. Sain, "The use of wheat straw fibres as reinforcements in composites," in *Biofiber Reinforcements in Composite Materials*, O. Faruk and M. Sain, Eds., pp. 423–453, Woodhead Publishing India, Ltd., Delhi, India, 2015.

[23] Y. Bi, C. Y. Gao, Y. J. Wang, and B. Y. Li, "Estimation of the amount of Chinese straw resources," *Chinese Society of Agricultural Engineering*, vol. 25, no. 12, pp. 211–217, 2009.

[24] B. A. M. Radzi, D. R. Oros, and B. R. Simoneit, "Biomass burning as the main source of organic aerosol particulate matter in Malaysia during haze episodes," *Chemosphere*, vol. 55, no. 8, pp. 1089–1095, 2004.

[25] L. Hong, G. Liu, L. Zhou, J. Li, H. Xu, and D. Wu, "Emission of organic carbon, elemental carbon and water-soluble ions from crop straw burning under flaming and smoldering conditions," *Particuology*, vol. 31, no. 2, pp. 181–190, 2017.

[26] Y. Guan, G. Chen, Z. Cheng, B. Yan, and L. a. Hou, "Air pollutant emissions from straw open burning: a case study in tianjin," *Atmospheric Environment*, vol. 171, pp. 155–164, 2017.

[27] S. Panthapulakkal, M. Sain, and M. Sain, "Preparation and characterization of wheat straw fibers for reinforcing application in injection molded thermoplastic composites," *Bioresource Technology*, vol. 97, no. 2, pp. 265–272, 2006.

[28] S. H. Ghaffar and M. Fan, "An aggregated understanding of physicochemical properties and surface functionalities of wheat straw node and internode," *Industrial Crops and Products*, vol. 95, pp. 207–215, 2017.

[29] M. Li, S. Xi Chai, H. Yuan Zhang, H. Pu Du, and L. Wei, "Feasibility of saline soil reinforced with treated wheat straw and lime," *Soils and Foundations*, vol. 52, no. 2, pp. 228–238, 2012.

[30] Y.-J. Du, M.-L. Wei, K. R. Reddy, Z.-P. Liu, and F. Jin, "Effect of acid rain pH on leaching behavior of cement stabilized lead-contaminated soil," *Journal of Hazardous Materials*, vol. 271, no. 4, pp. 131–140, 2014.

[31] J. L. Qi, J. M. Zhang, and Y. L. Zhu, "Influence of freezing–thawing on soil structure and its soils mechanics significance," *Chinese Journal of Rock Mechanics and Engineering*, vol. 22, pp. 2690–2694, 2004.

[32] B. Koohestani, T. Belem, A. Koubaa, and B. Bussière, "Experimental investigation into the compressive strength development of cemented paste backfill containing Nano-silica," *Cement and Concrete Composites*, vol. 72, pp. 180–189, 2016.

[33] P. K. Mehta and P. J. Monteiro, *Concrete Structure, Properties and Materials*, Prentice-Hall, Englewood Cliff, NJ, USA, 2nd edition, 1993.

[34] D. H. Everett, "The thermodynamics of frost damage to porous solids," *Transactions of the Faraday Society*, vol. 57, no. 5, pp. 1541–1551, 1961.

[35] D. H. Everett and J. M. Haynes, "Capillary properties of some model pore systems with special reference to frost damage," *RILEM Bulletin*, vol. 27, pp. 31–36, 1965.

[36] F. Gu, W. Ma, R. C. West, A. J. Taylor, and Y. Zhang, "Structural performance and sustainability assessment of cold central-plant and in-place recycled asphalt pavements: a case study," *Journal of Cleaner Production*, vol. 208, pp. 1513–1523, 2019.

[37] K. A. Kalliopi, "Pore structure of cement-based materials: testing, interpretation and requirements,"*Series: Modern Concrete Technology*, Vol. 12, pp. 1–33, CRC Press, Boca Raton, FL, USA, 2006.

[38] Y.-S. Wang, J.-G. Dai, L. Wang, D. C. W. Tsang, and C. S. Poon, "Influence of lead on stabilization/solidification by ordinary Portland cement and magnesium phosphate cement," *Chemosphere*, vol. 190, pp. 90–96, 2018.

[39] O. Onuaguluchi and N. Banthia, "Plant-based natural fibre reinforced cement composites: a review," *Cement and Concrete Composites*, vol. 68, pp. 96–108, 2016.

[40] S. P. Shah, "Do fibers increase the tensile strength of cement-based matrixes?," *ACI Materials Journal*, vol. 88, no. 6, pp. 595–602, 1991.

[41] A. Tagnit-Hamou, Y. Vanhove, and N. Petrov, "Microstructural analysis of the bond mechanism between polyolefin fibers and cement pastes," *Cement and Concrete Research*, vol. 35, no. 2, pp. 364–370, 2005.

[42] J. D. Frost and J. Han, "Behavior of interfaces between fiber-reinforced polymers and sands," *Journal of Geotechnical and Geoenvironmental Engineering*, vol. 125, no. 8, pp. 633–640, 1999.

[43] J. Qu and Z. Sun, "Strength behavior of shanghai clayey soil reinforced with wheat straw fibers," *Geotechnical and Geological Engineering*, vol. 34, no. 2, pp. 515–527, 2015.

[44] J. Prabhakara and R. S. Sridhar, "Effect of random inclusion of sisal fibre on strength behaviour of soil," *Construction and Building Materials*, vol. 16, no. 2, pp. 123–131, 2002.

[45] L. Wei, S. X. Chai, and H. Z. Cai, "Evaluation of anticorrosive measures for wheat straw and strengthening mechanism of reinforced saline soil in littoral area," *Geotechnical investigation Surveying*, vol. 37, no. 1, pp. 5–7, 2009.

[46] C. Tang, B. Shi, W. Gao, F. Chen, and Y. Cai, "Strength and mechanical behavior of short polypropylene fiber reinforced and cement stabilized clayey soil," *Geotextiles and Geomembranes*, vol. 25, no. 3, pp. 194–202, 2007.

[47] K. Huang, J. W. Wran, G. Chen, and Y. Zeng, "Testing study of relationship between water content and shear strength of unsaturated soils," *Rock and Soil Mechanics*, vol. 33, no. 9, pp. 2600–2604, 2012.

[48] J. Li, J. Zhang, G. Qian, J. Zheng, and Y. Zhang, "Three-dimensional simulation of aggregate and asphalt mixture using parameterized shape and size gradation," *Journal of Materials in Civil Engineering*, vol. 31, no. 3, article 04019004, 2019.

Research Article

A Fractional-Order Model of Biopolyester Containing Naturally Occurring Compounds for Soil Stabilization

Nadka Tzankova Dintcheva [ID], Marilena Baiamonte, Rosalia Teresi, Gioacchino Alotta, Emanuela Bologna, and Massimiliano Zingales

Dipartimento di Ingegneria Civile, Ambientale, Aerospaziale, dei Materiali, Università di Palermo, Viale delle Scienze, Ed. 6, 90128 Palermo, Italy

Correspondence should be addressed to Nadka Tzankova Dintcheva; nadka.dintcheva@unipa.it

Currently, the use of polymers and biopolymers as soil-stabilizer additives for control of the soil degradation, deterioration, and desertification and for improving the arid and semiarid soils has been expanded significantly in the agricultural sector. This research was conducted to determine the effect of naturally occurring compounds, such as quercetin (Q) and sodium montmorillonite (NaMMt) at different weight ratios, in biopolyester, such as polylactic acid (PLA), aiming to formulate ecosustainable materials to control the soil degradation and to protect the environment. As known, the use of sophisticated analytical tools to describe the material rheology and melting properties is nowadays very popular among physicists and material scientists. Certainly, several experimental tests conducted on polymeric- and biopolymeric-based materials, such as rubbers, foams, and hydro/aero gels, show that the relaxation time spectra are a continuous function, and as a consequence, multiple relaxation times are involved in the rheological description of the materials, yielding the need for nonconventional relaxation functions. Indeed, in this work, the considered fractional-order model could be considered a powerful tool to describe and to predict the melting properties of the complex polymer-based systems containing different additives.

1. Introduction

In the last two decades, the biodegradable polymers have widely been investigated to replace synthetic polymers because of environmental problems and decreasing fossil resources. The applications of biodegradable polymers in the agricultural field as covering films, mulching films, packaging, soil subsistence, etc., are a very promising and challenging issue [1]. However, the products formulated using polymers and biodegradable polymers must exert properties, performances, and durability compatible with the specific applications in the agricultural sector. In particular, the maintenance of the performance during their lifetime is a critical topic for successful applications. So, researchers have been focusing on a growing attention to nanocomposite formulation based on polymers and biopolymers containing reinforcement additives and natural stabilizing agents [2, 3].

Furthermore, some polymers, such as polystyrene and polyacrylamide, and biopolymers, such as biopolyester, have been identified and recognized as efficient and valuable soil conditioners because of their ability to stabilize the soil surface structure and pore continuity, preventing the soil erosion and controlling the water infiltration [2, 4, 5]. For example, as known, the arid and semiarid soils are characterized by low erratic rainfall, long periodic droughts, and high water evaporation, and in order to improve the agricultural productivity of these soils, the use of polymers and biopolymers as soil conditioners is absolutely imperative.

Polylactic acid, PLA, is a compostable thermoplastic made from renewable sources and able to degrade into innocuous lactic acid. PLA is used as medical implants and for the encapsulation of many therapeutic agents due to its high hydrophobicity, strong mechanical strength, and slow drug release. Furthermore, PLA can be used as a compostable packaging material, and the maintenance of the

performance during its service lifetime, however, remains a critical point for successful applications [6, 7].

Naturally occurring minerals, such as montmorillonite and bentonite, are very attractive polymer and biopolymer additives because of their ability to improve significantly the gas and water impermeability and to enhance the mechanical performance of the materials [8, 9]. Moreover, the montmorillonite and bentonite nanoparticles are naturally occurring minerals, and their release in the soil can be considered an absolutely eco-friendly issue.

Natural antioxidants receive attention in packaging and in the food industry also because of their presumed safety. Quercetin is an abundant flavonoid suitable in stabilizing polymer against both thermo-oxidation during processing and photo-oxidation during UV exposure. Its protective action is performed by reducing free radical formation, scavenging free radicals and, also, binding transition metal ions [10, 11]. It is of fundamental importance to investigate and to verify the usefulness of flavonoids in the thermo- and photo-oxidation stabilization and also for bio-polymer. The protection of biodegradable polymers provided by the flavonoid compound is similar to that obtained using the synthetic commercial light stabilizer [12, 13].

The use of sophisticated analytical tools to describe material rheology of neat polymer- or complex polymer-based systems is nowadays very popular among physicists and material scientists. Indeed, several experimental tests conducted on materials having different chemical nature, such as rubbers, foams, and hydro/aero gels, show that the relaxation time spectra are a continuous function, and as a consequence, multiple relaxation times are involved in the rheological description of the materials, yielding the need for nonconventional relaxation functions. Among them, the widely used stretched-exponential relations and the power-law relaxation well suited for complex system materials. In the context of linear material hereditariness, the use of power law expression of creep/relaxation to describe experimental data yields a rheological formulation in terms of the current fractional-order operators.

In this study, the authors will use the fractional-order calculus to fit the experimental data obtained for a biodegradable polylactic acid (PLA) containing naturally occurring compounds, such as quercetin (Q) and sodium montmorillonite (NaMMt) nanoparticles, at different ratios, as valuable materials for soil conditioners. The natural polyphenolic compound, i.e., Q, has been added in PLA at different concentrations, e.g., 0.5, 2, and 3 wt.%, considering the currently published experience of the authors in demonstrating the specific concentration dependent anti-/pro-oxidant activity of these molecules if introduced in PLA [14, 15]. Particularly, if these naturally occurring molecules are added at low concentrations, from 0.1 to 0.5 wt.%, they are able to protect the biopolyester against the exposure to UVB irradiation, but if they are added at high concentrations, from 2 to 3 wt.%, they are able to exert a prodegradant effect. Moreover, the naturally occurring silicate, i.e., NaMMt, and the natural phenolic compound, i.e., Q, have been considered in this work because of its beneficial effect as sustainable reinforcement additives for polymers and biopolymers, and their release in the soil is an absolutely eco-friendly issue.

2. Experimental Part

2.1. Materials. The materials used in this work are as follows:

(i) Polylactic acid (PLA) 2002D is purchased from NatureWorks LLC. Its main properties are molecular weight, $M_w = 204456$ g/mol; melting point, $T_m = 150°C–160°C$; glass transition temperature, $T_g = 58°C$; and melting index $(260°C/2.16\,kg) = 5.0–7.0$.

(ii) Natural sodium montmorillonite is purchased from Cloisite®Na+ (NaMMt) by Southern Clay; Quat. Conc. meq/100 g clay = 92.6 and $d_{001} = 1.17$ nm.

(iii) 2-(3,4-Dihydroxyphenyl)-3,5,7-trihydroxy-4H-1-benzopyran-4-one hydrate by Sigma-Aldrich; named quercetin (Q); molecular weight = 302,24 (anhydrous basis).

2.2. Processing. The preparation of PLA-based samples was carried out using a Brabender mixer at $T = 170°C$ and a mixing speed of 50 rpm for 5 minutes. NaMMt and Q have been added at different ratios as follows: 2.5/0.5, 2.5/2, and 2.5/3 (wt./wt.%). The neat PLA matrix and PLA/NaMMt have been subjected to the same processing conditions.

2.3. Characterizations. Rheological tests were performed using a strain-controlled rheometer (mod. ARES G2 from TA Instrument) in parallel-plate geometry (plate diameter of 25 mm). The complex viscosity (η^*) was measured performing time sweep experiments, at $\omega = 1$ rad/s and $T = 170°C$. The strain amplitude was $\gamma = 2\%$, which preliminary strain sweep experiments proved to be low enough to be in the linear viscoelastic regime.

The X-ray diffraction (XRD) analysis of PLA, PLA/NaMMt, and PLA/NaMMt/Q compound films was performed using an Empyrean Series 2 X-ray diffraction (Panalytical): the spectra of the sample film were recorded in the range 3–30 deg (step size = 0.025; scanning rate = 60 s/step) and Cu-Kα radiation at wavelength $\lambda = 0.1542$ nm.

The calorimetric data were evaluated by differential scanning calorimetry (DSC) using a Perkin Elmer DSC7 calorimeter. All experiments were performed under dry N_2 on samples of around 10 mg in 40 μl sealed aluminium pans. Four calorimetric (two heating: 30°C–220°C and two cooling: 220°C–30°C) scans were performed for each sample at the scanning heating/cooling rate of 5°C/min.

The crystallinity degree (X_c) is calculated using the following formula: X_c (%) = ($\Delta H_m + \Delta H_{cc}/\Delta H°$) × 100, where ΔH_m is the heat of melting of the sample, ΔH_{cc} corresponds to the heat of cold crystallization, and $\Delta H°$ is the heat of fusion for 100% crystalline PLA (93 J/g) [16].

Tensile properties were determined at room temperature and humidity, using an Instron (U.S.A.) dynamometer mod. 3365, according to ASTM test method D882. The specimens

were cut out from films in the machine direction and tested. The modulus was measured at the speed of 1 mm/min. When the deformation was about 10%, the speed was increased up to 100 mm/min until break. The data reported are the average values (with the related error bars) obtained through ten tests per sample.

2.4. Fractional Calculations. Fractional calculus may be considered the extension of the ordinary differential calculus to noninteger powers of derivation orders [17, 18]. In this section, we address some basic notions about this mathematical tool.

The Euler Gamma function $\Gamma(z)$ may be considered as the generalization of the factorial function since z assumes integer values as $\Gamma(z + 1) = z!$, and it is defined as the result of the integral as follows:

$$\Gamma(z) = \int_0^\infty e^{-x} x^{z-1} dx. \tag{1}$$

The Riemann–Liouville fractional integrals and derivatives with $0 < \beta < 1$ of functions defined over intervals of the real axis, namely, $f(t)$ such that $t \in [a, b] \subset R$, have the following forms:

$$\left(\mathbf{I}_a^\beta f\right)(t) = \frac{1}{\Gamma(\beta)} \int_a^t \frac{f(\tau)}{(t - \tau)^{1-\beta}} d\tau,$$

$$\left(\mathbf{D}_a^\beta f\right)(t) = \frac{f(a)}{\Gamma(1 - \beta)(t - a)^\beta} + \frac{1}{\Gamma(1 - \beta)} \int_a^t \frac{f'}{(t - \tau)^\beta} dr. \tag{2}$$

Besides the Riemann–Liouville fractional operators defined above, another class of fractional derivative that is often used in the context of fractional viscoelasticity is represented by Caputo fractional derivatives which are defined as

$$\left(_C\mathbf{D}_a^\beta f\right)(t) := \mathbf{I}_a^{m-\beta}\left(\mathbf{D}_a^m f\right)(t), \quad m - 1 < \beta < m, \tag{3}$$

and whenever $0 < \beta < 1$, it reads as follows:

$$\left(_C\mathbf{D}_a^\beta f\right)(t) = \frac{1}{\Gamma(1 - \beta)} \int_a^t \frac{f'(\tau)}{(t - \tau)^\beta} dr. \tag{4}$$

A closer analysis of equations (3) and (4) shows that the Caputo fractional derivative coincides with the integral part of the Riemann–Liouville fractional derivative in the bounded domain. Moreover, the definition in equation (4) implies that the function $f(t)$ has to be absolutely integrable of order m (e.g., in (4), the order is $m = 1$). Whenever $f(a) = 0$, Caputo and Riemann–Liouville fractional derivatives coalesce.

Similar considerations hold true also for Caputo and Riemann–Liouville fractional derivatives defined on the entire real axis. Caputo fractional derivatives may be considered as the interpolation among the well-known, integer-order derivatives, operating over functions $f(\circ)$ that belong to the class of the Lebesgue integrable functions $(f(\circ) \in L^1)$ as a consequence, and they are very useful in the mathematical description of complex system evolution.

3. Results and Discussion

It is shown that power law relaxation, in the functional class of

$$G(t) = \sum_{j=1}^N c_{\beta_j} t^{-\beta_j}, \tag{5}$$

yields an accurate representation of the experimental data for several kinds of mixtures analysed. Introducing the Boltzmann superposition principle for time-varying deformation law $\varepsilon(t)$, the rheological model yields:

$$\sigma(t) = \sum_{j=1}^N c_{\beta_j}\left(_C\mathbf{D}_0^{\beta_j}\varepsilon\right)(t). \tag{6}$$

For the considered semicrystalline polymer, the maximum number $N = 2$ yields the inverse relation of equation (6) as

$$\varepsilon(t) = \int_0^t E_{\alpha,\beta}(t - \tau)\sigma(\tau) dr, \tag{7}$$

where $E_{\alpha,\beta}(t)$ is the two parameters Mittag-Leffler function defined as

$$E_{\alpha,\beta}(t) = \sum_{k=0}^\infty \frac{t^k}{\Gamma(\alpha k + \beta)}, \tag{8}$$

where the parameters β_i and $c_{\beta i}$ have been estimated via the least-squared method for different concentrations of natural-based silicates as sodium montmorillonite (NaMMt).

However, the rheological analysis on PLA-based samples containing NaMMt and Q at different ratios has been carried out, and the fitting between the experimental data obtained and theoretical calculated data has been established.

The complex viscosity of the material, obtained by experimental data, is defined as

$$\eta(\omega) = \left[G'(\omega)^2 + G''(\omega)^2\right]^{1/2}, \tag{9}$$

where the complex storage $G''(\omega)$ and loss $G'(\omega)$ moduli are defined as the real and imaginary parts of the Fourier transform of eq. (5) as

$$G'(\omega) = \sum_{j=1}^N \frac{c_{\beta_j} \omega^{\beta_j+1} \sin(\beta_j \pi/2)}{\Gamma(1 - \beta_j)},$$

$$G''(\omega) = \sum_{j=1}^N \frac{c_{\beta_j} \omega^{\beta_j+1} \cos(\beta_j \pi/2)}{\Gamma(1 - \beta_j)}. \tag{10}$$

In Figure 1, the trends of the complex viscosity for neat PLA and PLA/NaMMt containing different amounts of Q as a function of time have been plotted. It can be observed that the adding of 2.5 wt.% NaMMt in PLA leads to a slight increase in the complex viscosity values at the early stage of the rheological analysis, while, at long experimental times, the adding of NaMMt nanoparticles leads to a slight decrease in the complex viscosity values probably because
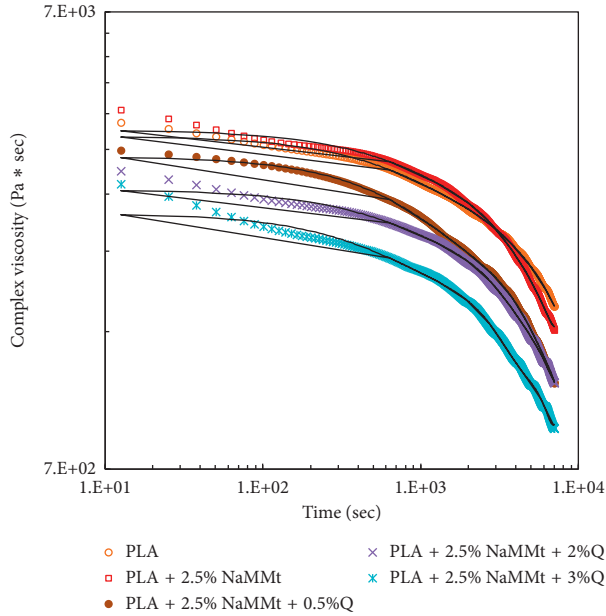
FIGURE 1: Complex viscosity data (symbols) and theoretical fittings (continuous lines) of neat PLA and PLA/NaMMt containing different amounts of Q.

TABLE 1: Fitting parameters for the power laws expansion in equaiton (10).

Sample	N	β	C_β
PLA	1	0.1985	7373,54
PLA + 2.5% NaMMt	1	0.1762	6545,61
PLA + 2.5% NaMMt + 0.5%Q	1	0.2229	6666,19
PLA + 2.5% NaMMt + 2%Q	1	0.1852	5164,57
PLA + 2.5% NaMMt + 3%Q	1	0.2052	4710,70

FIGURE 2: XRD spectra of neat PLA and PLA/NaMMt containing different amounts of Q.

of these flexible nanoplatelets that are able to align themselves along the flow direction, as proposed in literature [19]. Besides, the addition of naturally occurring molecules, as quercetin, in PLA/NaMMt nanocomposite leads to decrease in the complex viscosity values. This last issue could be understood considering that these low molecular weight molecules if added at high concentrations are able to exert pronounced plasticizing action, which leads to a significant decrease in the complex viscosity values.

The fitting parameters obtained for $N = 1$ expansion in equation (10) is reported in Table 1.

It is interesting to highlight that the fitting of the experimental data, based on the Caputo fractional derivative model for semicrystalline polymers, and the experimentally obtained results are very good, especially at long experimental times. The slight deviation between experimental data obtained and theoretical trends at early stage of the experiment could be understood by taking into account two different issues: (i) the description of the behaviour for complex polymer-based systems is very hard matter because of some morphological evolution of these systems and (ii) the interactions between the constituents, e.g., NaMMt and Q, can change because of alignment and/or orientation of the nanofillers can occur during the experiment.

Moreover, the morphology of the investigated systems has been evaluated through XRD and DSC analysis. The neat PLA and PLA/NaMMt samples containing different amounts of Q show similar XRD spectra (Figure 2). The main diffraction peak at around 15° slightly decreases due to the presence of Q molecules highlighting a reduction of the polymer crystalline structure. The diffraction peak at around

6° can be attributed to intrinsic PLA crystalline structure and to the presence of NaMMt nanoparticles; due to the signal overlapping, the estimation of nanofiller morphology in the PLA almost amorphous samples is a very hard matter.

The obtained results of the DSC analysis are shown in Table 2. In particular, the glass transition (T_g) and melting (T_m) temperatures, fusion (ΔH_m) and cold crystallization (ΔH_{cc}) enthalpies, and calculated crystallinity degree (X_c) of the samples are reported. As expected, the crystallinity degree of PLA slightly increases due to the addition of NaMMt nanoparticles and decreases due to the presence of the large amount of Q molecules.

Finally, to evaluate the possibility to use the PLA-based materials for soil stabilization, the mechanical tensile properties, i.e., elastic modulus (E), tensile strength (TS), and elongation at break (EB), of all instigated samples have been carried out and the obtained results are reported in Table 3. It can be observed that the addition of the NaMMt nanoparticles leads to the increase of the system rigidity and, in particular, the E and TS increase due to the presence of nanofillers, and this reinforcing effect has not been penalized by the presence of Q molecules in the solid state. The last issue highlights the possibility to consider these materials as

TABLE 2: Thermal properties of neat PLA and PLA/NaMMt containing different amounts of Q evaluated during second heating scan.

Sample	T_g (°C)	T_m (°C)	ΔH_m (J/g)	ΔH_{cc} (J/g)	X_c (%)
PLA	58.3	150.2	17.4	8.1	10
PLA + 2.5% NaMMt	58.7	146.8	21.8	5.8	17.5
PLA + 2.5% NaMMt + 0.5%Q	58.0	147.2	19.2	5.5	14.3
PLA + 2.5% NaMMt + 2%Q	57.0	151.0	24.5	14.4	5.6
PLA + 2.5% NaMMt + 3%Q	57.3	147.3	15.0	8.8	4.5

TABLE 3: Main mechanical properties: elastic modulus (E), tensile strength (TS), and elongation at break (EB), of neat PLA and PLA/NaMMt containing different amounts of Q.

Sample	E (MPa)	TS (MPa)	EB (%)
PLA	1555 ± 50	47.0 ± 2.5	9.1 ± 1.5
PLA + 2.5% NaMMt	1845 ± 58	51.2 ± 3.5	9.5 ± 2.0
PLA + 2.5% NaMMt + 0.5%Q	1848 ± 55	43.8 ± 2.1	15.0 ± 2.5
PLA + 2.5% NaMMt + 2%Q	1832 ± 51	42.8 ± 2.2	14.1 ± 2.5
PLA + 2.5% NaMMt + 3%Q	1808 ± 52	40.8 ± 2.5	13.0 ± 2.5

good candidates for soil stabilizations, considering also their naturally occurring nature.

4. Conclusions

In this work, the effect of naturally occurring compounds, such as NaMMt and Q, in PLA has been investigated through experimental and theoretical analysis, considering these materials as suitable candidates for soil stabilization in the agricultural sector. In particular, the rheological behaviour of the investigated systems has been estimated through the evaluation of the complex viscosity trends as a function of time. Besides, the fitting between experimental data obtained and theoretical calculated data has been accurately investigated and analysed. It can be concluded that the theoretical model is able to predict exactly the rheological behaviour of the investigated complex biopolymer-based systems at long experimental time, while, at short experimental time, the interactions between the system components are pronounced, and for these reasons, some deviations have been observed.

To evaluate the system morphology and solid-state properties of all investigated samples, accurate XRD and DSC analyses and mechanical tensile tests have been carried out.

Finally, all obtained results suggest the possibility to consider these materials as suitable candidates for soil stabilization.

Data Availability

The data used to support the findings of this study are available from the corresponding author upon request.

Conflicts of Interest

The authors declare that they have no conflicts of interest.

References

[1] R. D. Lentz and R. E. Sojka, "Field results using polyacrylamide to manage furrow erosion and infiltration," *Soil Science*, vol. 158, no. 4, pp. 274–282, 1994.

[2] V. S. Green, D. E. Stott, J. G. Graveel, and L. D. Norton, "Stability analysis of soil aggregates treated with anionic polyacrylamides of different molecular formulations," *Soil Science*, vol. 169, no. 8, pp. 573–581, 2004.

[3] A. Maghchiche, A. Haouam, and B. Immirzi, "Use of polymers and biopolymers for water retaining and soil stabilization in arid and semiarid regions," *Journal of Taibah University for Science*, vol. 4, no. 1, pp. 9–16, 2018.

[4] V. S. Green, D. E. Stott, L. D. Norton, and J. G. Graveel, "Polyacrylamide molecular weight and charge effects on infiltration under simulated rainfall," *Soil Science Society of America Journal*, vol. 64, no. 5, pp. 1786–1791, 2000.

[5] A. Husein and J. T. Thomas, "Polyacrylamide and Water Quality Effects on Infiltration in Sandy Loam Soils," *Soil Science Society of America Journal*, vol. 70, pp. 643–650, 2006.

[6] R. M. Rasal, A. V. Janorkar, and D. E. Hirt, "Poly(lactic acid) modifications," *Progress in Polymer Science*, vol. 35, no. 3, pp. 338–356, 2010.

[7] M. P. Arrieta, M. D. Samper, J. López, and A. Jiménez, "Combined effect of poly(hydroxybutyrate) and plasticizers on polylactic acid properties for film intended for food packaging," *Journal of Polymers and the Environment*, vol. 22, no. 4, pp. 460–470, 2014.

[8] W. Gianelli, G. Camino, N. T. Dintcheva, S. L. Verso, and F. P. L. Mantia, "EVA-montmorillonite nanocomposites: effect of processing conditions," *Macromolecular Materials and Engineering*, vol. 289, no. 3, pp. 238–244, 2004.

[9] F. P. La Mantia and N. Tzankova Dintcheva, "Eva copolymer-based nanocomposites: rheological behavior under shear and isothermal and non-isothermal elongational flow," *Polymer Testing*, vol. 25, no. 5, pp. 701–708, 2006.

[10] G. Cao, E. Sofic, and R. L. Prior, "Antioxidant and prooxidant behavior of flavonoids: structure-activity relationships," *Free Radical Biology and Medicine*, vol. 22, no. 5, pp. 749–760, 1997.

[11] M. D. Samper, E. Fages, O. Fenollar, T. Boronat, and R. Balart, "The potential of flavonoids as natural antioxidants and UV light stabilizers for polypropylene," *Journal of Applied Polymer Science*, vol. 129, no. 4, pp. 1707–1716, 2012.

[12] N. T. Dintcheva and F. P. La Mantia, "Durability of a starch-based biodegradable polymer," *Polymer Degradation and Stability*, vol. 92, no. 4, pp. 630–634, 2007.

[13] N. Tz. Dintcheva, F. P. La Mantia, and R. Arrigo, "Natural compounds as light stabilizer for a starch-based biodegradable polymer," *Journal of Polymer Engineering*, vol. 34, no. 5, pp. 441–449, 2014.

[14] N. T. Dintcheva, R. Arrigo, M. Baiamonte, P. Rizzarelli, and G. Curcuruto, "Concentration-dependent anti-/pro-oxidant activity of natural phenolic compounds in bio-polyesters," *Polymer Degradation and Stability*, vol. 142, pp. 21–28, 2017.

[15] N. T. Dintcheva, M. Baiamonte, and M. Spera, "Assessment of pro-oxidant activity of natural phenolic compounds in bio-polyesters," *Polymer Degradation and Stability*, vol. 152, pp. 280–288, 2018.

[16] H. Wang, X. Sun, and P. Seib, "Strengthening blends of poly(lactic acid) and starch with methylenediphenyl diisocyanate," *Journal of Applied Polymer Science*, vol. 82, no. 7, pp. 1761–1767, 2001.

[17] S. Samko, A. Kilbas, and O. Marichev, *Fractional Integrals and Derivatives: Theory and Applications*, Taylor & Francis, England, UK, 1987.

[18] I. Podlubny, *Fractional Differential Equations*, Accademic Press, Cambridge, MA, USA, 1999.

[19] G. Filippone, S. C. Carroccio, G. Curcuruto, E. Passaglia, C. Gambarotti, and N. T. Dintcheva, "Time-resolved rheology as a tool to monitor the progress of polymer degradation in the melt state-Part II: Thermal and thermo-oxidative degradation of polyamide 11/organo-clay nanocomposites," *Polymer*, vol. 73, pp. 102–110, 2015.

Research Article

Spectral Variation and Corresponding Changing Mechanism of Suspended Particulate Material Absorption in Poyang Lake during Flood Periods

Yuandong Wang (ID),[1,2] **Xibin You,**[1] **Lianfang Yu,**[1] **Lihong Meng,**[1] **Xiangming Xu,**[1] **and Guangxu Liu**[1]

[1]*College of Geography and Planning, Gannan Normal University, Ganzhou 341000, China*
[2]*Key Laboratory of Digital Earth Science, Institute of Remote Sensing and Digital Earth, Chinese Academy of Sciences, Beijing 100094, China*

Correspondence should be addressed to Yuandong Wang; ydwang@yic.ac.cn

Remote sensing accuracy of the dynamic water environment under a changing environment due to climate and anthropogenic impacts should be improved by a deep understanding of the absorption properties pertinent to the water body. Spectral variation of suspended particulate material (SPM) absorption and its changing mechanism during flood periods of Poyang Lake were analyzed in this study. Absorption coefficients were measured and determined by spectrophotometry using the quantitative filter techniques (QFTs) based on field samples from July 12 to September 06, 2017. Two main optical active constituents (OACs) of SPM including nonalgal and phytoplankton algal particulates were quantified and analyzed in detail. The results suggested that, during study periods, Poyang Lake exhibits an overall high level of suspended nonalgal detritus and algal concentration and lower water clarity, showing a strong absorption by total suspended sediments that are closely related with the land-derived nonalgal detritus material which varied significantly with diverse proportions of minerals and organic materials from multiple sources. Due to variations in phytoplankton community pigment composition, concentration, and package effect, there exists a difference between optical absorption capacity on blue (440) and red (675) portions of bands, the former of which had an obvious enhancement due to the increased effect of accessory pigments in suspended phytoplankton particles from July to September. Evidence also presented that the nonlinear dependency of specific phytoplankton particulate absorption on pigment concentration for various trophic statuses in different periods could be unstable due to relative contributions of the package effect and accessory pigments; this could bring uncertainties to the parameterization of optical models and remote sensing algorithms proposed for accurate applications in lake water environment monitoring.

1. Introduction

Absorption coefficients of optical active constituents (OACs, i.e., particulate and dissolved materials) play an important role in the inherent optical properties (IOPs, i.e., absorption and specific coefficients), largely determining the apparent optical properties (AOPs, i.e., water leaving radiance and remote sensing reflectance) in natural waters [1, 2]. Therefore, remote sensing inversion accuracy of the dynamic water environment under a changing environment due to climate and anthropogenic disturbances should be improved

by a deep understanding of the absorption properties pertinent to the water body under consideration [3–5].

Over past decades, variability in absorption coefficients has been thoroughly documented in oceanic waters (the so-called "Case 1"), where phytoplankton and their derivative products (organic detritus and dissolved yellow substance, arising by zooplankton grazing, or natural decay of the algal cells) are optically dominant, and other components are often assumed to covary with phytoplankton pigments [6–10]. Due to the simple configuration of Case 1 waters, single OAC models and algorithms based solely upon

phytoplankton have performed satisfactorily in oceanic waters [9, 11–13].

However, absorption coefficients can show significant variability in space and time in inland waters, where non-algal particles consist of minerals and nonliving organics detritus such as feccal material or degrading phytoplankton cells are not proportional to phytoplankton. Therefore, models and algorithms based solely upon chlorophyll-bearing biota are often invalid when applied to inland waters that spread across different geographic regions [14–16].

In recent years, there has been an increasing focus on the environment responses of inland waters due to climate and anthropogenic impacts, wherein spectral properties are very often dominated by land-derived inorganic or organic suspended particulate materials (SPMs) [17–22]. As the largest fresh water lake in China, Poyang Lake is in a very dynamic hydrological environment with the complex benthic topography, and its water level is further fluctuated due to frequent occurrence of extreme climate events such as heavy precipitation and storms during flood periods [25]; besides, anthropogenic activities also impact the lake environment [17]. According to previous research, water clarity of most of the lake region is between 0 and 2 m and sediment material concentration could vary between 2.6 and 220.19 mg/L throughout the year [18]. The water quality, quantity, and aquatic conditions of Poyang Lake have great impact on downstream, middle, and lower Yangtze River and the East China seashore [17].

Many researchers have performed studies in this region, and they provided valuable evidence of the optical properties of suspended substances [23–25]. Chen et al. revealed that the partition of organic and inorganic materials is helpful to accurately determine the optical property of SPM [22]. Wu et al. confirmed the temporal and regional variability of specific inherent optical properties due to different water constituents [24], and the development of the regional SPM model is fundamental for managing and protecting aquatic ecosystems [25].

Therefore, the complex spectral behavior of suspended sediments due to various OAC composition dynamics under evolving hydrological conditions in a changing climate still needs further investigation. Understanding more of variability in IOPs and the processes acting to change the optical behavior of suspended materials can be helpful to improve the accuracy of water quality parameters retrieval using remote sensing techniques for this complex water environment. To establish regional satellite algorithms aimed at evaluation of the content of suspended materials across different time spans for this dynamic lake, it is necessary to quantify the dependence of absorption coefficients on their OAC concentration at feature wavelengths, exploring corresponding contribution effects on the spectral change.

The main objectives of this study are (1) to separate absorption coefficients of suspended particulate materials in Poyang Lake through controlled laboratory experiments during the flood period, which may have its own characteristics at this time, contributing to a better understanding of the optical behavior of SPM absorption, and (2) to clarify the changing mechanism for corresponding components of absorption, which may facilitate improvements in the parameterization of remote sensing algorithms for the interpretation of remote sensing information.

2. Materials and Methods

2.1. Study Area. Poyang Lake (115°47′–116°45′E, 28°22′–29°45′N) is situated at the lower Yangtze River basin (Figure 1), with a subtropical monsoon climate and a mean annual precipitation of 1680 mm [26]. It is fed by tributaries of five rivers of Ganjiang, Fuhe, Xinjiang, Raohe, and Xiushui, connecting to and exchanging water with Yangtze River through the lake mouth in the north. The water level is highly dynamic with significant fluctuations throughout the year, with an extending water surface area (maximum to 4000 km^2) during the flood period between April and September and then shrinking during the dry period between October and March [27]. Meanwhile, the impact of anthropogenic activities on the lake water environment such as major hydrologic engineering and sand mining have caught attentions and been reported [28, 29]. Therefore, the lake water environment is under both natural and anthropogenic influences, providing a wide range of IOPs and OACs.

2.2. Sampling Details. The present work was carried out on boats, and a total of 55 water samples were collected in Lake Poyang from July 12 to 19 and September 01 to 06 in 2017, which is the representative time of flood periods when water level is at a status of increasingly high. Considering the lake geometry shape and hydrological flow directions, sample points were at about 5 km intervals and sampling locations were kept as same as possible between two survey periods; 15 samples were excluded in statistical analysis due to large distance discrepancies and outliers beyond 2 standard deviations of the mean. At each location, water samples prepared for the particulate absorption measurement were collected from the surface to about 20 cm below in the vertical direction, which were then stored in ice bags and transported to the laboratory for determinations in time. Water transparency was also recorded with the Secchi disk (SD), and geographical locations of sample sites were positioned and navigated using handheld GPS (Figure 1).

2.3. Laboratory Measurements. In the laboratory, the extraction and measurement of the chlorophyll a concentration (referred to as Chl.a) were made with acetone following the SM 10200 H spectrophotometric method [15]. Total suspended particulate material (SPM) concentrations were measured gravimetrically on preweighed Whatman GF/F filters after rinsing with distilled water.

Light absorption measurements were performed using the standard procedure of the quantitative filter technique (QFT) after the suspended particles concentrated onto Whatman GF/F filters [7]. Optical density of particulate matter was measured between 350 and 800 nm at 1 nm
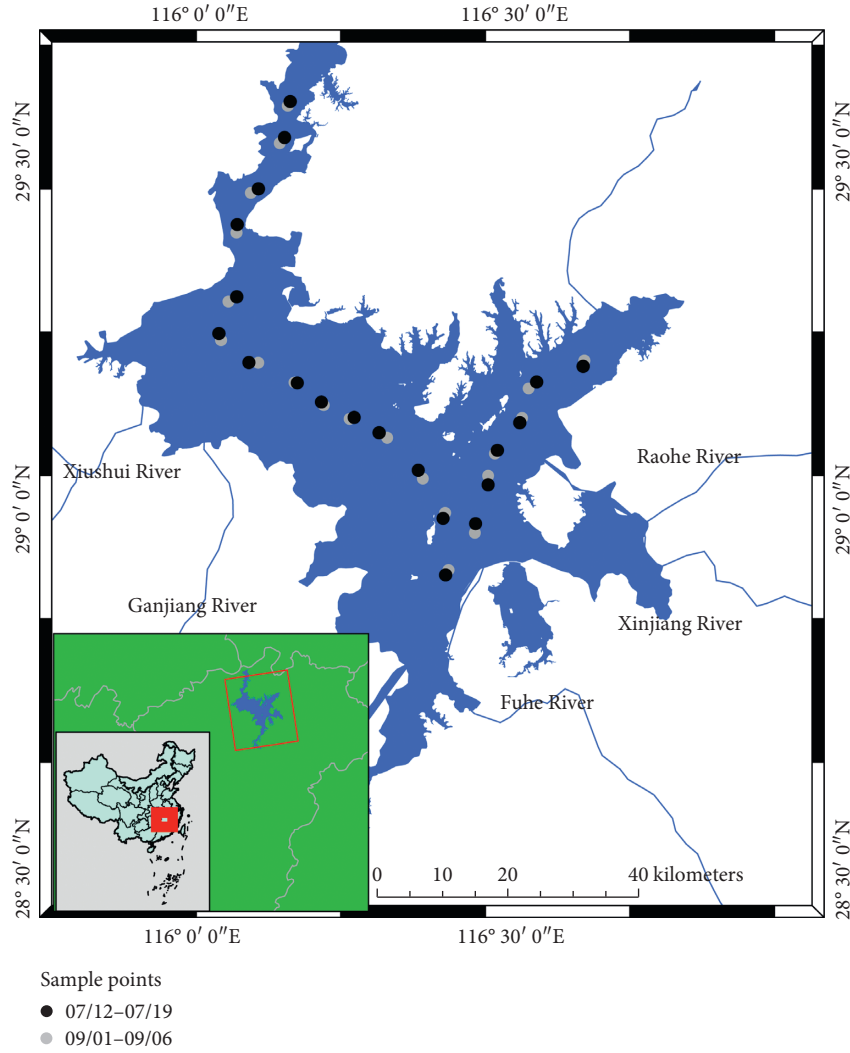
Figure 1: Location of Poyang Lake in China and sample sites over the lake during study periods.

intervals with a dual-beam scanning spectrophotometer with a blank filter saturated with distilled water as a reference. Nonalgal particle values were then determined after pigment extraction with pure methanol [7]. Statistical analysis was performed after measurements, descriptive statistics, one-way ANOVA, and correlation analysis were performed for Chl.a, SPM, and SD (Section 3), with null hypothesis stating the means of all levels are equal and alternative hypothesis stating the means of one or more levels are different at two periods. The correlation coefficient (R^2) is used to describe the strength of correlation using the guide that Evans (1996) suggested: 0.00–0.19 (very weak), 0.20–0.39 (weak), 0.40–0.59 (moderate), 0.60–0.79 (strong), and 0.80–1.0 (very strong) [30].

2.4. Analysis Methods. The absorption spectra of SPM (a_p) are decomposed into nonalgal (a_{NAP}) and phytoplankton (a_{ph}) algal components. a_p and a_{NAP} were calculated by converting total and extracted optical densities, respectively (Equation (1)). The absorption spectra for phytoplankton

(a_{ph}) were computed as the difference between a_p and a_{NAP} (Equation (2)):

$$a_p(\lambda) = \frac{2.303 \left[OD_s(\lambda) - OD_{(null)} \right]}{\beta(V_f)/A_f}, \tag{1}$$

$$a_{ph}(\lambda) = a_p(\lambda) - a_{NAP}(\lambda), \tag{2}$$

where $OD_s(\lambda)$ is the sample absorbance, and the geometric absorption path length of the suspended material was calculated as V_f/A_f, where V_f is the volume filtered (200 ml) and A_f is the clearance area of the filter. The path-length amplification factor beta was assumed to be a constant value of 2 after the theoretical calculations of Roesler (1998), and null point correction ($OD_{(null)}$) was performed by normalizing spectra to the average absorption measured between 740 and 750 nm assuming no wavelength dependence [31, 32].

The absorption spectrum of nonalgal particles for each sample was modeled from 380 to 600 nm with an exponential function using the least-squares method, and the absorption slope (S) of 40 samples was derived [33, 34]:

TABLE 1: Range of concentrations of the main OACs during two periods in 2017.

Time	Points	Range	SPM (mg/l)	Chl.a (μg/l)	SD (cm)
July	20	Mean	45.94	21.48	26
		Min	24.48	9.17	18
		Max	56.70	34.77	32
September	20	Mean	19.67	13.80	41
		Min	7.53	3.73	32
		Max	40.3	21.73	56
One-way ANOVA		F value	89.22	15.48	78.63
		Probability > F	$4.93E-10$	$3.91E-4$	$3.16E-10$

Null hypothesis: the means of all levels are equal. Alternative hypothesis: the means of one or more levels are different.

$$a_{\text{NAP}}(\lambda) = a_{\text{NAP}}(440)e^{(-S(\lambda-440))}, \qquad (3)$$

where S is the spectral slope, which can reveal relative proportions of minerals and organic materials for detritus in lake waters, because S values generally increase when mineral content decreases [34].

The absorption capacity of the phytoplankton algal component $a_{\text{ph}}(\lambda)$ per mass unit of algae can be expressed as follows [33, 34]:

$$a^*_{\text{ph}}(\lambda) = \frac{a_{\text{ph}}(\lambda)}{\text{Chl.a} \cdot \text{m}^2/\text{mg}}. \qquad (4)$$

As $a^*_{\text{ph}}(\lambda)$ usually changes due to package effects and pigment composition variations, the relationship between $a^*_{\text{ph}}(\lambda)$ and Chl.a can be expressed as a power function [33, 34]:

$$a^*_{\text{ph}}(\lambda) = A(\lambda) = [\text{Chl.a}]^{-B(\lambda)}, \qquad (5)$$

where A and B are the wavelength-dependent, positive parameters, with the exponent B representing the strength of variations of $a^*_{\text{ph}}(\lambda)$.

3. Results and Discussion

The range, average level of the SPM and Chl.a, and results of one-way ANOVA are shown in Table 1. It could be seen that, at the 0.05 level, the population means of SPM and Chl. a were both significantly different between two periods.

SPM and Chl.a were higher in July than September, representing a decreasing level of suspended sediments in lake columns as water flooded during the study time. Correspondingly, lower water transparency (SD) was observed in July, indicating higher water absorption, which is in accordance with previous research [17, 23, 24].

Although the SPM is with a low composition of phytoplankton biomass (indicated by low Chl.a compared to SPM), SD exhibited some positive correlation with Chl. a ($R^2 = 0.56$, $p < 0.01$), compared to suspended sediments ($R^2 = 0.73$, $p < 0.01$) in July, suggesting that the increasing abundance of various phytoplankton species such as spirogyra, diatoms, and cyanobacteria may also be responsible for lower transparency.

Meanwhile, more evident positive correlation of SD with SPM ($R^2 = 0.69$, $p < 0.01$) than Chl.a ($R^2 = 0.39$, $p < 0.01$) was also found in September, indicating that the vast shallow lake is usually dominated by suspended sediments (with a maximum value of 40.3 mg/l in this work) during this period [17, 24]. And water clarity was still not very high (average SD of 41 cm), which might be induced by resuspended sediments due to vertical convection disturbance of the water layer because of seasonal water-level fluctuations and relevant anthropogenic disturbances [17].

3.1. Variation of Total Suspended Particulate Material Absorption. Absorption spectra of SPM (a_p) of Poyang Lake can be decomposed into nonalgal (a_{NAP}) and phytoplankton (a_{ph}) algal components, which had been illustrated in previous research [22, 24]. Spectra curves of total suspended particulate material absorption during the flood period are present in Figure 2 (solid bold line represents mean and dashed line represents standard deviation), suggesting that absorption coefficients of SPM ($a_p(\lambda)$) were highly variable among sample points in both July and September, due to various SPM concentrations and compositions at different sample sites.

In July, the spectral shape of SPM resembled that of nonalgal particulates, with high absorption between 400 and 450 nm, ranging from 9.73 to 17.05 m^{-1} at 440 nm, indicating strong detrital particles dominance. Apparent phytoplankton absorption peaks could only be found at 675 nm, with much lower values between 1.93 and 5.83 m^{-1} and an average of 4.60 m^{-1} (Figure 2).

In September, magnitude of the whole spectrum (380–700 nm) decreased significantly, and the absorption feature of phytoplankton with accessory pigments appeared slightly at the short 400–450 nm wavelength region around 440 nm, with values between 2.47 and 4.69 m^{-1}. Meanwhile more evident peaks of phytoplankton absorption could be observed between 670 and 690 nm, but still with lower values 0.66–1.64 m^{-1} at 675 nm compared to shortwave bands (Figure 2). The growing peaks of phytoplankton absorption were also identified by Wu (2013) from August to October in their study of 2010 and 2011 [23].

To explore possible reasons accounted for SPM absorption variation, we select $a_p(440)$ and $a_p(675)$ as two feature bands to represent the blue portion (400–450 nm) and the red portion of the visible spectrum (670–690 nm), respectively. Regression analysis was performed between
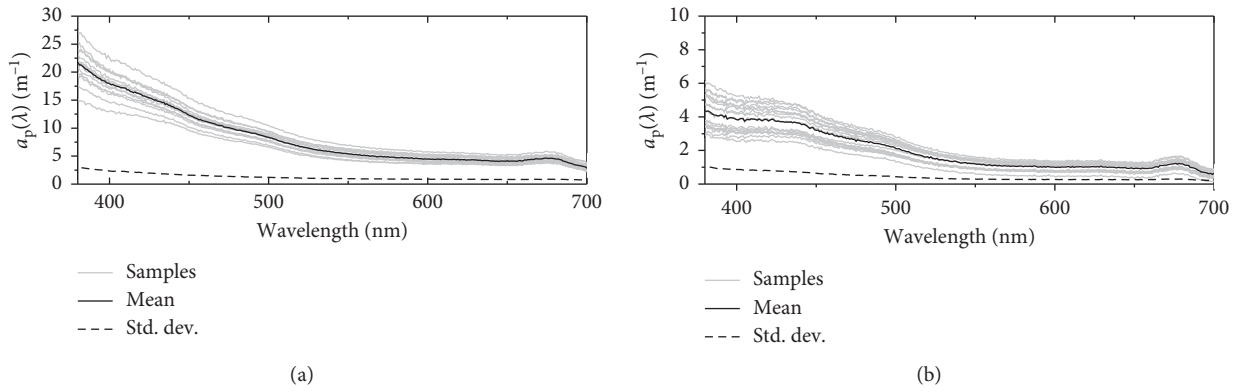
Figure 2: Total suspended particulate absorption spectra in Poyang Lake in July (a) and September (b).
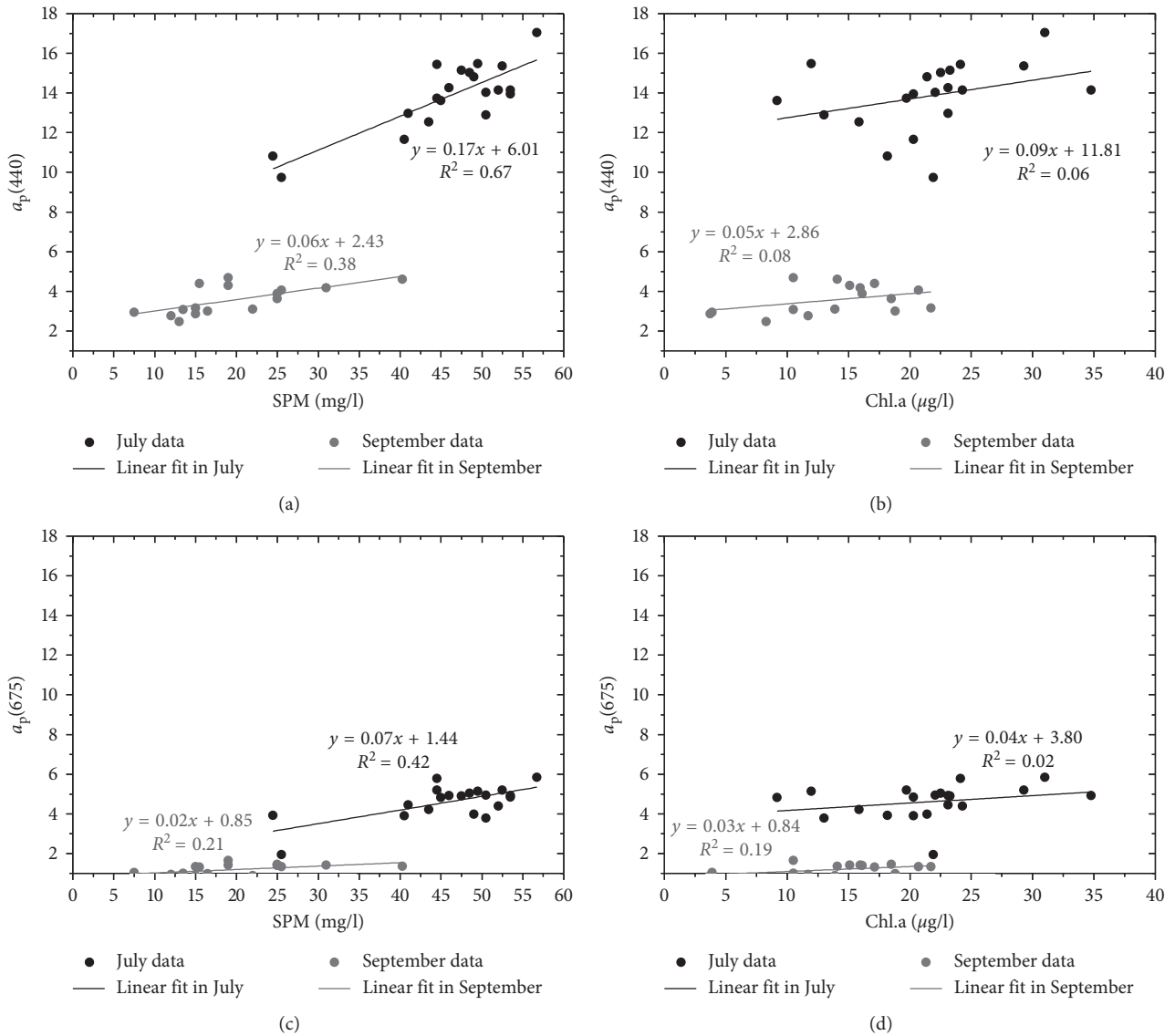

Figure 3: The linear relationships of $a_p(440)$ and $a_p(675)$ with SPM and Chl.a concentrations.

$a_p(440)$ and SPM and Chl.a, and $a_p(675)$ and SPM and Chl. a for each period (Figure 3).

It could be seen that the variation of $a_p(440)$ was more sensitive to SPM than to Chl.a for both July and September (Figures 3(a) vs 3(b)). The contribution of SPM to $a_p(440)$ tended to decrease from July to September (Figure 3(a)) as the effect of Chl.a remained at a slightly low level (Figure 3(b)). Thus, SPM absorption in blue portion of the visible spectrum was mainly dominated by nonalgal materials in lake water columns.

And the variation of $a_p(675)$ was also more sensitive to SPM than to Chl.a in July and September (Figures 3(c) vs 3(d)). The tendency of SPM contribution to $a_p(675)$ also decreased from July to September (Figure 3(c)). Although there was a slight increase of Chl.a effect in September, it was still small due to the low proportion of Chl.a in SPM composition.

Although the sediments' masking effect decreased in September, nonalgal particles still dominated the absorption at wavelengths around 400–450 nm, and contributions of phytoplankton at 600–690 nm were still weaker than those of nonalgal sediments. Thus, total suspended particulate material absorption during the flood period was mainly associated with detritus materials in both the blue and red spectra, which is in accordance with the results of previous research in Poyang Lake, Taihu Lake, and Chagan Lake, showing that the total SPM absorption is mainly dominated by nonalgal materials [23, 24, 35, 36].

Therefore, it is reasonable to be deduced that SPM absorption of Poyang Lake mainly has strong connection with nonalgal detritus, which will be elaborated in the next section.

3.2. Variation of Nonalgal Particulate Material Absorption.

In this study, the absorption spectrum of nonalgal particles for each sample was modeled from 380 to 600 nm according to Equation (3) using the least-squares method, and the absorption slope (S) of 40 samples was derived, from which the relative proportions of minerals and organic materials in detritus could be revealed [32].

The results showed that, in July, S varied within 0.0060–0.0107 nm^{-1} around 0.0069 nm^{-1}, and in September, its magnitude dropped to 0.0049–0.0102 nm^{-1} with an average level of 0.0067 nm^{-1}. The variation of the detritus absorption slope could be clearly seen from absorption spectra normalized to 440 nm in Figure 4. It suggests that S values generally decreased from July to September, indicating an elevated proportion of inorganic materials in SPM composition.

Regression analysis was also conducted between $a_{NAP}(440)$ and SPM and Chl.a, and $a_{NAP}(675)$ and SPM and Chl.a for each period to reveal factors responsible for variation of nonalgal material absorption in the blue region (400–450) and red region of spectra, respectively (Figure 5).

It is shown that $a_{NAP}(440)$ had a much stronger relationship with SPM than with Chl.a in both July and September (Figures 5(a) vs 5(b)). From July to September, although there was slightly a decrease in SPM

contribution (Figure 5(a)), the effect of Chl.a was still very low (Figure 5(b)), indicating that nonalgal sediments in the lake did not rely on phytoplankton degradation activities, which is often the case for ocean, but mainly derived from land-originated materials due to river runoff injections, such as soil surface inorganic mineral salts, reactants, nonpoint source pollutions, or decompositions of biodegradable organic compounds.

The variation of $a_{NAP}(675)$ could also be attributed to SPM in two periods (Figures 5(c) vs 5(d)). The decrease of the relationship between $a_{NAP}(675)$ and SPM can be observed due to the reduction of SPM concentration from July to September (Figure 5(c)). And because of the rather low proportion of phytoplankton degradation products in detritus, the significance of Chl.a effect on $a_{NAP}(675)$ remained at a low level (Figure 5(d)).

It is also verified by previous research of Wu (2013), who showed that there were higher correlations between a_{NAP} and SPM in 2010 and 2011. Our results again confirm previous analysis in Section 3.1: lake SPM absorption was mainly associated with land-derived nonalgal detritus. Despite there were some decreases in September, nonalgal particles still dominated the absorption in both the blue and red spectra.

3.3. Variation of Algal Particulate Material Absorption.

Specific absorption represents absorption capacity or efficiency of algal particulates in SPM. Usually, it can be used to parameterize analytical algorithms to inverse the remote sensing signal into phytoplankton pigment centration, which is closely related with the carbon fixation rate at global or regional scales [27, 33, 34].

Spectral curves of phytoplankton particulate specific absorption derived from Equation (4) are present in Figure 6. It can be seen that $a_{ph}^*(\lambda)$ curves in July resembled the shape pattern of absorption curves in September, and there was more evident variability at 400–500 nm around 440 nm and at 650–700 nm around 675 nm.

In July, $a_{ph}^*(440)$ varied between 0.101 and 0.205 m^2/mg around an average of 0.145 m^2/mg, and $a_{ph}^*(675)$ was 0.056–0.111 m^2/mg with a mean value of 0.084 m^2/mg. In September, $a_{ph}^*(440)$ and $a_{ph}^*(675)$ increased to 0.115–0.424 m^2/mg and 0.067–0.169 m^2/mg, with an average of 0.229 m^2/mg and 0.107 m^2/mg, respectively.

Previous studies have demonstrated that fluctuations of $a_{ph}^*(\lambda)$ were mainly associated with relative contributions of accessory pigments (Chl.b, Chl.c, and carotenoids) and chlorophyll present in phytoplankton cells under different light and nutrient conditions [15, 17, 23, 32–35]. The increased abundance of accessory pigments tended to enhance the absorption of blue portion of the visible spectrum between 400 and 500 nm, while Chl.a constantly leads to a contribution focusing on 650–700 nm.

Therefore, the apparent variations of $a_{ph}^*(\lambda)$ here suggested that there might be evident changes in phytoplankton community or pigment compositions during study periods. To validate this speculation, $a_{ph}^*(\lambda)$ spectra were normalized to 440 nm in Figure 7. It could be clearly
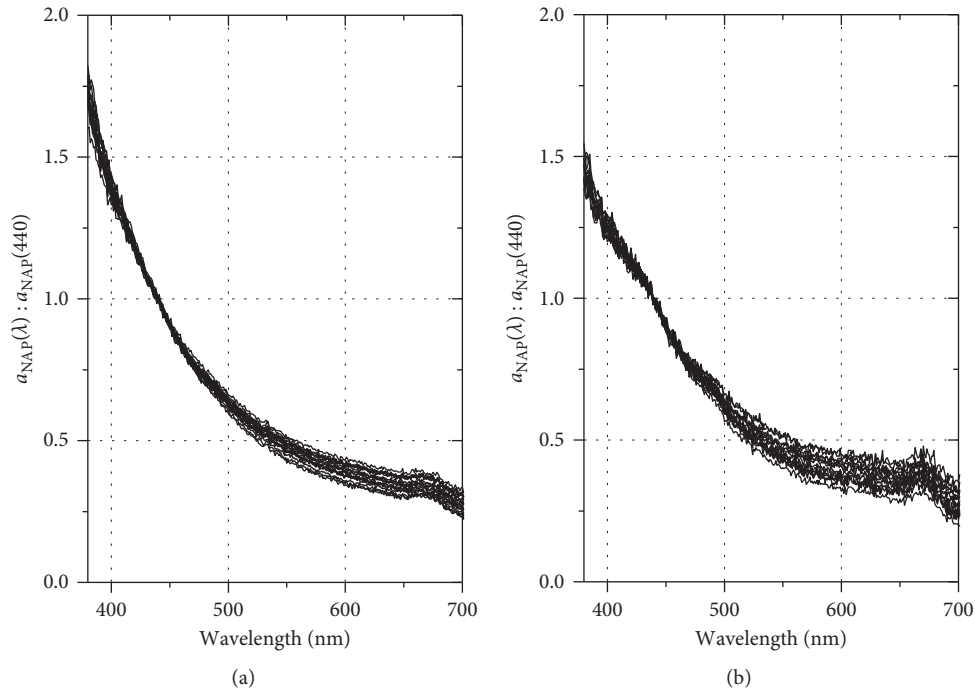
FIGURE 4: Nonalgal particulates of absorption spectra normalized to $a_{\text{NAP}}(440)$ in July (a) and September (b).

seen that compared to July, the ratio values at 675 nm $(a_{\text{ph}}^*(675) : a_{\text{ph}}^*(440))$ in September had decreased, exhibiting an increased effect of accessory pigments (Chl. b, Chl.c, and carotenoids).

While changes in optical absorption capacity in blue (at 440 nm) and red (at 675 nm) portions could be the consequence of pigment composition changes, the possible differences in the pigment concentration level and package effect in the specific trophic status during study periods may also be responsible for that.

Therefore, the variation of $a_{\text{ph}}^*(\lambda)$ due to pigment concentration (indicated by Chl.a) change was further analyzed using Equation (5), from which the strength of variations in $a_{\text{ph}}^*(\lambda)$ could be inferred by the exponent B (Figure 8).

Despite the fact that there was some dispersion, $a_{\text{ph}}^*(\lambda)$ exhibited a decreasing trend with increasing pigment concentration at 440 nm and 675 nm (Figure 8). To some extent, both the blue and red bands showed a decreasing trend because of an increasing package effect when pigment concentration in algal particles was elevated, but the decaying rate of optical absorption capacity was much faster on the blue band where optical absorption mainly associated with accessory pigments.

The variations of $a_{\text{ph}}^*(\lambda)$ were also found to be significant due to different phytoplankton constituents at different seasons by Wu (2013), which are similar to those found in Taihu Lake [35] and Chagan Lake [36]. It was also shown that the package effect might explain the higher a_{ph}^* values at 440 or 676 nm in Poyang Lake at a certain level when Chl. a was relatively lower compared with that of the most other water bodies [23].

With those observations and analysis illustrated in this section, it would be reasonable to confirm that the absorption capacity of algal particulates in SPM was dependent on the relative contributions of accessory pigments and chlorophyll in phytoplankton composition as well as the package effect and could fluctuate on the feature bands of the spectrum under various aquatic environments during flood time.

There is, however, some ambiguity in the partition of the relative contribution of the package effect and accessory pigments, which could be possibly intermingled with each other in the domain of 400–500 nm, and further research including more effective separation among algal compositions such as sodium hypochlorite bleaching or numerical separation method warranted to resolve these problems [23, 32, 34].

4. Conclusions

This study presents a case study of optical variations of suspended particulate material absorption during the flood time for Poyang Lake and provides more insight into the natural changes of the spectral parameters required for the parameterization of bio-optical models and remote sensing algorithms in this dynamic water environment under the background of climate change and anthropogenic impacts.

As one of the most representative inland waters in China, Poyang Lake exhibits an overall high level of suspended nonalgal detritus and algal concentration and lower water clarity during study periods, showing a strong absorption by total suspended sediments that are closely related with the land-derived nonalgal detritus material which varied

$y = 0.21x + 2.21$
$R^2 = 0.72$

$y = 0.12x + 1.49$
$R^2 = 0.70$

(a)

$y = 0.09x + 10.01$
$R^2 = 0.02$

$y = 0.05x + 3.08$
$R^2 = 0.07$

(b)

$y = 0.09x - 0.17$
$R^2 = 0.54$

$y = 0.02x + 0.83$
$R^2 = 0.22$

(c)

$y = 0.04x + 3.21$
$R^2 = 0.01$

$y = 0.01x + 1.11$
$R^2 = 0.02$

(d)
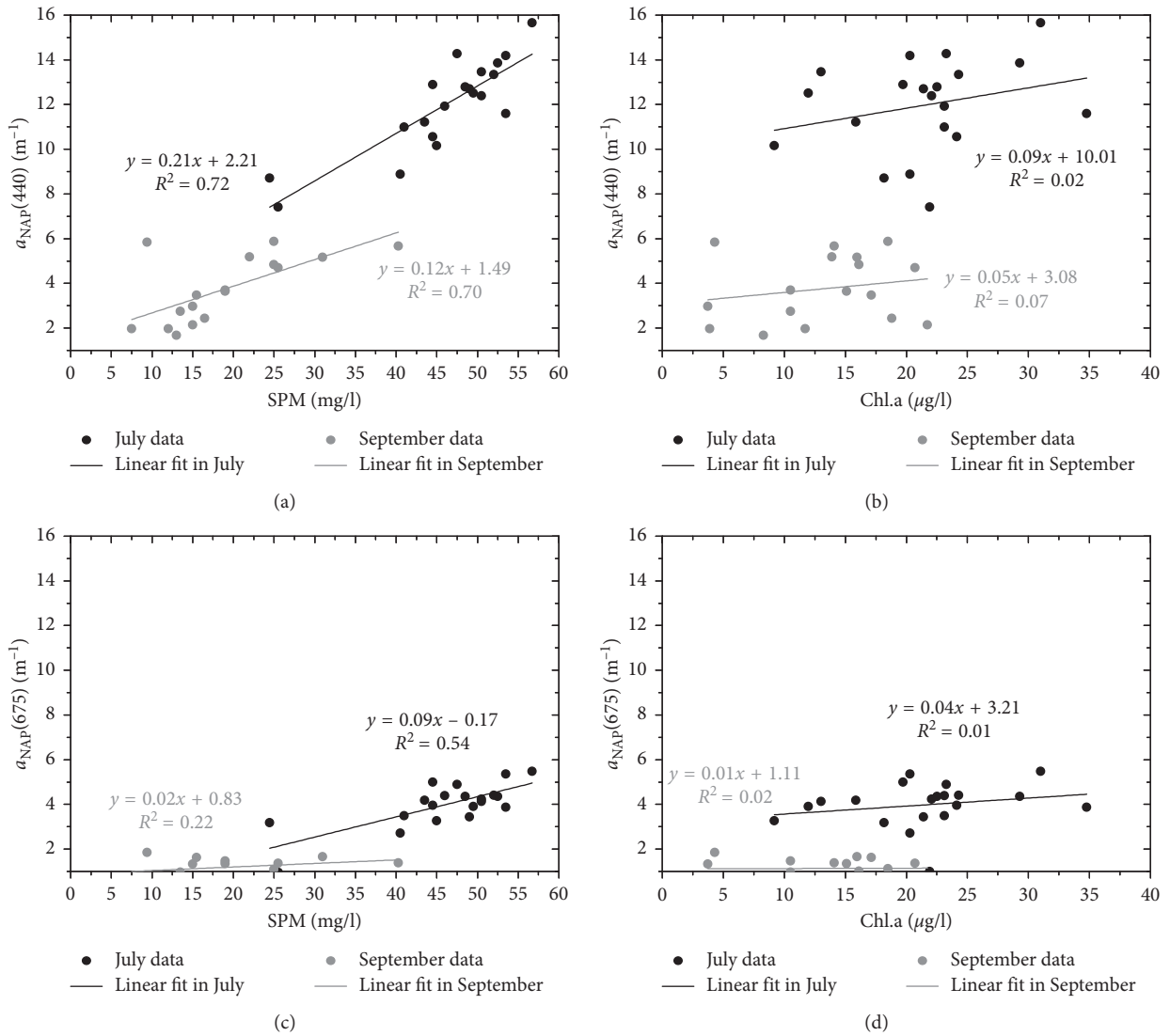
FIGURE 5: The linear relationships of $a_{NAP}(440)$ and $a_{NAP}(675)$ with SPM and Chl.a concentrations.

(a)

(b)
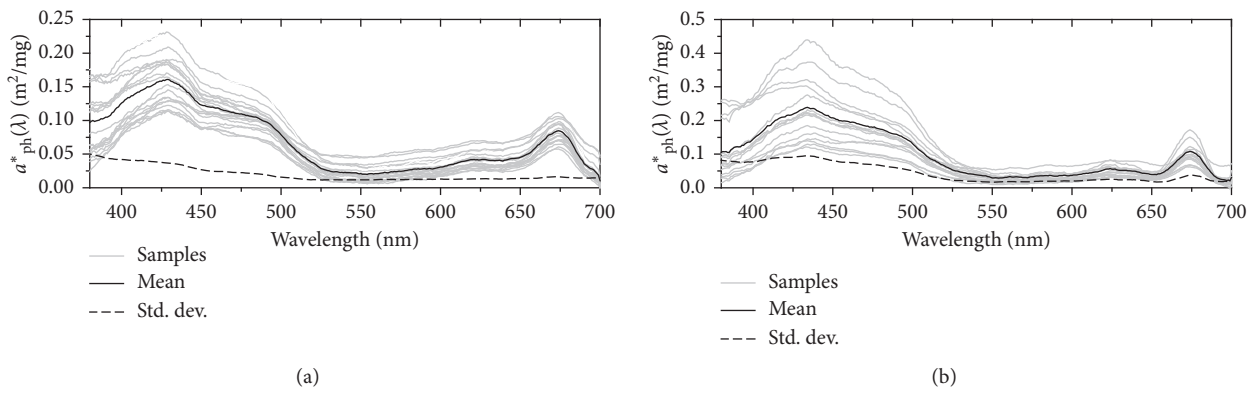
FIGURE 6: Phytoplankton specific absorption spectral curves in July (a) and September (b).

significantly with diverse proportions of minerals and organic materials from multiple sources loaded by river runoff injections, such as soil surface inorganic mineral salts [23, 24], reactants, nonpoint source pollutions, or decompositions of biodegradable organic compounds [4, 30, 32, 34].
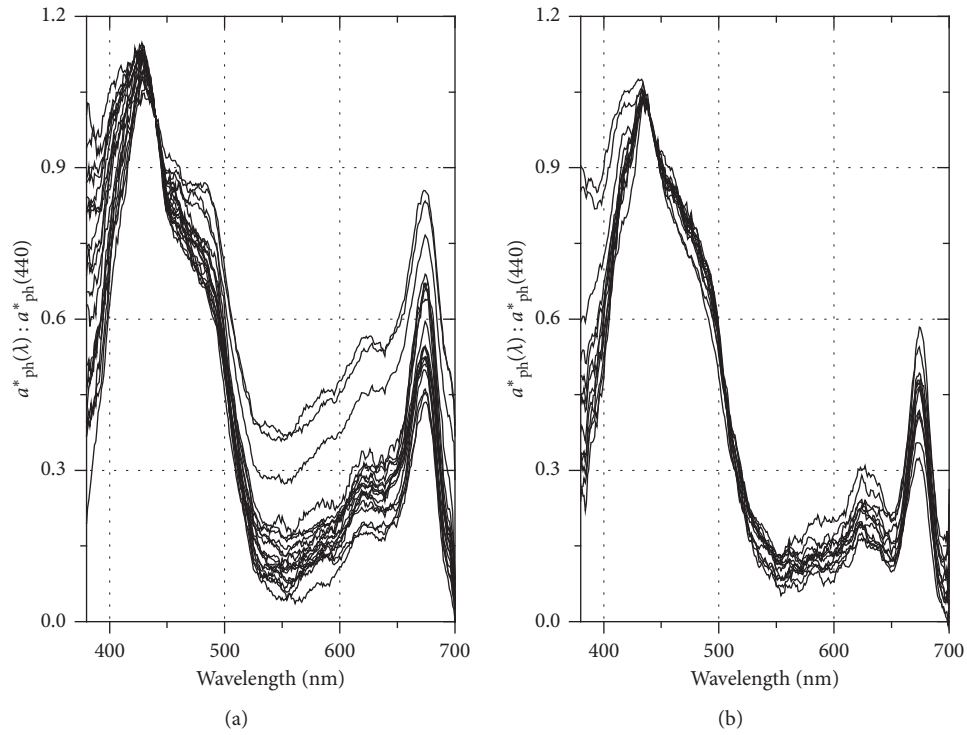
FIGURE 7: Specific absorption spectra normalized to $a^*_{\mathrm{ph}}(440)$ in July (a) and September (b).
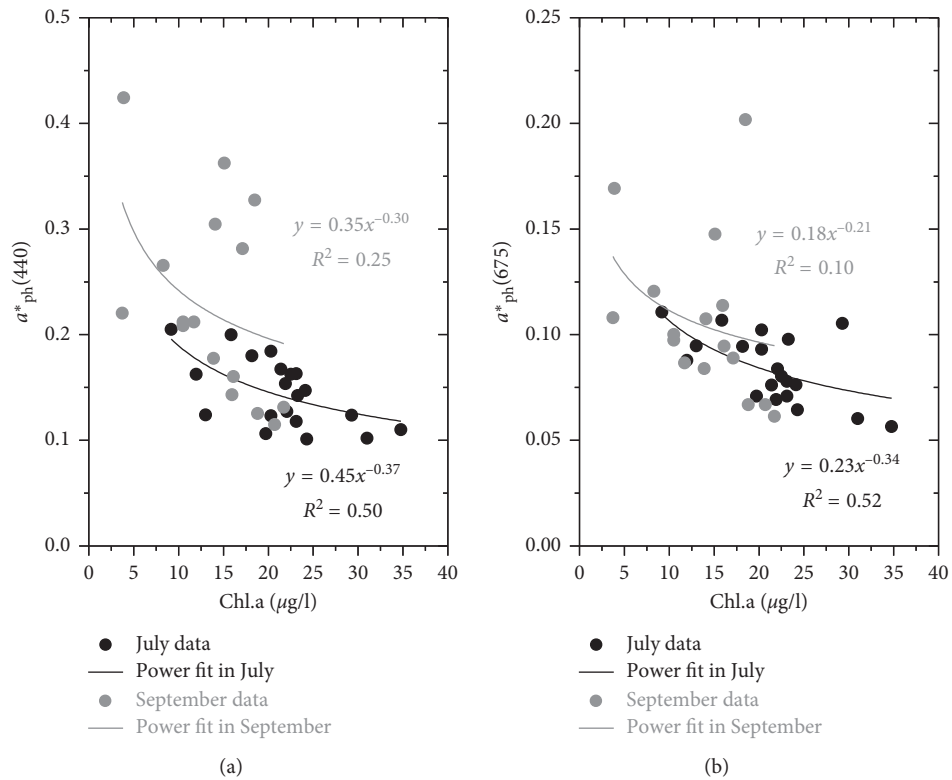
FIGURE 8: The power functions of $a^*_{\mathrm{ph}}(440)$, $a^*_{\mathrm{ph}}(675)$, and Chl.a.

Due to variations in phytoplankton community pigment composition, concentration, and package effect, there exists a difference between optical absorption capacity on blue (440) and red (675) portions of bands, the former of which had an obvious enhancement due to the increased effect of accessory pigments (Chl.b, Chl.c, and carotenoids) in suspended phytoplankton particles from July to September.

Evidence also presented that the nonlinear dependency of specific phytoplankton particulate absorption on pigment concentration for various trophic statuses in different periods could be unstable due to relative contributions of the package effect and accessory pigments, and this could bring uncertainties to the application accuracy of bio-optical models and remote sensing algorithms during parameterization.

There is still some ambiguity in the partition of the relative contribution of the package effect and accessory pigments, which might be intermingled in the domain of 400–500 nm, and further research including more effective separation among algal composition such as sodium hypochlorite bleaching or numerical separation method warranted to resolve these problems [23, 32, 34].

More works and studies are being carried out by researchers to learn about the spectral behavior of covaried optical active constituents present in this aquatic region, such as the identification of selective absorption of the dissolved organic material (DOM) onto sediments due to seasonal and dynamic biological activity (the presence of phytoplankton-derived DOM further processed by bacteria and/or by photo-oxidation) [27] and periodical covariation links between optical active materials [36], from which we hope to learn more about the impact of IOP variation on regional bio-optical model constructions and the interpretation of remote sensing observations in a changing environment.

Data Availability

All data generated or analyzed during this study are included in this article, and the original data are available from the corresponding author upon reasonable request.

Conflicts of Interest

The authors declare that they have no conflicts of interest.

Authors' Contributions

Yuandong Wang and Xibin You conceived and designed the experiments. Lianfang Yu performed the experiments. Yuandong Wang and Lihong Meng analyzed the data. Xiangming Xu contributed to the reagents and materials. Yuandong Wang and Guangxu Liu wrote and revised the paper.

Acknowledgments

References

[1] H. R. Gordon, O. B. Brown, and R. H. Evans, "A semianalytic radiance model of ocean color," *Journal of Geophysical Research*, vol. 93, no. D9, p. 10909, 1988.

[2] T. T John, B. M Colleen, and S. M. Timthy, "Remote sensing of physical cycles in lake superior using a spatio temporal analysis of optical water typologies," *Remote Sensing of Environment*, vol. 171, pp. 149–161, 2015.

[3] P Ammenberg, P Flink, and T. Lindell, "Bio-optical modelling combined with remote sensing to assess water quality," *International Journal of Remote Sensing*, vol. 23, no. 8, pp. 1621–1638, 2002.

[4] L. Hubert, M. Antoine, and V. Vincent, "Variability of suspended particulate material concentration in coastal waters under the Mekong's influence from ocean color (MERIS) remote sensing over the last decade," *Remote Sensing of Environment*, vol. 150, pp. 218–230, 2014.

[5] S. C. Palmer, P. D. Hunter, and T. Lankester, "Validation of Envisat MERIS algorithms for chlorophyll retrieval in a large, turbid and optically-complex shallow lake," *Remote Sensing of Environment*, vol. 157, pp. 158–169, 2015.

[6] A. Morel, "Optical modeling of the upper ocean in relation to its biogenous material content (Case I waters)," *Journal of Geophysical Research*, vol. 93, no. C9, pp. 10749–10768, 1988.

[7] B. G. Mitchell, A. Bricaud, K. Carder et al., "Determination of spectral absorption coefficients of particles, dissolved material and phytoplankton for discrete water samples," in *Ocean Optics Protocols For Satellite Ocean Color Sensor Validation, Revision 2, NASA Technical Memorandum 2000-209966*, G. S. Fargion, J. L. Mueller, and C. R. McClain, Eds., pp. 125–153, NASA Goddard Space Flight Center, Greenbelt, MD, USA, 2000.

[8] R. A. Reynolds, D. Stramski, and E. B. G. Mitchell, "A chlorophyll-dependent semianalytical reflectance model derived from field measurement of absorption and backscattering coefficients within the Southern Ocean," *Journal of Geophysical Research*, vol. 106, no. C4, pp. 7125–7138, 2001.

[9] A. Morel and S. Maritorena, "Bio-optical properties of oceanic waters: a reappraisal," *Journal of Geophysical Research*, vol. 106, no. C4, pp. 7163–7180, 2001.

[10] C. J. Stephanie, T. K. Palmer, and D. H. Peter, "Remote sensing of inland waters: challenges, progress and future directions," *Remote Sensing of Environment*, vol. 157, pp. 1–8, 2015.

[11] S. Bagheri, C. Zetlin, and R. Dios, "Estimation of optical properties of nearshore water," *International Journal of Remote Sensing*, vol. 20, no. 17, pp. 3393–3397, 2010.

[12] B. P. David, F. R. James, and A. G. Gower, "A review of ocean color remote sensing methods and statistical techniques for the detection, mapping and analysis of phytoplankton blooms in coastal and open oceans," *Progress in Oceanography*, vol. 123, no. 4, pp. 123–144, 2014.

[13] D. Katja and O. Natascha, "Remote sensing for lake research and monitoring–Recent advances," *Ecological Indicators*, vol. 64, pp. 105–122, 2016.

[14] D. G. Bowers, G. E. L. Harker, and B. Stephan, "Absorption spectra of inorganic particles in the Irish Sea and its relation to tidal stirring," *International Journal of Remote Sensing*, vol. 17, no. 12, pp. 2789–2805, 1996.

[15] M. Babin, D. Stramski, G. M. Ferrari, and H. Claustre, "Variations in the light absorption coefficients of sssphyto-plankton, non-algal particles, and dissolved organic material in coastal waters around Europe," *Journal of Geophysical Research*, vol. 108, no. C7, p. 3211, 2003.

[16] B. M. Colleen, G. Steven, and A. Dirk, "Aquatic color radiometry remote sensing of coastal and inland waters: Challenges and recommendations for future satellite missions," *Remote Sensing of Environment*, vol. 160, pp. 15–30, 2015.

[17] W. Zhang, X. L. Chen, L. Q. Tian et al., "Temporal and spatial variations of TSM concentration in Poyang Lake: observations from HJ-1A/1B satellite CCD imagery," *Journal of Central China Normal University (Natural Sciences)*, vol. 47, no. 3, pp. 416–420, 2013.

[18] W. X. Cao, Y. Z. Yang, and X. Q. Xu, "Regional patterns of phytoplankton spectral absorption in the Pearl river estuary," *Chinese Science Bulletin*, vol. 48, no. 17, pp. 1876–1882, 2003.

[19] G. P. Wu and Y. B. Liu, "Capturing variations in inundation with satellite remote sensing in amorphologically complex, large lake," *Journal of Hydrology*, vol. 523, no. 6, pp. 14–23, 2015.

[20] D. Stramski, S. B. Wozniak, and P. J. Flatau, "Optical properties of Asian mineral dust suspended in seawater," *Limnology and Oceanography*, vol. 49, no. 3, pp. 749–755, 2004.

[21] L. Linhai, L. Lin, S. Kaishan, and L. Yunmei, "An inversion model for deriving inherent optical properties of inland waters: Establishment, validation and application," *Remote Sensing of Environment*, vol. 135, pp. 150–166, 2015.

[22] L. Q. Chen, X. L. Chen, and L. Q. Tian, "Partitioning of the suspended particulate spectral scattering coefficient in Poyang lake," *Spectroscopy and Spectral Analysis*, vol. 32, no. 3, pp. 729–733, 2012.

[23] G. F. Wu, L. J. Cui, H. T. Duan, T. Fei, and Y. L. Liu, "Specifc absorption and backscattering coefficients of the main water constituents in Poyang lake, China," *Environmental Monitoring and Assessment*, vol. 185, no. C13, pp. 4191–4206, 2013.

[24] G. F. Wu, L. J. Cui, J. J. He, H. T. Duan et al., "Comparison of MODIS-based models for retrieving suspended particulate matter concentrations in Poyang lake, China," *International Journal of Applied Earth Observation and Geoinformation*, vol. 24, no. 1, pp. 63–72, 2013.

[25] G. Claudia, B. Mariano, and V. Emiliana, "Airborne hyperspectral data to assess suspended particulate material and aquatic vegetation in a shallow and turbid lake," *Remote Sensing of Environment*, vol. 157, pp. 48–57, 2015.

[26] Z. Wu, Y. Cai, X. Liu, C. P. Xu, Y. Chen, and L. Zhang, "Temporal and spatial variability of phytoplankton in Lake Poyang: the largest freshwater lake in China," *Journal of Great Lakes Research*, vol. 39, no. 3, pp. 476–483, 2013.

[27] J. Xu, Y. Q. Wang, D. Gao, Z. R. Yan, C. Gao, and L. L. Wang, "Optical properties and spatial distribution of chromophoric dissolved organic matter (CDOM) in Poyang lake, China," *Journal of Great Lakes Research*, vol. 43, no. 4, pp. 700–709, 2017.

[28] X. Mei, Z. Dai, J. Du, and J. Chen, "Linkage between Three Gorges Dam impacts and the dramatic recessions in China's largest freshwater lake, Poyang Lake," *Scientific Reports*, vol. 5, 2015.

[29] S. Lei, X. P. Zhang, and R. F. Li, "Analysis the changes of annual for Poyang lake wetland-vegetation based on MODIS monitoring," *Procedia Environmental Sciences*, vol. 10, no. 4, pp. 1840–1846, 2011.

[30] A. Beldjazia and D. Alatou, "Precipitation variability on the massif Forest of Mahouna (North Eastern-Algeria) from 1986 to 2010," *International Journal of Management Sciences and Business Research*, vol. 5, no. 3, pp. 21–28, 2016.

[31] C. S. Roesler, "Theoretical and experimental approaches to improve the accuracy of particulate absorption coefficients derived from the quantitative filter technique," *Limnology & Oceanography*, vol. 43, pp. 1649–1660, 1998.

[32] B. G. Mitchel, M. Kahru, and J. Wieland, Determination of spectral absorption coefficients of particles, dissolved material and phytoplankton for discrete water samples. Ocean optics protocols for satellite ocean colour sensor validation, Revision 4, Volume IV: Inherent optical properties: Instruments, characterizations, field measurements and data analysis protocols, Goddard Space Flight Center Technical Memorandum, 01674, 2003.

[33] W. M. Mark, "Eutrophication and cyanobacterial blooms in South African inland waters: 10 years of MERIS observations," *Remote Sensing of Environment*, vol. 155, pp. 161–171, 2014.

[34] A. Bricaud, A. Morel, and M. Babin, "Variations of light absorption by suspended particles with chlorophyll a concentration in oceanic (case 1) waters: analysis and implications for bio-optical models," *Journal of Geophysical Research*, vol. 103, no. C13, pp. 31033–31044, 1998.

[35] R. H. Ma, D. L. Pan, H. T. Duan et al., "Absorption and scattering properties of water body in Taihu lake, China: backscattering," *International Journal of Remote Sensing*, vol. 30, no. 9, pp. 2321–2335, 2009.

[36] Y. D. Wang, D. W. Liu, K. S. Song, J. Du et al., "Characterization of water constituents spectra absorption in Chagan lake of Jilin province, Northeast China," *Chinese Geographical Science*, vol. 21, no. 3, pp. 334–345, 2011.

Research Article

Discretization of the Water Uptake Process of Na-Montmorillonite Undergoing Atmospheric Stress: XRD Modeling Approach

Walid Oueslati [ORCID] and Mahdi Meftah

UR 05/13-01 Physique des Matériaux Lamellaires et Nano-Matériaux Hybrides (PMLNMH), Faculté des Sciences de Bizerte, Université de Carthage, 7021 Zarzouna, Tunisia

Correspondence should be addressed to Walid Oueslati; walidoueslati@ymail.com

This work focuses on the water-montmorillonite interaction under variable atmospheric conditions in order to characterize the interlamellar space (IS) configuration for possible use in the context of geological barrier for radioactive and industrial waste confinement. Atmospheric stress is achieved by applying, for Na-rich montmorillonite, a water sorption/desorption constraint, created at the laboratory scale. This hydrological disturbance allows the "demolition" of the clay history and to highlight the clay hydrous performance. The structural analysis is achieved using modeling of XRD profiles, which allowed us to determine the optimal structural parameters describing the IS configuration along the c^* axis. During the "in situ" XRD analysis, a sorption/desorption cycle is envisaged by variation of the relative humidity rate (%RH) from the saturated condition (94 %RH) towards extremely dry ones (2-3 %RH). Qualitatively, a new hydration hysteresis behavior of the "stressed" sample appears. Structural analysis achieved before and after perturbation allowed us to identify, respectively, the homogeneous hydration states, the hydrous transition domains, and the hydration heterogeneity degree. This latter parameter is characterized, quantitatively, by variable relative abundances of mixed-layer structure (MLS) population discerned over a wide explored RH range. Using the optimum structural parameter, the water molecule distribution versus the applied hydrous strain was quantified.

1. Introduction

The use of the smectite clay, like montmorillonite, as an canister envelope or as plugs or rock grout, in the context of geological barrier for industrial and/or radioactive hazardous waste confinement constitutes a green solution for severe environmental problems. In this regard, montmorillonite will be exposed to several environmental constraints (temperature cycle, extremely saturated conditions, high water pressure, etc.). Under these conditions, the clay-sealing ability is influenced, and two different scenarios can take place: (1) the crystal lattices may undergo permanent changes resulting in a largely reduced swelling and gel-forming capacity, and (2) the microstructure may become temporarily or permanently altered, which affects the cation exchange process [1–7].

The crystal structure of smectite consists of two sheets of principally tetrahedral Si with minor Al sandwiched to the top and bottom of a layer of octahedrally coordinated cations, usually Al but with some Mg and Fe [8, 9]. Furthermore, isomorphic substitution causes internal negative charges in the lamellae. The negative charges are compensated by adsorption of ions near the external surfaces of the clay minerals.

The smectite group of clay minerals with 2 : 1 layer structure is able to expand and contract its structures while maintaining its crystallographic integrity. Expansion takes place as water or some polar molecules enter the interlayer space [10].

The layers expand because the exchangeable cations attract more water than the relatively small layer charge [11]. The swelling is characterized by a stepwise expansion of the layer-to-layer distance with increasing water activity. This expansion has been described by the incorporation of 1, 2, and 3 planes of interlayer H_2O molecules, leading to the well-known 1W (d_{001} = 11.6–12.9 Å), 2W (d_{001} = 14.9–15.7 Å), and

3W ($d_{001} = 18$–19 Å) hydration states, in addition to the dehydrated one, 0W ($d_{001} = 9.6$–10.2 Å) [12].

The swelling of montmorillonite in various liquid systems has been investigated by several authors. These studies have focused on many parameters that come into play during the chemical clay-environment interaction. Indeed, to evaluate the mechanisms causing changes in the soil structure, Kaya and Fang [13] show that the physicochemical properties (i.e., cation exchange capacity (CEC), zeta potential (ζ), surface charge density, pore-size distribution, and Atterberg limits) of kaolinite, bentonite, and a local soil as the dielectric constant of the pore fluid change, such that as the dielectric constant of the pore fluid approaches that of the soil, the repulsive and attractive forces diminish. Smectite hydration and interlayer structure have been widely studied from both experimental and computational methods, mainly using X-ray diffraction (XRD) and some theoretical methods [14–31]. The studies [20, 32] show that hydration of swelling clays increases their basal spacing stepwise. Dazas et al. [31] investigate, under near-saturated conditions, the interlayer structure model of trihydrated low-charge smectite by X-ray diffraction and Monte Carlo modeling method. Oueslati et al. [29] characterize, using quantitative XRD analysis, the effect of the chemical composition of the soil solution on the structural change of Na-montmorillonite materials. On the contrary [30, 33], they investigate the effect of an environmental constraint, created in situ by varying the relative humidity rate, on the cation exchange performance and the structural changes of Na-montmorillonite in contact with Cd^{2+}, Co^{2+}, Zn^{2+}, Ni^{2+}, and Ba^{2+} chloride solutions.

Within this scope, and in extension with earlier works, this study is aimed at quantifying using the XRD modeling approach, the effect of an in situ applied hydrous perturbation on the hydration behavior and the structural changes of the most used host material in the earlier studies (i.e., the Na-exchanged montmorillonite). The structural parameters were determined by quantitative XRD analysis using an indirect method based on the comparison of the experimental 00l reflections with those calculated from structural models. This investigation allowed us to determine, respectively, the nature, amounts, position, and organization of exchangeable cations in the interlamellar space, along the c^* axis.

2. Materials and Methods

2.1. Starting Materials.
The dioctahedral smectite used in this work is a reference montmorillonite sample (SWy-2) from the Source Clays Repository of The Clay Minerals Society [34]. The host material is characterized by a half-cell structural formula as follows [35]:

$$\left(Si_{3.923}Al_{0.077}\right)\left(Al_{1.459}Ti^{4+}_{0.018}Fe^{3+}_{0.039}Fe^{2+}_{0.045}Mg^{2+}_{0.382}\right)$$
$$O_{10}\left(OH\right)_2\left(Ca^{2+}_{0.177}Na^{+}_{0.027}\right) \tag{1}$$
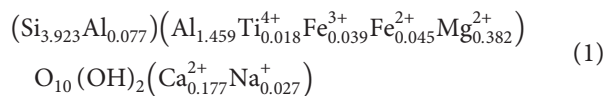
This clay mineral represents a major octahedral charge and exhibits an extremely limited substitution in the tetrahedral sheets where the cation exchange capacity (CEC) is 101 meq/100 g [36]. In order to guarantee a maximum dispersion, a preliminary treatment for the host materials is performed. The Na-rich montmorillonite suspension is prepared according

to a classical protocol [37]. The obtained sample is referred to as SWy-2-Na.

2.2. Hydrous Perturbation.
In order to achieve an atmospheric constraint (i.e., desorption process), a starting material suspension is placed in a sand bath at 50°C for 24 h to ensure a complete drying process. This sample undergoes a second humectation route (sorption process) by excessive addition of water followed by a moderate agitation. These two steps are repeated 50 times to ensure the destruction of the sample hydration history which is a principal parameter affecting its probable long use in the context of geological barrier.

2.3. XRD Measurements.
For all samples, oriented slides were prepared by drying at room temperature an aqueous clay suspension on glass slides. XRD patterns were then recorded using a Bruker D8 diffractometer equipped with an MHG Messtechnik humidity controller coupled to an Anton Paar CHC+ chamber. Experimental XRD patterns were registered every 3 %RH scale at the fixed relative humidity condition values. Intensities were measured with a SolXE Si(Li) solid-state detector (Baltic Scientific Instruments) for 4 s per 0.04° 2θ step over the 2–32° 2θ Cu-Kα angular range. The divergence slit, the two Soller slits, the antiscatter slits, and the resolution slits were 0.3°, 2.3°, 0.3°, and 0.1°, respectively.

The samples were kept at 23°C in the CHC+ chamber during the whole data collection. The samples were kept also under a constant flow of mixed dry/saturated air to maintain the desired relative humidity (RH) after an initial equilibration. RH was continuously monitored with a hygrometer located close to the sample. To carry out the adsorption cycle, the RH value extended from 4% to the almost saturated condition (94 %RH). The reverse cycle (i.e., desorption) is accomplished by varying the moisture values in the opposite direction starting the dehydration process from 94 %RH and decreasing towards extremely dry ones (4 %RH).

2.3.1. Semiquantitative XRD Investigation.
The diffractometer installation is monitored by DIFFRACPlus software (Bruker AXS GmbH, Karlsruhe, Germany) which allowed the calculation of qualitative parameters such as the basal spacing d_{001} from the first-order (001) Bragg reflections; the FWHM (full width at the half maximum intensity for the 001 reflection) and the rationality of the reflection position (ξ) related to the 00l reflections [38]. The combination of semiquantitative parameters with the profile geometry description (i.e., symmetric and asymmetric X-ray peaks) provides preliminary information about the hydration state evolution all over the explored RH range.

2.3.2. Quantitative XRD Investigation.
The XRD modeling method is widely used to quantify hydration properties of smectite as a function of relative humidity [12, 13, 24–30, 33, 39, 40]. This indirect method consists of adjusting the experimental patterns by fitting positions and profiles of the 00l reflections over the explored angular range. Theoretical XRD patterns are calculated using the algorithms developed
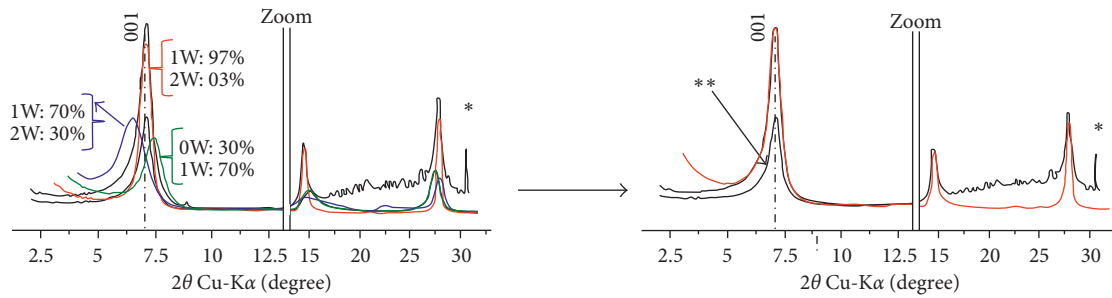
FIGURE 1: Example of an experimental XRD profile modeled using three MLSs containing (97%-1W, 3%-2W), (30%-0W, 70%-1W), and (70%-1W, 30%-2W), respectively. *Halite (NaCl) complex, **the 001 line is recorded twice time in order to check the sample balance with its environment.

in [41] and detailed later in [42]. The abundances of the diverse layer types (W_i), the mode of stacking of the different kinds of layers, and the mean number of layers per coherent scattering domain (CSD) are determined through XRD profile modeling. Within a CSD, the stacking of layers is described by a set of junction probability parameters (P_{ij}). The relationships between these probabilities and the abundances W_i of the different types of layers are given in [41]. All XRD profiles are simulated following the fitting strategy detailed in [24, 25], where the authors reproduce the experimental XRD pattern using various contributions to obtain a good fit, when it is not obtained with a unique periodic structure. Each contribution contains different layer types in variable proportions. However, the use of two or more mixed-layer structures to fit all features of experimental XRD patterns does not imply the actual presence of two or more populations of particles in the sample as discussed below. As a consequence, layers in the same hydration state as those present in the different mixed-layer structures must have identical properties at a given RH value. Each given layer type was thus assigned a unique chemical composition, a unique layer thickness value, and a unique set of atomic coordinates for all mixed-layer structures at a given RH. A detailed example of an experimental XRD profile modeled using three MLSs containing (97%-1W, 3%-2W), (30%-0W, 70%-1W), and (70%-1W, 30%-2W), respectively, is reported in Figure 1.

3. Results

3.1. Unstressed Sample

3.1.1. Qualitative XRD Analysis

(1) Sorption Process. For the starting materials, the evolution of the experimental XRD patterns versus %RH, reported in the Figure S1, shows a significant fluctuation of the position and intensity of the investigated 00*l* reflection along the hydration process. An additional reflection attributed to the Halite crystallization is present in up to 60 %RH. The qualitative investigation of the d_{001} value evolution, the FWHM, and the ξ parameters versus %RH (Figure 2) indicates heterogeneous hydration behavior for the transitional hydration state domain. This character is confirmed by the obtained high value of the cited parameters [29]. Based on this criterion, three principal transitional hydration domains along the sorption

process can be reached and situated, respectively, between 10 and 34 %RH for 0W-1W, 49–67 %RH for 1W-2W, and 91–94 %RH for 2W-3W. For the three defined RH transition ranges, the XRD patterns are characterized by an asymmetric 001 reflection geometry accompanied by the corresponding high FWHM and ξ values (i.e., at 22 %RH, FWHM = 2.48° (2θ) and ξ = 1.84 Å; at 55 %RH, FWHM = 1.45° (2θ) and ξ = 1.58 Å; at 91 %RH, FWHM = 0.867° (2θ) and ξ = 1.13 Å), indicating probably an interstratified hydration character with more one layer type. Indeed, the d_{001} value shifts gradually from 0W (9.98 Å) towards 3W (18.86 Å) layer-type phase for the extreme %RH condition. The greatest clear 1W → 2W transition is observed from 52 %RH to 61 %RH. The 2W → 3W transition is observed from 85 %RH to 94 %RH.

(2) Desorption Process. The desorption sequence is achieved by decreasing the RH rate. The d_{001} basal spacing shifts from 18.86 Å, characteristic of a 3W hydration state (3W), to 9.96 Å, characteristic of a dehydrated state (0W). This evolution presents characteristic levels of almost homogeneous hydration states of hydration (3W, 2W, and 1W). Furthermore, there are transition regions 3W → 2W, 2W → 1W, and 1W → 0W, which are characterized by experimental profiles with an asymmetric diffraction line shape and an irrationality of the reflection positions, indicating probably a possible interstratified hydration state (Figure S2 and Figure 2). By comparing the widths (as a function of %RH) of the transition domains along the sorption and desorption processes (Figure 2), an offset is shown for 2W → 1W and 1W → 0W transitions.

Indeed, the 2W → 1W transition starts from 52 %RH and ends at 34 %RH, which is the RH value where the same transition ends during the sorption process. Similarly for the 1W → 0W transition, which starts from 13 %RH and ends at 4 %RH, there is a large offset to the hydration process whose 1W → 0W transition starts at 13 %RH and ends at 34 %RH.

This hydrous behavior shows the existence of hydration hysteresis reported in Figure 2. Also, during the desorption process, the absence of the pure dehydrated phase (0W), despite having reached the limit of 4 %RH, is noted.

In order to decode the insertion/disengagement mechanism of IS water molecules, this result can be explained by a freedom degree decrease for all the constituents inside the IS, which complicate the water molecule release process.

This fact can be interpreted by a transformation of the free water from the surrounding environment into structural

(a)

(b)

(c)
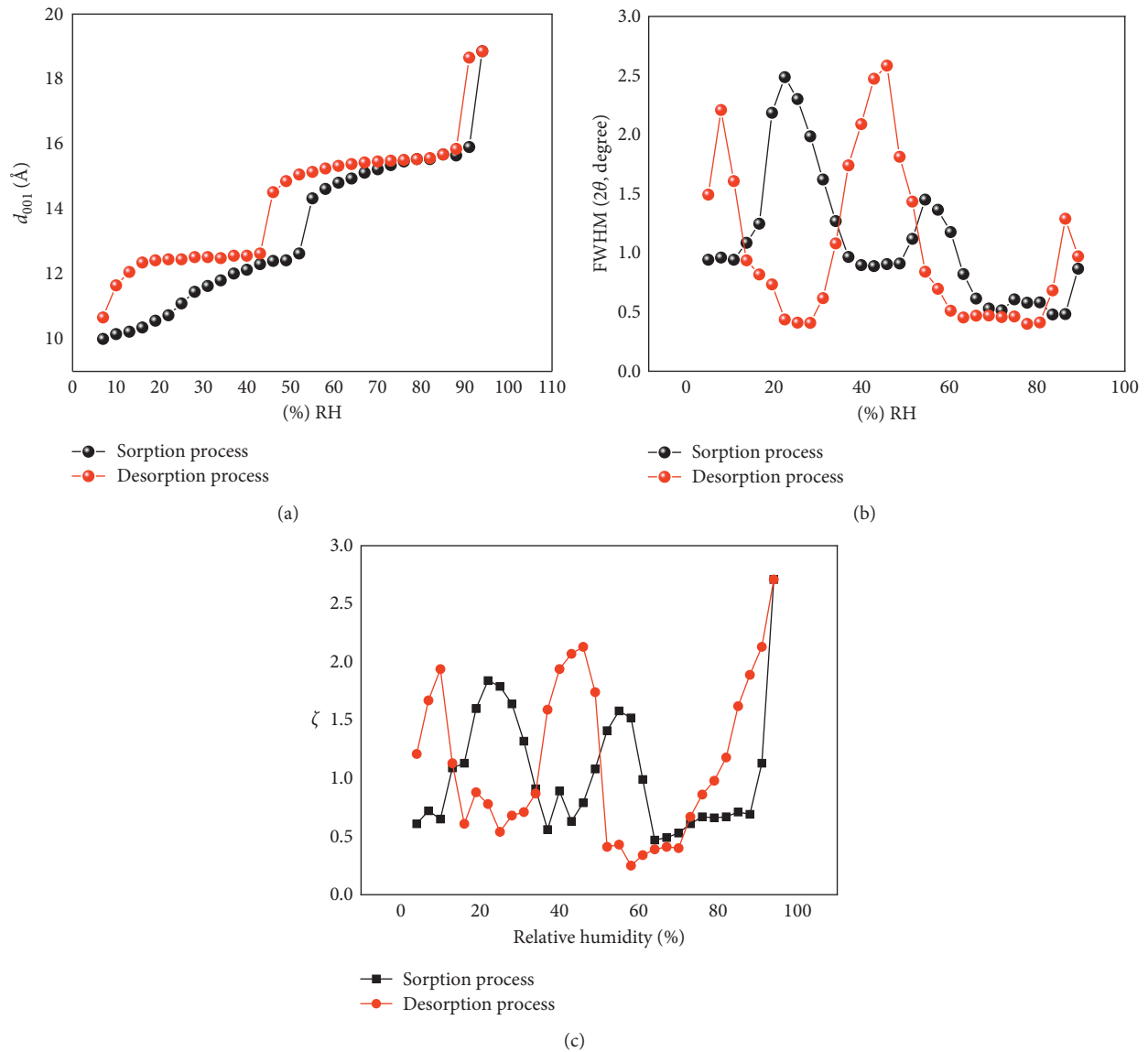
FIGURE 2: Evolution of the d_{001} (a), FWHM (b), and ξ parameters (c) versus %RH in the case of the unstressed sample along the sorption and desorption processes. The ξ parameter, which accounts for the departure from rationality of the 00l reflection series, is calculated as the standard deviation of the $l \times d_{00l}$ values calculated for the X_i measurable reflections ($X_i = 3$ in this case) over the 2θ Cu-Kα angular range (degree). Blue and yellow circles indicate interstratified hydration character (I) and homogeneous hydration character (H).

water, incorporated in the internal and external pore surfaces, which complicates its loss by dehydration.

The investigation of FWHM and ξ parameter shows the difference between the two processes for the transitions 2W $\rightarrow$ 1W and 1W $\rightarrow$ 0W (Figure 2). This problem does not arise for the 3W $\rightarrow$ 2W transition if we want to compare it with the 2W $\rightarrow$ 3W transition along the hydration process. Indeed, in this case, the high %RH value induces an elevated amount of water present in the IS; thereafter, the existence of a large fraction of water considered as "free water" will facilitate the process of dehydration.

3.1.2. Quantitative XRD Analysis

(1) Sorption Process. The hydration behavior obtained from the qualitative XRD analysis is refined by the

quantitative analysis in order to quantify the clay "particle" composition.

The obtained best agreements between experimental and calculated intensity are reported in Figure S1, where a selection in the presentation was made in order to view areas with large fluctuations in the basal spacing value. All structural parameters used to fit experimental pattern are reported in Table 1 and Figure 3.

The distribution of water molecules in the theoretical model respects the results published in the literature [24, 29]. Indeed, for the 1W hydration state, one water sheet is located in the middle of the IS at the same position as the exchangeable cation. For the 2W hydration state, two water sheets are distributed on both sides of the middle of the IS. For the 3W hydration state, the exchangeable cation "bathes" in 3 water sheets superimposed along the c^* axis.

TABLE 1: Some structural parameters obtained from the quantitative XRD analysis in the case of the unstressed sample along the sorption process.

%RH	Layer stacking mode*	M
4	R0 — R0	7
7	R0 — R0	7
10	R0 — R0	8
13	R0 — R1 ($P_{AA} = 0.80$)	8
16	R1 ($P_{AA} = 0.85$) R0 — R1 ($P_{AA} = 0.85$)	8
19	R1 ($P_{AA} = 0.70$) R0 — R1 ($P_{AA} = 0.85$)	8
22	R1 ($P_{AA} = 0.70$) R1 ($P_{AA} = 0.75$) R1 ($P_{AA} = 0.70$)	8
25	R0 R1 ($P_{AA} = 0.75$)	9
28	R1 ($P_{AA} = 0.75$)	9
31	R1 ($P_{AA} = 0.75$)	7
34	R1 ($P_{AA} = 0.70$)	6
37	R1 ($P_{AA} = 0.70$) R1 ($P_{AA} = 0.70$)	6
40	R1 ($P_{AA} = 0.70$)	5
43	R1 ($P_{AA} = 0.75$)	5
46	R1 ($P_{AA} = 0.87$) R1 ($P_{AA} = 0.70$)	5
49	R0 R1 ($P_{AA} = 0.87$) R1 ($P_{AA} = 0.70$)	5
52	R0 R1 ($P_{AA} = 0.85$) R1 ($P_{AA} = 0.96$) R1 ($P_{AA} = 0.70$)	5
55	R1 ($P_{AA} = 0.70$) R1 ($P_{AA} = 0.70$) R1 ($P_{AA} = 0.90$)	5
58	R0 R1 ($P_{AA} = 0.70$) R1 ($P_{AA} = 0.90$) R1 ($P_{AA} = 0.75$)	6
61	R1 ($P_{AA} = 0.75$) R1 ($P_{AA} = 0.88$)	6
64	R1 ($P_{AA} = 0.75$)	5
67	R1 ($P_{AA} = 0.80$)	5
70	R1 ($P_{AA} = 0.85$)	5
73	R1 ($P_{AA} = 0.85$)	5
76	— R0 R0	5
79	— R0 R0	5

TABLE 1: Continued.

%RH	Layer stacking mode*	M
82	— R0 R0	5
85	— R0 R0	7
88	R0 R0	7
91	R0 R0	7
94	R0 R0	6

Note: 3W, 2W, 1W, and 0W are attributed to the layer hydration state. n_{H_2O}: the number of H_2O molecules per half unit cell is fixed to 2.5, 5.6, and 6.1, respectively, for 1W, 2W, and 3W. Z_{Na}: the position of exchangeable cations per half unit cell calculated along the c^* axis is fixed to 8.30 Å, 9.50 Å, 11.25 Å, and 12.60 Å, respectively, for 0W, 1W, 2W, and 3W hydration state. n_{Na}: the number of H_2O molecules per half unit cell is fixed to 0.33, indicating full saturation of the cation exchange capacity (CEC) of the minerals. *R, Reichweite factor; R0 and R1 describe the MLS with random interstratifications or with partial segregation; M: the average number of layers per particle; P_{AA}: layer succession law.

During the hydration process and for RH up to 43%, the experimental profile is reproduced by interstratification between the 0W and 1W phases with variable proportions, indicating the absence of a mono-homogeneous phase at 0W for humidity below 13 %RH (Figure 3).

On the contrary, an introduction of an R1 stacking mode type is noted at 13 %RH, which is consistent with the variation of the FWHM and ξ parameters. The first appearance of the 2W phase begins at 46 %RH and maintains a heterogeneous hydration state between 3 layer types (0W, 1W, and 2W) up to 58 %RH, where the structure is reproduced using a random distribution between the three mentioned phases. From 61 %RH, the contribution of the 0W phase disappears, and the experimental profile is completely reproduced by a combination of the 1W and 2W phases up to 76 %RH, where a minority phase related to the 3W hydration state is introduced. This combination continues up to 91 %RH, and then the 1W phase contribution disappears and the structure is completely modeled by 2W and 3W layer types. It should be noted that, at 94 % RH, the experimental diffractogram is reproduced by a majority 3W phase and the sample retains its interstratified character, which is in contradiction with the qualitative description mentioning a homogeneous phase. In contrast to the qualitative analysis, the quantitative analysis allowed us to show the existence of structural heterogeneities related to the coexistence of populations of several layers within the clay particle over the whole explored RH range.

(2) Desorption Process. For the desorption sequence and by decreasing humidity values up to 64 %RH, the experimental profile is modeled by a distribution of the two phases,

FIGURE 3: Schematic representation of the structure model used to fit the experimental XRD pattern in the case of the unstressed sample along the sorption process. Relative proportions, expressed in wt.%, of the three elementary mixed-layer structure (MLS) contributions are plotted on the y-axis, whereas their compositions (relative proportions of the different layer types) are plotted on the x-axis.

respectively, 3W and 2W. The basal distances and the proportions of the phase contributions used indicate a transition to the 2W hydration state. From 61 %RH and up to 58 % RH, the experimental profile is fully reproduced using segregated three phases mixed randomly. From 55 %RH and up to 34 %RH, the 3W phase disappears, which means a high retention of the water content, despite the relatively

low RH and the absence of a sudden transition. At this humidity range, the structure is reproduced by a 2W/1W mixed structure. The first appearance of the 0W phase is obtained at 31 %RH, and its contribution in the theoretical model continues to increase as a function of the decrease in the RH rate. It should be noted that, for humidity ranging from 40 to 16 %RH, layers are stacked with random

TABLE 2: Some structural parameters obtained from the quantitative XRD analysis in the case of the unstressed sample along the desorption process.

TABLE 2: Continued.

%RH	Layer stacking mode	M
94	R0 R0	6
91	— —	3
88	R0 R1 ($P_{AA} = 0.80$)	4
85	R1 ($P_{AA} = 0.80$) R0	4
82	— R1 ($P_{AA} = 0.80$)	6
79	— R1 ($P_{AA} = 0.80$)	6
76	R1 ($P_{AA} = 0.86$) R0	6
73	— R1 ($P_{AA} = 0.86$)	6
70	— R1 ($P_{AA} = 0.92$)	6
67	— R1 ($P_{AA} = 0.86$)	6
64	— R1 ($P_{AA} = 0.96$)	7
61	— R1 ($P_{AA} = 0.96$)	7
58	R0 R0 R1 ($P_{AA} = 0.96$) R0	7
55	R0 R1 ($P_{AA} = 0.96$)	7
52	R1 ($P_{AA} = 0.85$)	6
49	R1 ($P_{AA} = 0.88$)	6
46	R1 ($P_{AA} = 0.88$) R0	6
43	R1 ($P_{AA} = 0.88$) —	7
40	R0 R0	7
37	R0 R0	7
34	R0 R0	7
31	R0 R0 R0	7
28	— R0 R0	8
25	— R0 R0	8
22	— R0 R0	8
19	— R0 R0	8
16	R0 R0	8
13	R1 ($P_{AA} = 0.75$) R0	8
10	R1 ($P_{AA} = 0.50$) R1 ($P_{AA} = 0.55$)	8
7	R1 ($P_{AA} = 0.80$)	7
4	R1 ($P_{AA} = 0.89$)	8

distribution, and from 13 %RH, a partial tendency to segregation governs the stacking mode (Table 2 and Figure 4).

3.2. Stressed Sample

3.2.1. Qualitative XRD Description

(1) Sorption Process. From a macro point of view, the hydration behavior similar to that of the unstressed sample is observed in the case of the sample having undergone 50 drying/wetting cycles. Indeed, the d_{001} basal spacing value goes from 9.86 Å at 4 %RH relative to the 0W phase to 18.47 at 94 %RH, indicating a highly hydrated specimen (3W) (Figure S3). But the difference in behavior between the two hydration samples lies in the mechanism and the path followed during the swelling process. Indeed, for the stressed sample, the absence of homogeneous hydration levels characterized by homogeneous phases at 1W and 2W is noted. The evolution of experimental XRD patterns shows a 0W–2W transition over a wide range of humidity that starts at 16 %RH and ends at 70 %RH. This behavior is not observed in the case of the unstressed sample. The second difference is the absence of a homogeneous 3W phase for the maximum used RH values and the shift of the RH range for the homogeneous 2W phase. However, the hydration evolution versus %RH can be described by three main steps: (i) a logic starting from the 0W hydration state, (ii) a transition from 0W to 2W passing through an ephemeral 1W state, and (iii) an incomplete transition from 2W to 3W for high RH rates.

The exploitation of the calculated values of FWHM and ξ, reported in Figure 5, confirms the interstratified character observed during the 0W–2W and 2W–3W transitions. Indeed, a maximum of the FWHM value and ξ parameters is obtained for two ranges of humidity, respectively, that is, from 16% to 70 %RH and from 88% to 94 %RH. The homogeneous 0W and 2W hydration phases are characterized by low values of the abovementioned two parameters.

(2) Desorption Process. The evolution of experimental XRD patterns along the desorption process is shown in Figure S4. Along the explored RH range, a transition from an interstratified 3W hydration state to an interstratified 0W phase, characterized by an asymmetric 00l reflection with irrational positions, is observed (Figure 5). The followed dehydration way differs from that adopted during the hydration process indicating the appearance of a hydration hysteresis phenomenon. Depending on the RH value, during the dehydration
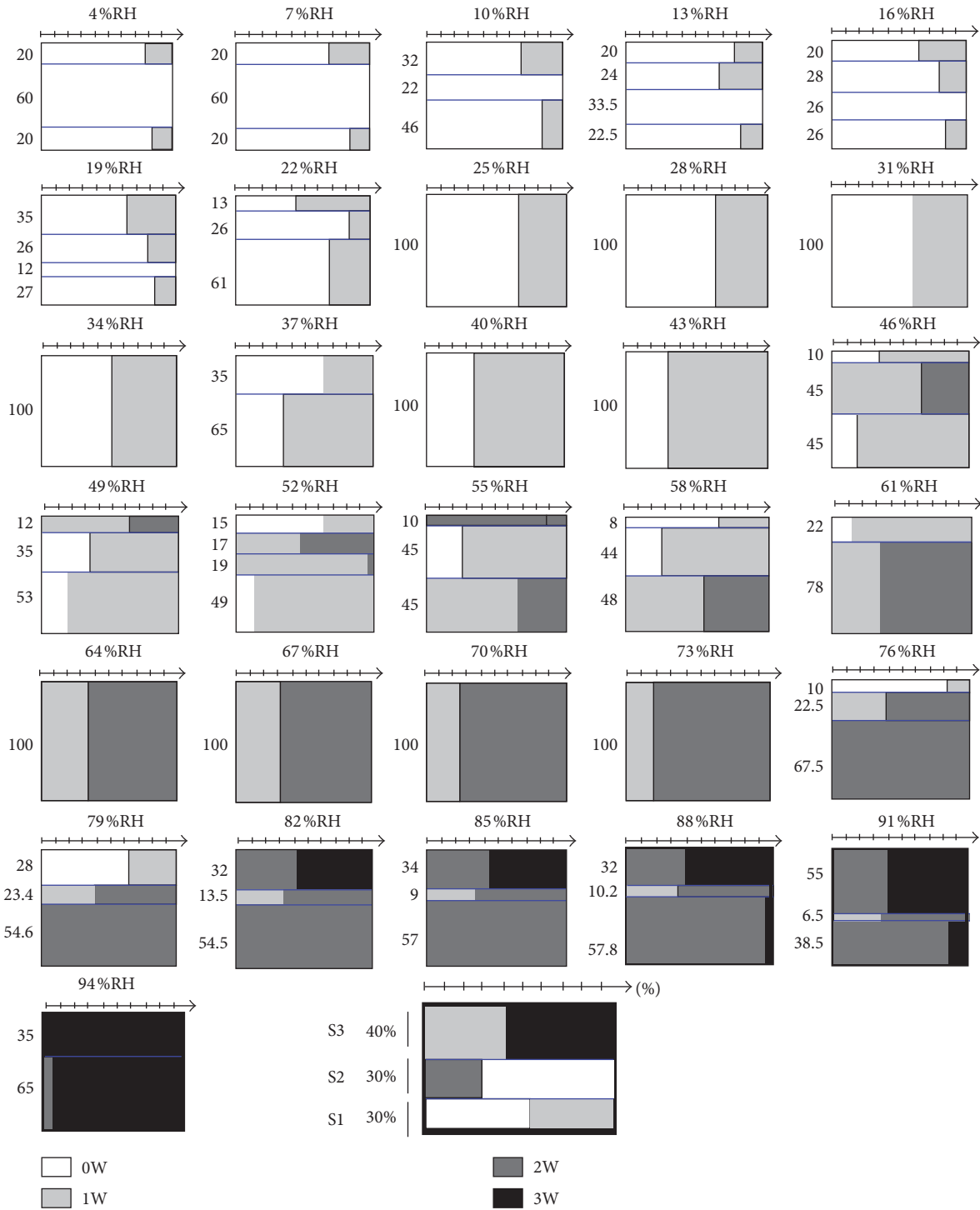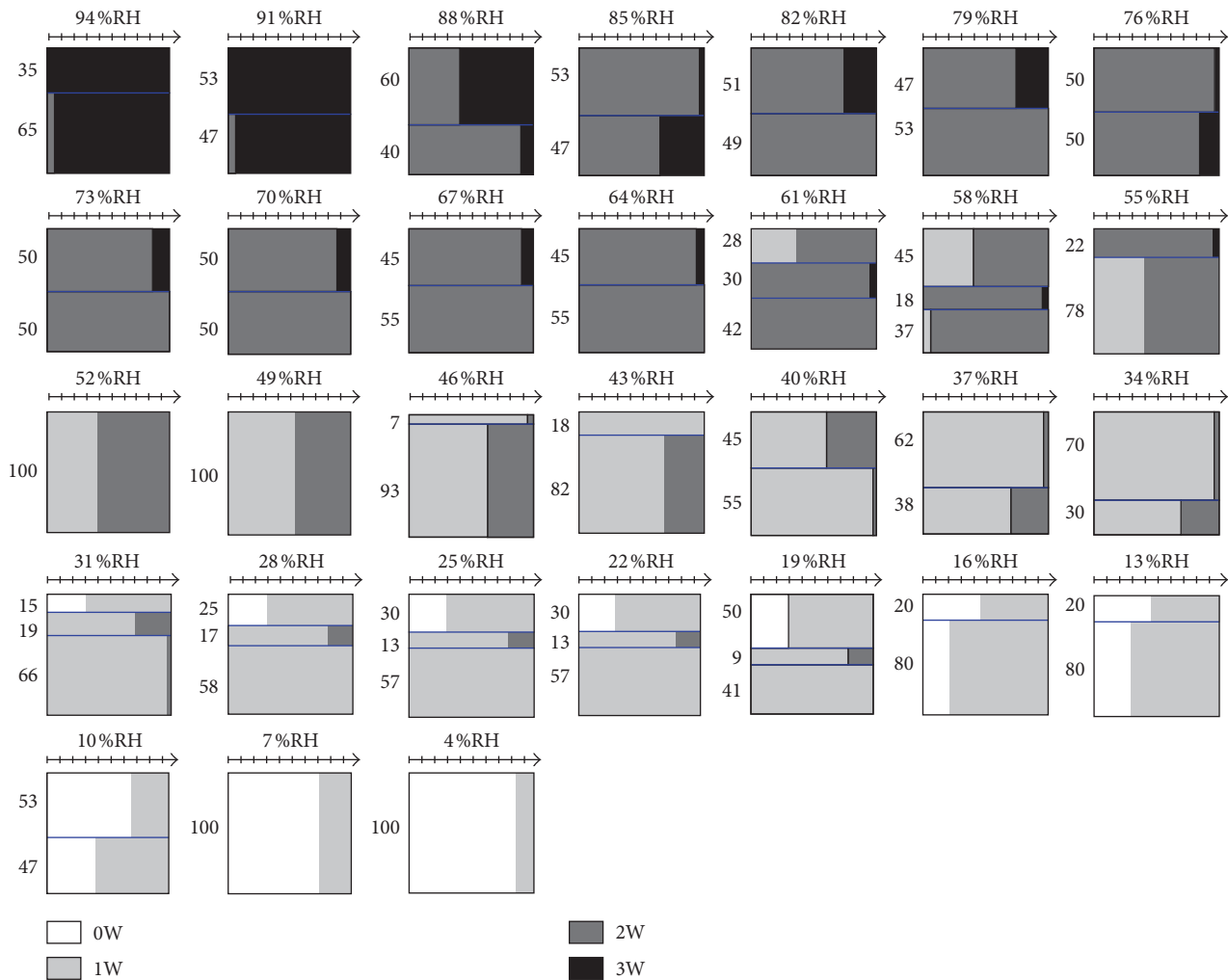
FIGURE 4: Schematic representation of the structure model used to fit the experimental XRD pattern in the case of the unstressed sample along the desorption process.

sequence, two hydration levels related, respectively, to the homogeneous phases 1W and 2W appear. The investigation of the FWHM and ξ parameters (Figure 5) allowed us to identify the interstratified type of the obtained phases during the dehydration process.

Indeed, from 91 %RH and up to 82 %RH, a fast 3W-2W transition with the absence of a purely trihydrated phase is observed. The homogeneous 2W phase begins at 79% and ends at 64 %RH. By comparing this result to that observed in the case of the "unstressed" sample, a decrease in the width of the RH range over which it is spreading is noted. This RH shift is probably attributed to an instability in the IS configuration or the easy release of the IS water molecule, due to RH value fluctuations. Indeed, from 61 %RH and up to 31 %RH, the evolution of the d_{001} basal spacing value indicates a slow progressive 2W-1W transition that can be interpreted as a small loss of interlayer water content. The 1W homogeneous state is observed over a very short RH range compared to the "unstressed" sample whose 1W level started at 31 %RH and reached 16 %RH. This result is consistent with the above, especially since a 1W-0W transition starts a bit early (from 23 %RH), which is not the case

for the unstressed sample. The evolution of the different parameters from the qualitative analysis as a function of the %RH variation is reported in Figure 5. Several differences appear between the hydration and dehydration mechanisms obtained for the "stressed" sample. Whatever be the orientation of the hydration sequence and based on the low values of FWHM and ξ, only the homogeneous 2W state exists and a short and near-homogeneity is observed for the 1W state. On the contrary, an absence of the homogeneous 3W state, obtained in the case of the unstressed sample, is noted. The hysteresis effect (Figure 5) is present during both cycles, indicating a swelling behavior depending on the environmental conditions. The observed fluctuations, in terms of %RH width, the absence of homogeneous hydration domains, and characteristic phases of extreme RH conditions (4% and 94 %RH), confirm the major interstratified character observed for the "stressed" sample during the sorption/desorption sequence.

The evolution of the two parameters FWHM and ξ made it possible to determine a limit of homogeneity and/or heterogeneity of hydration and to confirm the geometric anomalies observed on the experimental XRD profiles.

(a)

(b)

(c)
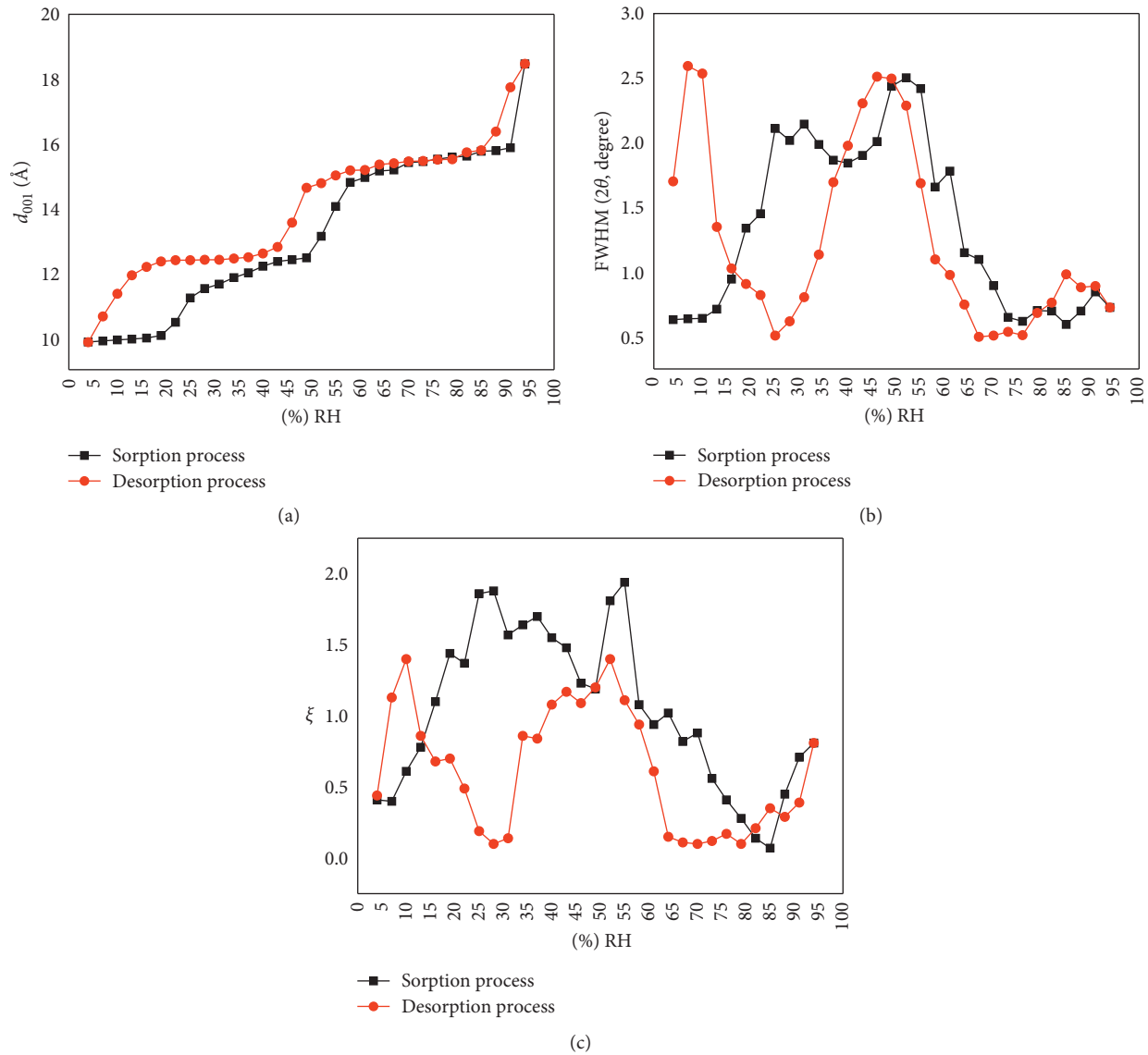
FIGURE 5: Evolution of the d_{001} (a), FWHM (b), and ξ parameters (c) versus %RH in the case of the stressed sample.

In general and for both sorption and desorption mechanisms, the "stressed" sample has more hydration heterogeneities than the "unstressed" sample. The interpretation of this result can be completed only after a quantitative analysis which makes it possible to quantify the abundances of the phases present in the structure and the contents of the IS.

3.2.2. Quantitative XRD Analysis

(1) Sorption Process. The obtained results deduced from the qualitative analysis are refined by quantitative analysis in order to quantify the composition of the clay "particle." All structural parameters used to model experimental XRD patterns are shown in Figure S3 and are summarized in Table 3 and Figure 6. Contrary to the results obtained during the qualitative analysis, concerning the homogeneous 0W and 2W hydration phases, the quantitative analysis shows

the absence of any hydration homogeneities along the sorption process. In fact, for a humidity ranging from 4% to 37 %RH, the experimental profiles are reproduced by a 0W/1W mixture with variable abundances. The investigation of junction probabilities and the succession law between layers indicates a major segregation trend (R1). Also, qualitatively, the 2W transition starts at 52 %RH, which is not really the case since the introduction of a 2W layer "population" is done quantitatively at 40 %RH and the system (i.e., crystalline particle) is totally reproduced by 3 layer types (i.e., 0W, 1W, and 2W). This configuration does not exclude the 0W phase (which is in complete disagreement with the qualitative description), the contribution of which persists in the diffracted intensity, even for very high values of humidity. The three layer types are stacked with a segregation tendency.

At 34 %RH, the decrease of the average number of layers per half unit cell is due to hydration transition domain. This

Table 3: Some structural parameters obtained from the quantitative XRD analysis in the case of the stressed sample along the sorption process.

%RH	Layer stacking mode	M
	R0	
4	—	7
	R0	
	R1 ($P_{AA} = 0.90$)	
7	—	9
	R1 ($P_{AA} = 0.80$)	
	R1 ($P_{AA} = 0.90$)	
10	—	10
	R1 ($P_{AA} = 0.80$)	
	R1 ($P_{AA} = 0.90$)	
13	—	11
	R1 ($P_{AA} = 0.80$)	
	R1 ($P_{AA} = 0.90$)	
16	—	11
	R1 ($P_{AA} = 0.80$)	
19	R0	11
	R1 ($P_{AA} = 0.90$)	
	R1 ($P_{AA} = 0.80$)	
22	R1 ($P_{AA} = 0.90$)	11
	R1 ($P_{AA} = 0.70$)	
	R1 ($P_{AA} = 0.90$)	
25	R1 ($P_{AA} = 0.70$)	10
	R1 ($P_{AA} = 0.90$)	
28	R1 ($P_{AA} = 0.70$)	8
31	R1 ($P_{AA} = 0.70$)	8
34	R1 ($P_{AA} = 0.70$)	7
37	R1 ($P_{AA} = 0.70$)	7
	R1 ($P_{AA} = 0.70$)	
40	R0	7
	R1 ($P_{AA} = 0.75$)	
	R1 ($P_{AA} = 0.70$)	
43	R0	6
	R1 ($P_{AA} = 0.70$)	
46	R1 ($P_{AA} = 0.80$)	6
	R1 ($P_{AA} = 0.70$)	
	R1 ($P_{AA} = 0.90$)	
49	R1 ($P_{AA} = 0.57$)	6
	R1 ($P_{AA} = 0.70$)	
	R1 ($P_{AA} = 0.90$)	
52	R1 ($P_{AA} = 0.57$)	6
	R1 ($P_{AA} = 0.70$)	
	R1 ($P_{AA} = 0.90$)	
55	R1 ($P_{AA} = 0.57$)	7
	R1 ($P_{AA} = 0.70$)	
	R1 ($P_{AA} = 0.90$)	
58	R1 ($P_{AA} = 0.60$)	6
	R1 ($P_{AA} = 0.85$)	
61	R1 ($P_{AA} = 0.75$)	6
	R1 ($P_{AA} = 0.65$)	
	R1 ($P_{AA} = 0.85$)	
64	R1 ($P_{AA} = 0.75$)	6
	R1 ($P_{AA} = 0.68$)	
	R1 ($P_{AA} = 0.85$)	
67	R1 ($P_{AA} = 0.75$)	6
	R1 ($P_{AA} = 0.90$)	
	R1 ($P_{AA} = 0.85$)	
70	R1 ($P_{AA} = 0.75$)	6
	R1 ($P_{AA} = 0.90$)	

Table 3: Continued.

%RH	Layer stacking mode	M
	R1 ($P_{AA} = 0.80$)	
	R1 ($P_{AA} = 0.65$)	
73	R1 ($P_{AA} = 0.92$)	6
	R1 ($P_{AA} = 0.95$)	
	—	
76	R1 ($P_{AA} = 0.92$)	6
	R1 ($P_{AA} = 0.85$)	
	R0	
79	—	6
	R1 ($P_{AA} = 0.85$)	
	R1 ($P_{AA} = 0.95$)	
82	R0	7
	R1 ($P_{AA} = 0.85$)	
	R0	
85	R0	7
	R1 ($P_{AA} = 0.85$)	
	R0	
88	R0	7
	R1 ($P_{AA} = 0.85$)	
	R1 ($P_{AA} = 0.93$)	
91	R0	6
	R0	
	R1 ($P_{AA} = 0.85$)	
94	R1 ($P_{AA} = 0.97$)	6

decrease in the M parameter is quantitatively reflected by diversity and a maximum number of MLSs present in the proposed theoretical model. The elevated heterogeneity degree is confirmed from 61 %RH, where the experimental profile is totally reproduced by 4 theoretical distributions (0W, 1W, 2W, and 3W). This combination of "population" is up to 76 %RH.

This result is probably due to a hard exfoliation mechanism of the IS under the effect of the constraint created by the drying/wetting stress.

From 79 %RH and up to 91 %RH, the 0W phase disappears and the system is reproduced by 3 phases only. At 94 %RH, the 1W phase disappears and the homogeneous 3W hydration state is never reached; however, the experimental profile is reproduced by a distribution between two phases (2W and 3W) stacked with a segregation tendency.

Physically, the existence of these hydration heterogeneities, in the quantitative analysis, agrees with the results of the qualitative analysis, indicating an increase in the values of FWHM and ξ on the same humidity range.

(2) Desorption Process. All structural parameters resulting from the quantitative analysis are summarized in Table 4 and Figure 7. In addition to the absence of the homogeneous hydration state over the entire explored RH range and contrary to the results of the qualitative analysis, the water molecule release is done in a progressive and continuous manner in the absence of any specific level. Indeed, from 94% up to 73 %RH, the experimental profiles are reproduced based on an arrangement of 2W and 3W phases stacked with a segregation tendency in the majority of cases. This result

Figure 6: Schematic representation of the MLS used to fit the experimental XRD pattern in the case of the stressed sample along the sorption process.

contradicts with the qualitative analysis which assumes a homogeneous 2W phase starting at 79 %RH and ending at 64 %RH. From 70 %RH, the 1W phase is introduced in the MLS, and up to 52 %RH, the structure is fully reproduced by three layer types. At 49 %RH, the transition 3W-2W is achieved and a disappearance of the 3W phase is noted. The system is modeled using random distribution of 1W and 2W

phases up to 46 %RH. The 0W phase is introduced, with minor proportions, in the MLS from 43 %RH and continues its progression in terms of abundance up to 4 %RH. At 25 %RH, the total disappearance of the 2W phase indicates the end of the 2W-1W transition.

The proposed MLS raises the ambiguity of the 3W-2W, 2W-1W, and 1W-0W transition zone limits, observed

TABLE 4: Some structural parameters obtained from the quantitative XRD analysis in the case of the stressed sample along the desorption process.

%RH	Layer stacking mode	M
94	R1 ($P_{AA} = 0.86$) R1 ($P_{AA} = 0.90$)	6
91	R1 ($P_{AA} = 0.90$) R1 ($P_{AA} = 0.90$)	6
88	R1 ($P_{AA} = 0.75$) R1 ($P_{AA} = 0.90$)	5
85	R0 R1 ($P_{AA} = 0.86$)	5
82	R0 R1 ($P_{AA} = 0.86$)	5
79	— R1 ($P_{AA} = 0.75$)	5
76	— R1 ($P_{AA} = 0.75$)	5
73	— R1 ($P_{AA} = 0.75$)	5
70	R0 R1 ($P_{AA} = 0.75$)	5
67	R0 R1 ($P_{AA} = 0.75$)	5
64	R0 R0 R1 ($P_{AA} = 0.75$)	5
61	R0 R0 R1 ($P_{AA} = 0.75$)	5
58	R1 ($P_{AA} = 0.95$) R1 ($P_{AA} = 0.90$) R1 ($P_{AA} = 0.75$)	5
55	R1 ($P_{AA} = 0.95$) R1 ($P_{AA} = 0.90$) R1 ($P_{AA} = 0.75$)	5
52	R1 ($P_{AA} = 0.75$) R0 R1 ($P_{AA} = 0.75$)	5
49	R1 ($P_{AA} = 0.75$) —	5
46	R1 ($P_{AA} = 0.70$) —	5
43	R1 ($P_{AA} = 0.75$) R1 ($P_{AA} = 0.92$)	5
40	R1 ($P_{AA} = 0.75$) R1 ($P_{AA} = 0.92$)	6
37	R1 ($P_{AA} = 0.75$) R1 ($P_{AA} = 0.90$)	5
34	R1 ($P_{AA} = 0.75$) R1 ($P_{AA} = 0.90$)	5
31	R1 ($P_{AA} = 0.87$) R1 ($P_{AA} = 0.90$)	5
28	R1 ($P_{AA} = 0.87$) R0	5
25	R1 ($P_{AA} = 0.79$) R1 ($P_{AA} = 0.90$)	5
22	R1 ($P_{AA} = 0.79$) R1 ($P_{AA} = 0.90$)	6
19	R1 ($P_{AA} = 0.79$) R1 ($P_{AA} = 0.85$)	6
16	R1 ($P_{AA} = 0.90$) R1 ($P_{AA} = 0.87$)	6

TABLE 4: Continued.

%RH	Layer stacking mode	M
13	R1 ($P_{AA} = 0.95$) R1 ($P_{AA} = 0.87$)	5
10	R0 —	5
7	R0 R1 ($P_{AA} = 0.55$) —	7
4	R0 ($P_{AA} = 0.75$) — R1 ($P_{AA} = 0.75$)	7

during the qualitative analysis, and precisely determines the boundaries of these transitions, despite the existing overlaps. Indeed, transition zones are characterized by asymmetry in the shape of characteristic reflections and irrational positions, and modeling has allowed a more in-depth description of hydration heterogeneities linked to these zones. The absence of a clean transition zone has been shown whatever being the RH value.

During the desorption process, the 2W phase persists up to 25 %RH, and the 1W phase endures even at 4 %RH, indicating probably the hard water molecule release mechanism for the "stressed" sample. This behavior results from the effect of the applied constraint.

4. Discussion

4.1. Water Molecule Distribution and IS Configuration. During the sorption/desorption cycle, the correlation of the results from the qualitative and quantitative XRD analyses allowed us to quantify, with precision, the composition of the clay particle studied and the contents of the IS of each type of layer. The observed fluctuations of the d_{001} basal spacing as a function of %RH are related to the variation of the water molecule amounts present in the IS.

The coexistence of different hydration states, which is an omnipresent character regardless of the constraint, is probably due to a complex insertion/release water molecule mechanism. This process remains unexplored with conventional analysis methods. The results, obtained from XRD modeling, can provide answers on the evolution of the interlamellar water abundances and their organization inducing an adequate description of the evolution of the layer thickness, according to the variation of the surrounding humidity. The evolution of the theoretical water molecules (n_{H_2O}) abundance (Figure 8), resulting from the different layer-type populations versus %RH, for the unstressed and stressed samples takes the form of a hydration hysteresis. This behavior is consistent with the results obtained by Oueslati et al. [30], who demonstrate the hysteresis material response, after external solicitation. The obtained hysteresis can be divided into three main sections, respectively, I, II, and III, as a function of the value of %RH. In fact, section I starts at 4 %RH and finishes at 37 %RH, section II is spread over the 40%–82 %RH range, and finally, section III starts at 85 %RH and ends at 94 %RH.
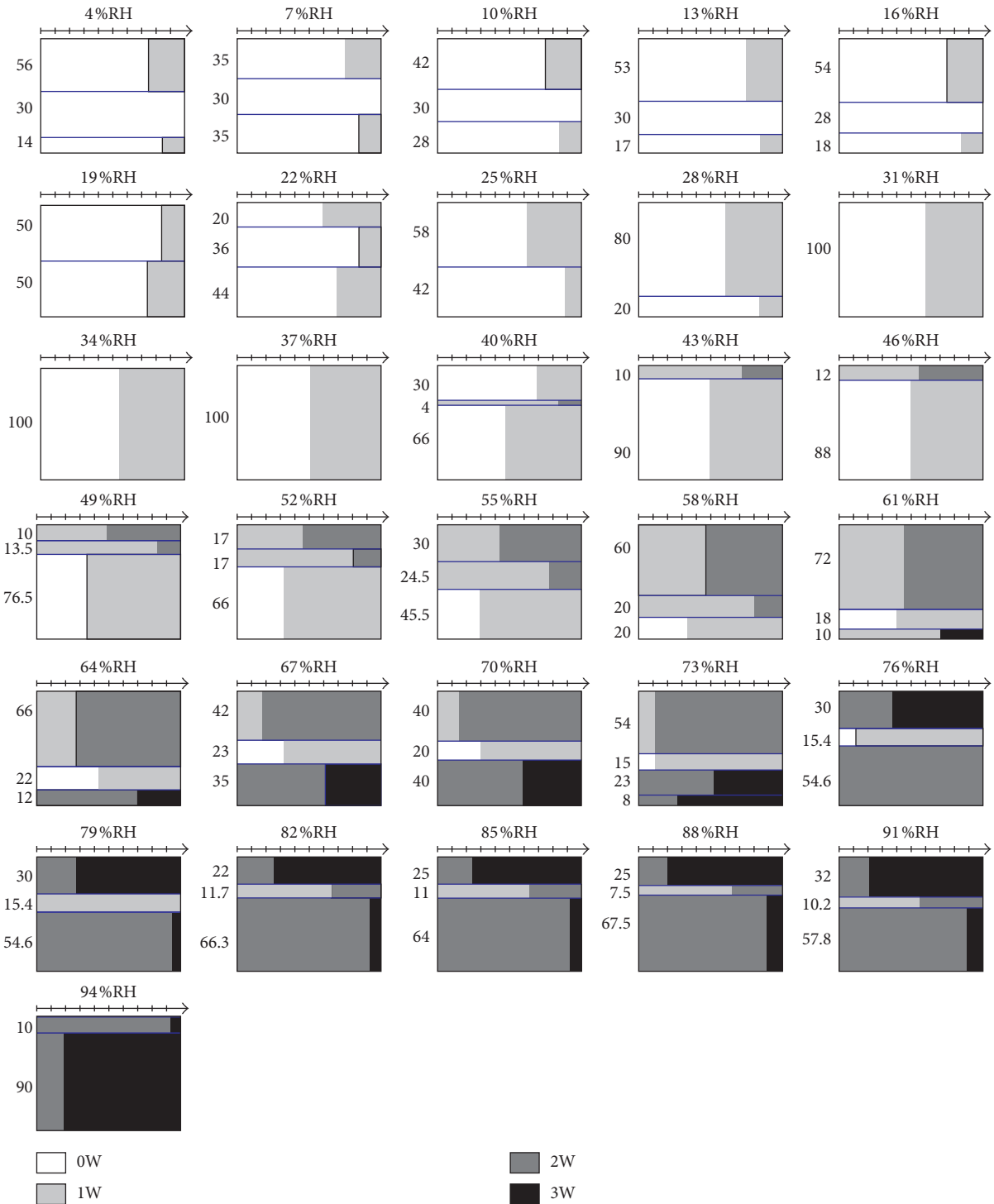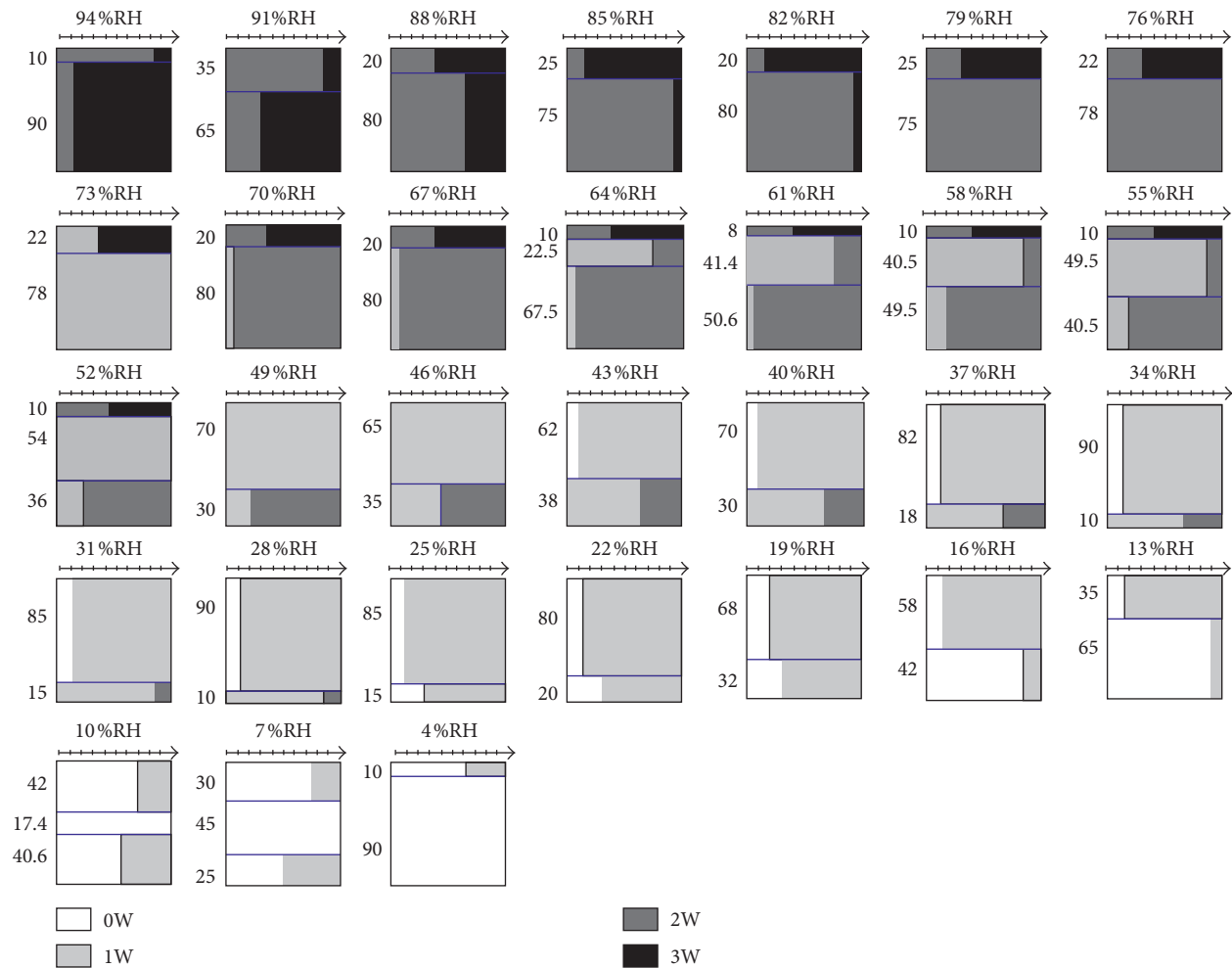
FIGURE 7: Schematic representation of the MLS used to fit the experimental XRD pattern in the case of the stressed sample along the desorption process.

4.1.1. Section I. For the low %RH value and until 37 %RH, a same evolution of the water molecule amount, for the unstressed and stressed samples, is noted and the variation of the environmental constraint (i.e., 50 drying/wetting cycles) does not affect the water retention mechanism. Quantitatively, this domain is totally described, at maximum, by 1W phases which are characterized by a relatively small layer thickness and a quite limited interlayer water amount. This condition imposes a restricted geometrical configuration of the IS (exchangeable cation + one water sheet) inducing a minimum freedom degree.

4.1.2. Section II. Within this section, there is a maximum water amount fluctuation and the sample has a high sensitivity to the applied atmospheric stress. Indeed, the decrease in the hysteresis thickness, for the stressed sample, indicates a significant variation in the water loss process as a function of %RH during the desorption sequence. This section can be divided in two specific phases, mentioned, respectively, (1) and (2), in blue in Figure 8. The difference between the two phases appears essentially on the curves relating to the desorption sequence.

For the phase (1), the starting sample is characterized by a hydration level with an average of $n_{H_2O} > 6$, whereas the stressed sample has a pseudolevel at $n_{H_2O} = 5.2$. In addition, the bearing relative to the starting sample is spread over a wide humidity range from 82 %RH to 55 %RH (~27%), which is not the case for the stressed sample with a fairly narrow range from 82 %RH to 67 %RH (~15%).

For the phase (2), there is a gradual and continuous decay for both samples but still keeping the offset in the number of water molecules. This behavior can be interpreted by the hypothesis of the transformation of a fraction of the "free" IS water into "structural" water, under the effect of the drying/wetting constraint, inducing a reduction in the number of vacant sites on the internal surfaces of the tetrahedral sheet and necessarily a decrease in the number of inserted water molecules. At the macroscopic scale, this means that, in the case of the "unstressed" sample, a water retention capacity is higher than that of the "stressed" one.

4.1.3. Section III. From 85% towards 94 %RH, a maximum water molecule abundance is reached and the same hydration/dehydration way is observed for the two studied
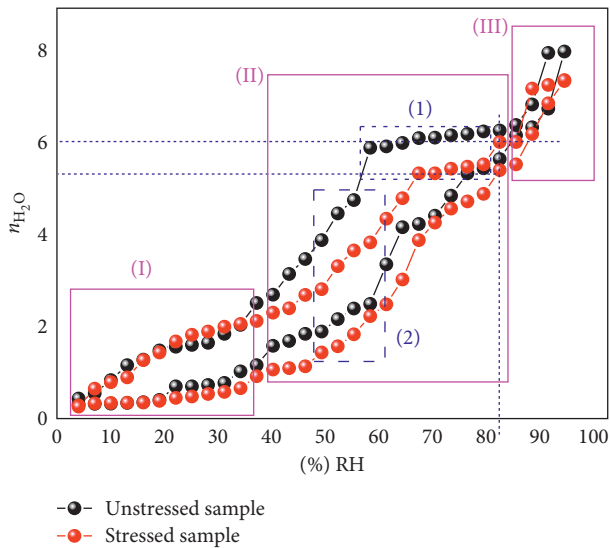
FIGURE 8: Evolution of the water molecule amounts (n_{H_2O}) versus %RH. The bottom black curve represents the sorption process of the unstressed sample. The red curve at the bottom represents the sorption process of the stressed sample. For (1) and (2) in blue, see text.

samples. This can be explained by the same principle as for Section I. Indeed, at the 3W layers hydration state, the interlamellar space is completely saturated by the geometric arrangement of the water sheets and the exchangeable cations. The stereographic configuration and the condition imposed by the physical interactions that govern the nature and arrangement of the chemical species present a constraint which limits the hydration behavior changes despite the external applied atmospheric constraint.

4.2. Hydration State Discretization. The ability of smectites to incorporate interlayer H_2O molecules and the subsequent change in d_{001} have been studied for several decades. These observations suggested several possible models where crystalline swelling is controlled by the balance between the repulsive force owing to 2 : 1 layer interactions and the attractive forces between hydrated interlayer cations and the negatively charged surface of siloxane layers [43–46]. Few studies have taken into account the coexistence of different hydration states using the XRD profile modeling approach (with 0 to 3 planes of interlayer H_2O molecules) [47–50]. More recently, the studies [51, 52] refined this approach by fitting the 00*l* reflections over a large angular range and showed that randomly interstratified structures, each containing different layer types, coexisted in their montmorillonite samples. Ferrage et al. [24] investigate the distribution of interlayer water in bihydrated smectite from X-ray diffraction profile modeling of 00*l* reflections where they propose a new configuration for the interlayer structure of bihydrated smectite. They focused on the montmorillonite hydration properties by modeling experimental X-ray diffraction patterns recorded under controlled relative humidity (RH) conditions. Indeed, the humidity rate varies with an increment of ~20%, and it is an understandable view that the purpose of the work was to

study the hydration heterogeneities in the case of several exchangeable cations. They show the systematic coexistence of smectite layer types exhibiting contrasting hydration states and a heterogeneous character for smectite hydration. This heterogeneity is characterized qualitatively using the fluctuation of FWHM and (ξ) parameters. This rule is used after that in [29, 30] to define hydration heterogeneities. Several rules deduced from the work of [25] are respected in this paper, and some results related to structural parameters such as position and amounts of exchangeable cations and the use of the MLS are in perfect concordance.

This work focuses on the discretization of the water retention mechanism, using the XRD profile modeling approach, when an external hydrous strain is applied in the case of Na-montmorillonite. The choice of the external environmental constraint (i.e., 50 drying/wetting cycles), the relative humidity variation steps (~3 %RH), and the realized limit of the extreme conditions (i.e., from 4 %RH to 94 %RH) make this work a fundamental study in order to understand the interlamellar water amount fluctuation. Indeed, the localization of the hydration transition region is accurately defined, and the hydration heterogeneities, related to the presence of more than one layer type, can be quantitatively explained. Among the strong keys of this work is the overall characterization of the abundance limits, of the dehydrated phases (0W) and the extremely hydrated phases (3W), along the sorption/desorption sequence. Indeed, after 50 drying/wetting cycles, the dehydrated and the extremely hydrated phases are more present in the stressed sample than the host material (Figure 9).

This configuration is probably due to a chemical and electrostatic equilibrium change in the interlamellar space. This change is explained by a possible adjust in the internal surface of the interlayer space following sorption/desorption cycles. Subsequent to the excessive repetition of the insertion/release water process in the starting materials, a water molecule residue has been incorporated in the internal structure which subsequently reduces the vacant site proportion inside the interlamellar space and affects its initial "function" after that (i.e., the cation exchange capacity (CEC)). By examining the evolution of the 1W and 2W abundances (Figure 9) versus %RH, a similar variation is observed for the stressed and the unstressed samples.

It remains to note that the 1W phase never reached the maximum abundance in the case of the stressed and unstressed samples. However, the 1W phase is the layer type mostly present along all the relative humidity scales. This result is interpreted by the transitional character of the 1W hydration state explained by a structural interlamellar space change with a permanent presence of the interlamellar water molecules regardless of %RH rates. The 1W phase can be considered as a transitional hydration state support. In terms of heterogeneities, a trend towards homogeneity is noted for both hysteresis terminals, whereas a heterogeneity tendency is noted for the transitional areas.

5. Conclusion

The XRD profile modeling of the 00*l* reflections allowed us to characterize the structural changes along the c^* axis of the
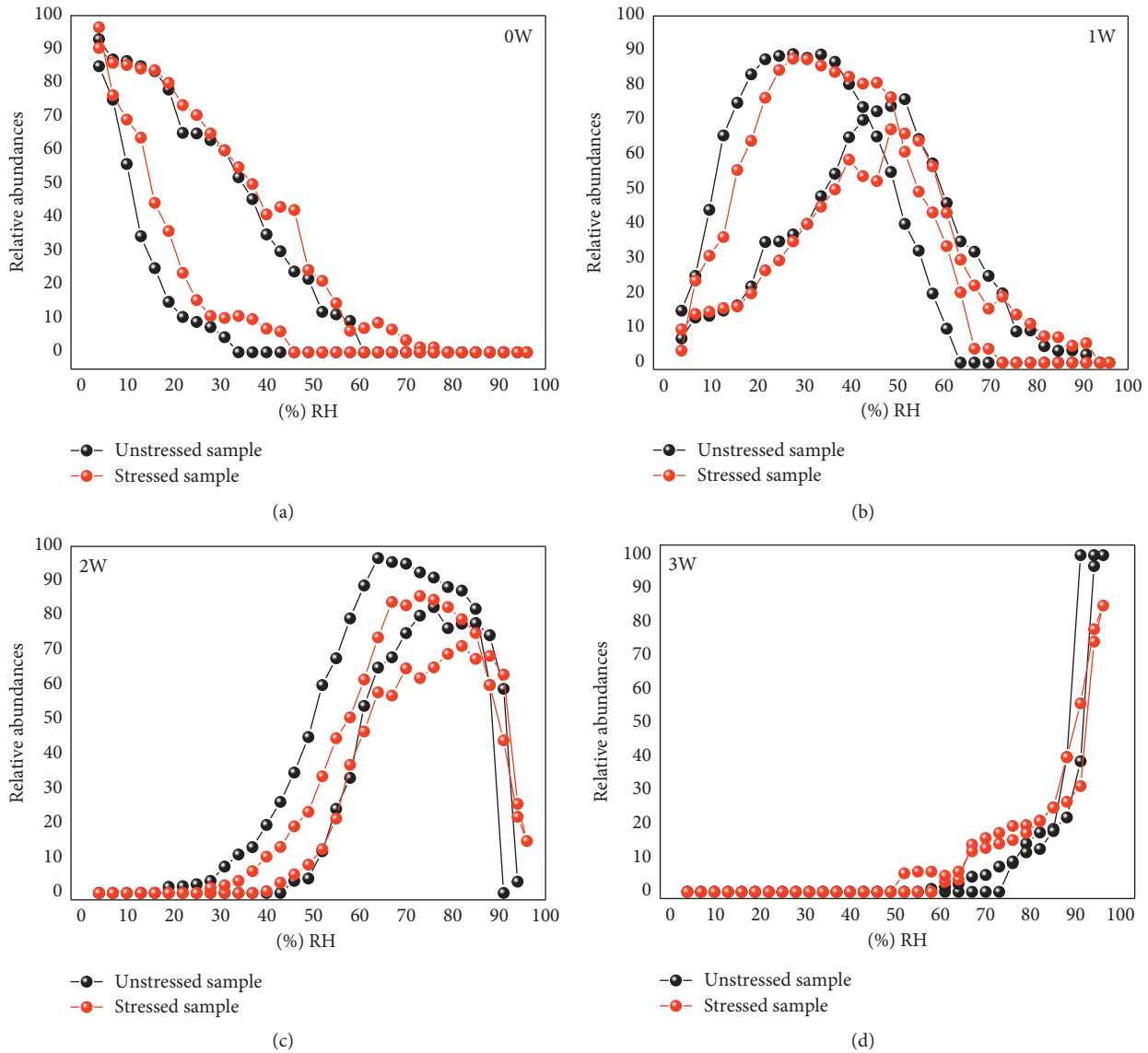
(a)

(b)

(c)

(d)

FIGURE 9: Evolution of the individual relative abundance of each hydration state as a function of the relative humidity (%RH) in the case of unstressed and stressed samples.

SWy-2-Na sample before and after application of the atmospheric stress. The obtained results are as follows:

(i) A new hydration behavior of the "stressed" sample described by fluctuations in the hydration hysteresis as a function of the RH rates.

(ii) The application of the sorption/desorption process by "in situ" variation of the %RH, before and after applying the constraint, made it possible to identify the homogeneous hydration states and the hydration transition zones, which are characterized by a high heterogeneity degree.

(iii) Structural heterogeneities are characterized by an elevated MLS number. Indeed, two possible configurations of IS contents, 0W/1W/2W and 1W/2W/3W, with variable relative abundances, are discerned over a wide explored RH range.

(iv) Iteration of the insertion/release phenomenon of the water molecules, during drying/wetting cycles, induces an increase in the relative abundance of the 0W and 3W population at the expense of the abundances of the 1W and 2W phases. This result explains the limits observed during the sorption/desorption process in the case of the stressed sample.

Conflicts of Interest

The authors declare that they have no conflicts of interest.

Acknowledgments

presentation. The authors also thank Nathaniel Findling (ISTerre, Grenoble, France) for the assistance during XRD and sorption/desorption data collection.

Supplementary Materials

Figure S1: best agreement obtained between experimental (black) and modeled (red) XRD patterns in the case of the SWy-2-Na sample versus %RH. The sorption sequence by increasing %RH: 4–25 %RH (a), 28–49 %RH (b), 52–73 %RH (c), and 76–94 %RH (d). For all XRD patterns, the intensity is arbitrary. The theoretical decomposition of the experimental patterns (blue, red, and green) is on the left. The obtained best agreement is on the right. For each %RH value, the 001 line is recorded twice (in black) in order to check the sample balance with its environment. *Halite (NaCl) complex. Figure S2: best agreement obtained between experimental (black) and modeled (red) XRD patterns in the case of the SWy-2-Na sample versus %RH. The desorption sequence by decreasing %RH: 94–70 %RH (a), 67–46 %RH (b), 43–25 %RH (c), and 22–4 %RH (d). For all XRD patterns, the intensity is arbitrary. The theoretical decomposition of the experimental patterns (blue, red, and green) is on the left. The final best agreement is on the right. *Halite (NaCl) complex. Figure S3: best agreement obtained between experimental (black) and modeled (red) XRD patterns in the case of the stressed sample versus %RH. The sorption sequence obtained by increasing %RH: 4–25 %RH (a), 28–46 %RH (b), 49–70 %RH (c), and 73–94 %RH (d). For all XRD patterns, the intensity is arbitrary. The theoretical decomposition of the experimental patterns (blue, red, and green) is on the left. The obtained best agreement is on the right. *Halite (NaCl) complex. Figure S4: best agreement obtained between experimental (black) and modeled (red) XRD patterns in the case of the stressed sample versus %RH. The desorption sequence obtained by increasing %RH: 4–25 %RH (a), 28–46 %RH (b), 49–70 %RH (c), and 73–94 %RH (d). For all XRD patterns, the intensity is arbitrary. The theoretical decomposition of the experimental patterns (blue, red, and green) is on the left. The obtained best agreement is on the right. *Halite (NaCl) complex. (*Supplementary Materials*)

References

[1] H.-J. Herbert, J. Kasbohm, H. Sprenger, A. M. Fernández, and C. Reichelt, "Swelling pressures of MX-80 bentonite in solutions of different ionic strength," *Physics and Chemistry of the Earth, Parts A/B/C*, vol. 33, no. S1, pp. S327–S342, 2008.

[2] T. Higashihara, K. Kinoshita, Y. Akagi, S. Sato, and T. Kozaki, "Transport number of sodium ions in water-saturated, compacted Na-montmorillonite," *Physics and Chemistry of the Earth, Parts A/B/C*, vol. 33, no. S1, pp. S142–S148, 2008.

[3] M. V. Villara, M. Sánchez, and A. Gens, "Behaviour of a bentonite barrier in the laboratory: experimental results up to 8 years and numerical simulation," *Physics and Chemistry of the Earth, Parts A/B/C*, vol. 33, no. S1, pp. S476–S485, 2008.

[4] T. Kozaki, J. Liua, and S. Sato, "Diffusion mechanism of sodium ions in compacted montmorillonite under different NaCl concentration," *Physics and Chemistry of the Earth, Parts A/B/C*, vol. 33, no. 14–16, pp. 957–961, 2008.

[5] T. Kozaki, T. Sawaguchi, A. Fujishima, and S. Sato, "Effect of exchangeable cations on apparent diffusion of Ca2+ ions in Na- and Ca-montmorillonite mixtures," *Physics and Chemistry of the Earth, Parts A/B/C*, vol. 35, no. 6–8, pp. 254–258, 2010.

[6] O. Karnland, M. Birgersson, and M. Hedström, "Selectivity coefficient for Ca/Na ion exchange in highly compacted bentonite," *Physics and Chemistry of the Earth, Parts A/B/C*, vol. 36, no. 17–18, pp. 1554–1558, 2011.

[7] K. K. Norrfors, M. Bouby, S. Heck et al., "Montmorillonite colloids: I. Characterization and stability of dispersions with different size fractions," *Applied Clay Science*, vol. 114, pp. 179–189, 2015.

[8] W. F. Bradley, R. E. Grim, and G. F. Clark, "A study of the behavior of montmorillonite on wetting," *Zeitschrift Kristallographie*, vol. 97, pp. 260–270, 1937.

[9] J. Méring and R. Glaeser, "Sur le rôle de la valence des cations échangeables dans la montmorillonite," *Bulletin de la Société Francaise de Minéralogie et Cristallographie*, vol. 77, pp. 519–530, 1954.

[10] S. Dultz, J.-H. An, and B. Riebe, "Organic cation exchanged montmorillonite and vermiculite as adsorbents for Cr(VI): effect of layer charge on adsorption properties," *Applied Clay Science*, vol. 67-68, pp. 125–133, 2012.

[11] D. M. Moore and R. C. Reynolds Jr., *X-Ray Diffraction and the Identification and Analysis of Clay Minerals*, Oxford University Press, New York, NY, USA, 1997.

[12] B. Dazas, B. Lanson, J. Breu, J.-L. Robert, M. Pelletier, and E. Ferrage, "Smectite fluorination and its impact on interlayer water content and structure: a way to fine tune the hydrophilicity of clay surfaces?," *Microporous and Mesoporous Materials*, vol. 181, pp. 233–247, 2013.

[13] A. Kaya and H. Y. Fang, "The effects of organic fluids on physicochemical parameters of fine-grained soils," *Canadian Geotechnical Journal*, vol. 37, no. 5, pp. 943–950, 2000.

[14] M. H. Fu, Z. Z. Zhang, and P. F. Low, "Changes in the properties of a montmorillonite-water system during the adsorption and desorption of water: hysteresis," *Clays and Clay Minerals*, vol. 38, pp. 485–492, 1990.

[15] E. S. Boek, P. V. Coveney, and N. T. Skipper, "Monte Carlo molecular modeling studies of hydrated Li-, Na-, and K-smectites: understanding the role of potassium as a clay swelling inhibitor," *Journal of the American Chemical Society*, vol. 117, no. 50, pp. 12608–12617, 1995.

[16] E. S. Boek, P. V. Coveney, and N. T. Skipper, "Molecular modeling of clay hydration: a study of hysteresis loops in the swelling curves of sodium montmorillonites," *Langmuir*, vol. 11, no. 12, pp. 4629–4631, 1995.

[17] F.-R. C. Chang, N. T. Skipper, and G. Sposito, "Computer simulation of interlayer molecular structure in sodium montmorillonite hydrates," *Langmuir*, vol. 11, no. 7, pp. 2734–2741, 1995.

[18] F.-R. C. Chang, N. T. Skipper, and G. Sposito, "Monte Carlo and molecular dynamics simulations of interfacial structure in lithium-montmorillonite hydrates," *Langmuir*, vol. 13, no. 7, pp. 2074–2082, 1997.

[19] N. T. Skipper, F. R. C. Chang, and G. Sposito, "Monte Carlo simulation of interlayer molecular structure in swelling clay minerals. 1. Methodology," *Clays and Clay Minerals*, vol. 43, no. 3, pp. 285–293, 1995.

[20] S. Karaborni, B. Smit, W. Heidug, J. Urai, and E. van Oort, "The swelling of clays: molecular simulations of the hydration of montmorillonite," *Science*, vol. 271, no. 5252, pp. 1102–1104, 1996.

[21] Q. H. Zeng, A. B. Yu, G. Q. Lu, and R. K. Standish, "Molecular dynamics simulation of the structural and dynamic properties of dioctadecyldimethyl ammoniums in organoclays," *Journal of Physical Chemistry B*, vol. 108, no. 28, pp. 10025–10033, 2004.

[22] A. Meleshyn and C. Bunnenberg, "Swelling of Na/Mg-montmorillonites and hydration of interlayer cations: a Monte Carlo study," *Journal of Chemical Physics*, vol. 123, no. 7, article 074706, 2005.

[23] D. E. Smith, Y. Wang, A. Chaturvedi, and H. D. Whitley, "Molecular simulations of the pressure, temperature, and chemical potential dependencies of clay swelling," *Journal of Physical Chemistry B*, vol. 110, no. 40, pp. 20046–20054, 2006.

[24] E. Ferrage, B. Lanson, B. A. Sakharov, and V. A. Drits, "Investigation of smectite hydration properties by modeling of X-ray diffraction profiles. Part 1. Montmorillonite hydration properties," *American Mineralogist*, vol. 90, no. 8-9, pp. 1358–1374, 2005.

[25] E. Ferrage, B. Lanson, N. Malikova, A. Plançon, B. A. Sakharov, and V. A. Drits, "New insights on the distribution of interlayer H_2O molecules in bi-hydrated smectite from X-ray diffraction profile modeling of 00l reflections," *Chemistry of Materials*, vol. 17, no. 13, pp. 3499–3512, 2005.

[26] E. Ferrage, B. Lanson, B. A. Sakharov, N. Geoffroy, E. Jacquot, and V. A. Drits, "Investigation of smectite hydration properties by modeling of X-ray diffraction profiles. Part 2. Influence of layer charge and charge location," *American Mineralogist*, vol. 92, no. 10, pp. 1731–1743, 2007.

[27] W. Oueslati, M. S. Karmous, H. Ben Rhaiem, B. Lanson, and A. Ben Haj Amara, "Effect of interlayer cation and relative humidity on the hydration properties of a dioctahedral smectite," *Zeitschrift für Kristallographie Supplements*, vol. S26, pp. 417–422, 2007.

[28] W. Oueslati, H. B. Rhaiem, B. Lanson, and A. B. H. Amara, "Selectivity of Na–montmorillonite in relation with the concentration of bivalent cation (Cu^{2+}, Ca^{2+}, Ni^{2+}) by quantitative analysis of XRD patterns," *Applied Clay Science*, vol. 43, no. 2, pp. 224–227, 2009.

[29] W. Oueslati, H. Ben Rhaiem, and A. Ben Haj Amara, "XRD investigations of hydrated homoionic montmorillonite saturated by several heavy metal cations," *Desalination*, vol. 271, no. 1–3, pp. 139–149, 2011.

[30] W. Oueslati, H. Ben Rhaiem, and A. Ben Haj Amara, "Effect of relative humidity constraint on the metal exchanged montmorillonite performance: an XRD profile modeling approach," *Applied Surface Science*, vol. 261, pp. 396–404, 2012.

[31] B. Dazas, E. Ferrage, A. Delville, and B. Lanson, "Interlayer structure model of tri-hydrated low-charge smectite by X-ray diffraction and Monte Carlo modeling in the Grand Canonical ensemble," *American Mineralogist*, vol. 99, no. 8-9, pp. 1724–1735, 2014.

[32] T. Sato, T. Watanabe, and R. Otsuka, "Effects of layer charge, charge location, and energy change on expansion properties of dioctahedral smectites," *Clays and Clay Minerals*, vol. 40, no. 1, pp. 103–113, 1992.

[33] W. Oueslati, M. Ammar, and N. Chorfi, "Quantitative XRD analysis of the structural changes of Ba-exchanged montmorillonite: effect of an in situ hydrous perturbation," *Minerals*, vol. 5, no. 3, pp. 507–526, 2015.

[34] W. F. Moll, "Baseline studies of the Clay Minerals Society Source Clays: geological origin," *Clays and Clay Minerals*, vol. 49, no. 5, pp. 374–380, 2001.

[35] A. R. Mermut and A. F. Cano, "Baseline studies of the Clay Minerals Society Source Clays: chemical analyses of major elements," *Clays and Clay Minerals*, vol. 49, no. 5, pp. 381–386, 2001.

[36] J. L. Post, B. L. Cupp, and F. T. Madsen, "Beidellite and associated clays from the DeLamar Mine and Florida Mountain area, Idaho," *Clays and Clay Minerals*, vol. 45, no. 2, pp. 240–250, 1997.

[37] D. Tessier, "Experimental study of the clay materials organization. Hydration, swelling and structure along drying and re-wetting," Thesis, University of Paris VII, Publication INRA Versailles, Paris, France, 1984.

[38] S. W. Bailey, "Nomenclature for regular interstratifications," *American Mineralogist*, vol. 67, pp. 394–398, 1982.

[39] M. Ammar, W. Oueslati, H. B. Rhaiem, and A. B. H. Amara, "Quantitative XRD analysis of the dehydration–hydration performance of (Na^+, Cs^+) exchanged smectite," *Desalination and Water Treatment*, vol. 52, no. 22–24, pp. 4314–4333, 2014.

[40] M. Ammar, W. Oueslati, H. B. Rhaiem, and A. B. H. Amara, "Effect of the hydration sequence orientation on the structural properties of Hg exchanged montmorillonite: quantitative XRD analysis," *Journal of Environmental Chemical Engineering*, vol. 2, no. 3, pp. 1604–1611, 2014.

[41] V. A. Drits and C. Tchoubar, *X-ray Diffraction by Disordered Lamellar Structures: Theory and Applications to Microdivided Silicates and Carbons*, Springer, Berlin, Germany, 1990.

[42] B. A. Sakharov and B. Lanson, "X-ray identification of mixed-layer structures. Modelling of diffraction effects," in *Handbook of Clay Science*, F. Bergaya and G. Lagaly, Eds., vol. 5B, pp. 51–135, Elsevier, Amsterdam, Netherlands, 2013.

[43] K. Norrish, "The swelling of montmorillonite," *Discussions of the Faraday Society*, vol. 18, pp. 120–133, 1954.

[44] H. van Olphen, "Thermodynamics of interlayer adsorption of water in clays," *Journal of Colloid Science*, vol. 20, no. 8, pp. 822–837, 1965.

[45] D. A. Laird, "Influence of layer charge on swelling of smectites," *Applied Clay Science*, vol. 34, no. 1–4, pp. 74–87, 2006.

[46] B. Lanson, "Modelling of X-ray diffraction profiles: investigation of defective lamellar structure crystal chemistry," *EMU Notes in Mineralogy*, Chapter 4, vol. 11, pp. 151–202, Mineralogical Society Great Britain & Ireland, Ireland, 2011.

[47] T. Iwasaki and T. Watanabe, "Distribution of Ca and Na ions in dioctahedral smectites and interstratified dioctahedral mica/smectites," *Clays and Clay Minerals*, vol. 36, no. 1, pp. 73–82, 1988.

[48] I. Bérend, J. M. Cases, M. François et al., "Mechanism of adsorption and desorption of water vapour by homoionic montmorillonites: 2. The Li^+, Na^+, K^+, Rb^+ and Cs^+ exchanged forms," *Clays and Clay Minerals*, vol. 43, no. 3, pp. 324–336, 1995.

[49] J. M. Cases, I. Bérend, M. François, J. P. Uriot, L. J. Michot, and F. Thomas, "Mechanism of adsorption and desorption of water vapour by homoionic montmorillonite: The Mg^{2+}, Ca^{2+}, Sr^{2+} and Ba^{2+} exchanged forms," *Clays and Clay Minerals*, vol. 45, no. 1, pp. 8–22, 1997.

[50] J. Cuadros, "Interlayer cation effects on the hydration state of smectite," *American Journal of Science*, vol. 297, no. 8, pp. 829–841, 1997.

[51] L. Calarge, B. Lanson, A. Meunier, and M. L. Formoso, "The smectitic minerals in a bentonite deposit from Melo (Uruguay)," *Clay Minerals*, vol. 38, no. 1, pp. 25–34, 2003.

[52] A. Meunier, B. Lanson, and B. Velde, "Composition variation of illite-vermiculite-smectite mixed-layer minerals in a bentonite bed from Charente (France)," *Clay Minerals*, vol. 39, no. 3, pp. 187–196, 2004.